Institut für Strömungsmechanik
und Elektronisches Rechnen im Bauwesen
der Leibniz Universität Hannover

Bericht Nr. 76/2008

Oliver Göthel

Numerical modelling of flow and wave induced scour around vertical circular piles

ISSN 0177-9028

Institut für Strömungsmechanik
und Elektronisches Rechnen im Bauwesen
Leibniz Universität Hannover
Appelstr. 9A
30167 Hannover

Tel.: +49-511-762-3568
Fax.: +49-511-762-3777
URL: http://www.hydromech.uni-hannover.de

Von der Fakultät für Bauingenieurwesen und Geodäsie der Leibniz Universität Hannover zur Erlangung des Grades eines Doktor-Ingenieurs (Dr.-Ing.) genehmigte Dissertation.

Referent:	Prof. Dr.-Ing. Werner Zielke
Korreferent:	Prof. B. Mutlu Sumer

Tag der Promotion: 28. April 2008

Zusammenfassung

Ein dreidimensionales, numerisches Strömungsmodell wurde mit einem Sedimenttransport und einem Modell zur Analyse der Bodenstabilität gekoppelt. Das Strömungsmodell ist in der Lage Berechnungen mit und ohne freier Oberfläche durchzuführen, wodurch stationäre Strömungen wie auch propagierende Wellen und die daraus resultierende Strömung im Nahbereich eines Bauwerks simuliert werden kann. Das Modell basiert auf den Reynold's gemittelten Navier-Stokes Gleichungen, wobei die Schließung des Gleichungssystems mit dem k-ω(SST) Modell durchgeführt wurde.

Die vom Strömungsmodell berechneten Schubspannungen am Boden werden an das Sedimenttransportmodell übergeben und mit diesen die Bodenevolutionsgleichung gelöst. Die Geometrie des sich verändernden Bodens wird nach einer festgelegten Dauer an das Strömungsmodell zurückgegeben, worauf eine Aktualisierung der Strömungsergebnisse durchgeführt wird. Da sich bei der Umströmung von Bauwerken lokal erhöhte Schubspannungen ergeben, führt dies zu einem intensiven Sedimenttransport und zur Bildung eines Kolkes. Die auftretenden steilen Bodengradienten werden in den Gleichungen zur Berechnung der Sedimentransportrate durch zusätzliche Ansätze berücksichtigt. Eventuell auftretende Sedimentrutschungen werden durch einen Algorithmus simuliert, der Sediment in Richtung des Gefälles umlagert, falls der Neigungswinkel des Bodens den Reibungswinkel übersteigt.

Das Sedimenttransportmodell wurde um ein Finite-Elemente Bodenmodell erweitert, das in der Lage ist, eine Stabilitätsanalyse des Bodens bei Einwirkung des Eigengewichts und äußerer Lasten durchzuführen. Dadurch können die Bereiche bestimmt werden, an denen Sediment- bzw. Hangrutschungen auftreten. Hierbei werden mehrere Bodenparameter in die Analyse sowie die Geometrie des Bodens mit einbezogen.

Das beschriebene Modell wurde auf verschiedene Laborversuche mit strömungs- und welleninduziertem Kolk angewendet. Neben einem Zylinder und einem senkrechten Wandeinbau in einer stationären Strömung, wurden auch Versuche mit kurzen Wellen (KC$<$6) sowie langen Wellen (KC$>$6) zur Validierung des Modells herangezogen. Weiterhin wurde ein aus einem Wellenspektrum entstandener Kolk im numerischen Modell nachgebildet.

Abstract

A three-dimensional flow model capable of simulation flows with or without free surface was coupled with a model capable of simulating sediment transport and bottom evolution, and a model for analysing soil stability. The flow model presented is capable of simulating a steady flow or a propagating wave in order to calculate the flow field in the proximity of a structure. The solver is based on the Reynold's averaged Navier-Stokes equations, whereas the closure of the set of equations is achieved by means of the k-ω(SST) turbulence model.

Using the shear stress at the bottom computed by the flow model, a sediment transport rate may be calculated and subsequently inserted in the bottom evolution equation. This leads to an intense sediment transport and thus to scour. Steep slopes will lead to sliding sediment grains when the actual slope angle exceeds the friction angle of the sediment. In order to keep the bottom geometry in a reasonable shape, an algorithm is used to simulate sliding sediments. Adjustments for the inception of motion and the sediment transport rate at slopes improve the original equations in such a way that sand sliding is less intensive with regard to the number of iterations rquired, even though it is still necessary. The resulting scour geometry is therefore also characterized by this algorithm, which depends on one soil parameter.

A more general model for determining slope stability was developed and coupled with the existing flow and sediment transport model. The bottom is idealised as a three-dimensional solid body and a finite element analysis is carried out in order to calculate the erosion zones under given conditions. When determining the slope stability, this approach not only takes account of the friction angle but also several other soil parameters as well as the bottom geometry.

The model described was used to simulate different laboratory experiments of flow and wave induced scour. A vertical cylinder and an abutment in steady flow conditions were considered as well as experiments with short waves (KC$<$6) and long waves (KC$>$6) to validate the model. Furthermore, a scour resulting from a wave spectrum was considered as test case for the numerical model.

Vorwort

Die vorliegende Arbeit ist in den Jahren 2002 – 2008 während meiner Tätigkeit am Institut für Strömungsmechanik und Elektronisches Rechnen im Bauwesen der Leibniz Universität Hannover entstanden. Während dieser Zeit bearbeitete ich das Forschungsprojekt “Numerische Modellierung von Strömung und Kolkung im Nahfeld von Wasserbauwerken“, das von der Deutschen Forschungsgemeinschaft (DFG) über insgesamt dreieinhalb Jahre gefördert wurde. Im Rahmen dieser Förderung wurde mir die Teilnahme an mehreren internationalen Konferenzen ermöglicht, auf denen ich gleichzeitig Bestätigung des eingeschlagenen Weges erfahren und neue Motivation für das weitere Arbeiten an diesem Projekt gewinnen konnte.

An dieser Stelle möchte ich Herrn Prof. Dr.-Ing. Werner Zielke für die Übernahme des Hauptreferats und die Unterstützung sowie den Freiraum während der Durchführung meiner Tätigkeiten am Institut danken.

Weiterhin danke ich Herrn Prof. B. Mutlu Sumer für die Übernahme des Korreferats. Prof. Sumer hat durch seine Forschung auf dem Gebiet der Kolkung an Wasserbauwerken wichtige Grundlagen und Erkenntnisse erarbeitet, die einen wesentlichen Einfluss auf den Inhalt des durchgeführten Projekts und die vorliegende Arbeit hatten.

Mein Dank gilt auch den Mitarbeitern und Kollegen mit denen ich während meiner Zeit am Institut zusammenarbeiten durfte. Das stets freundliche und produktive Arbeitsklima hat seinen Teil zur Durchführung des Projekts beigetragen. Hervorheben möchte ich an dieser Stelle die Zusammenarbeit mit Herrn Dr.-Ing. Holger Weilbeer, der mich als studentischen Mitarbeiter in das Arbeitsthema, das mich über viele Jahre begleitet hat, einführte und maßgeblich an der Antragstellung des Projekts beteiligt war.

Im Besonderen möchte ich mich auch bei Herrn Dr. Ian Westwood für die sprachliche Überarbeitung der in Englisch geschriebenen Arbeit bedanken.

Schließlich danke ich meiner Familie und insbesondere meiner Frau für die Unterstützung bei der Entstehung dieser Arbeit.

Hannover, Januar 2008
Oliver Göthel

Contents

1 Introduction

1.1 Motivation

All structures situated in a maritime- or river-environment are exposed to the fluid flow that surrounds them. The resulting forces acting on the structure and the surrounding soil are a result of flow or wave action, or the combination of both. Additional effects may include e.g. wave diffraction and reflection, wave breaking or flow contraction. These effects may result in an increased flow velocity in the vicinity of the structure and hence to higher shear stresses acting on the soil. Assuming that the soil in most cases consists of sediments that are vulnerable to erosion, an increase in the flow will result in increased sediment transport and subsequent scour. As indicated by many examples in the past, this may pose a serious threat to the stability of a structure.

In order to gain more knowledge concerning the scour process and the issue of soil stability under the influence of flow, a combined numerical model of flow, sediment transport and soil stability analysis has been developed. Whereas the flow and soil model are three-dimensional, sediment transport and bed evolution is simulated by means of two-dimensional model. The flow model is based on the Reynold's averaged Navier-Stokes equations with a scheme for calculating the free surface. By this means it is possible to analyse a flow and a wave-induced scour. Averaging the Navier-Stokes equations leads to the turbulence closure problem, i.e. the need for additional equations in order to close the set of available equations. This is achieved by using a modified version of the k-ω turbulence model which offers the advantage of simulating boundary-layer flows with a stagnation point and adverse pressure gradients.

Taking the bottom shear stress computed by the flow model as input for the sediment transport model, a time variable bottom topography may be calculated by means of the bottom evolution equation. The required transport rates are obtained from (semi-)empirical equations based on laboratory experiments. The considered material is sand and the main transport mode is bed-load. The transport of suspended sediment is neglected in the presented numerical investigations. Locally increased shear stress in the proximity of a structure leads to higher transport rates and thus to more intense erosion. As a consequence, a scour with steadily increasing slopes will develop. Once a slope has been established, the sediment transport is not only driven by shear stress but also by the force of gravity, which becomes more dominant with an increasing slope angle. Furthermore, a collapsing slope with sliding sediment will occur when the slope angle attains the sediment friction angle. As these sediment movements are only driven by the force of gravity, they are not taken into account in the above-mentioned transport rate equations but are treated separately using an algorithm which ensures that the slope angle cannot exceed the friction angle. The sediment is otherwise shifted in the direction of the slope until a stable condition is reached.

The slope stability is determined by comparing the actual slope angle with the friction angle of the used material concerned. This is a valid assumption for homogeneous, sandy materials which are preferred in laboratory experiments. The properties and distribution of natural soil, however, are far more variable than can be expressed by a single material parameter. For this reason a more general model for determining slope stability was developed and coupled with the existing flow and sediment transport model. The bottom is idealised as a three-dimensional solid body and a finite element analysis is carried out in order to calculate the erosion zones under given conditions. When determining the slope stability, this approach not only takes account of the friction angle but also several other soil parameters as well as the bottom geometry.

The model described was used to simulate different small and large scale cases investigated in laboratory experiments. This covers experiments with a steady flow as well as cases with waves. Most of the presented material is based on small scale cases, as large scale scour experiments are rarely available.

1.2 Literature review

1.2.1 Flow model

The vertical circular cylinder is one of the most widely used geometries for structures in the marine environment whereas river-based buildings are often designed with an oval cross-section. Nevertheless the circular cylinder remains the commonly considered cross-section in theoretical and experimental studies. Flow around structures is purely three-dimensional even in the case of a vertical cylinder where the geometry is constant over the depth. The flow field exhibits different effects depending on the type of flow approaching the structure. The effects that may occur such as, e.g. a stagnation point, flow contraction and vortex shedding are not only characteristic for a vertical pile but also for almost all other possible objects.

Different approaches for modelling the flow around a circular cylinder may be found in the literature. Reynold's averaged Navier-Stokes equations (RANS) with an adequate closure model and large eddy simulations are the most commonly used. In the case of RANS, turbulence modelling may be performed using a two equation model such as the k-ε or the k-ω model. Whereas Olsen and Melaaen (1993) and Olsen and Kjellesvig (1998) applied the first method in order to calculate the flow for a scour simulation, the latter method was applied in a modified form (Menter, 1992) by Weilbeer (2001) and Roulund et al. (2005) for the same purpose.

Although a large eddy simulation is certainly more accurate for calculating flow than a RANS model, a considerably longer computation time is required. This makes the method unsuitable for calculations involving longer periods than are necessary for simulating the scour process or for calculations involving high Reynold's numbers. A subgrid scale model is necessary in order to model the turbulence that is not resolved by the mesh. Several of these included in the literature were studied by Breuer (2000) and Salvatici and Salvetti (2003). These and among others Fröhlich and Rodi (2004) and Fröhlich et al. (2003), analysed the influence of spatial discretization on the results. The advantages of using a large eddy simulation were demonstrated by Catalano et al. (2003). By comparing the results of the latter with the results obtained from a calculation using a k-ε model it was shown that the large eddy simulation clearly yields better results regarding the pressure distribution and the separation points.

Yen et al. (2001) made use of the advantages of a large eddy simulation for calculating a scour. The flow was only modelled once with a horizontal bed and the velocities were then adapted to the changing bottom geometry without performing an LES flow simulation for updating the flow. The Reynold's number based on the pile diameter was only 3900.

Although RANS have several disadvantages compared with large eddy simulations, they were in fact succesfully used by Salaheldin et al. (2004) with a k-ϵ model. The resulting velocity profiles were found to be in good agreement with the measured data while the shear stresses showed small deviations. Nagata et al. (2002) used a nonlinear k-ϵ model in order to calculate flow and scour around a cylinder. This and the results of Weilbeer and Roulund et al. shows that RANS may succesfully be applied to solve three-dimensional flow and scour problems, which would otherwise be too time consuming using large eddy simulations.

1.2.2 Sediment transport

In a numerical model the sediment transport is usually subdivided into near-bottom transport and the transport of material in suspension. They are included in the general bottom evolution equation. Neglecting suspended sediment transport on the grounds that sandy material (the only material considered in the present work) is predominantly transported at the bottom, the problem reduces to finding an adequate description of the bed-load. This may be achieved using one of the numerous equations available for this purpose. The problem may be further simplified by assuming a uniform sediment, i.e. representation of the sediment particle diameters by a single mean diameter. This is a valid assumption as the experiments presented here were carried out in laboratories under well defined conditions with a given uniform sediment.

One of the first empirical expressions for the bed-load transport was obtained by Meyer-Peter and Müller (1948) from flume experiments with uniform grains as well as with mixed grain sizes. The resulting formula is still used very frequently.

Around the same time Kalinske (1947) and Einstein (1950) developed stochastic approaches which take the nature of a turbulent flow into account when calculating the transport rate. Both equations still require experimental data for calibrating the various parameters (van Rijn, 1993). The formulas of Meyer-Peter and Müller and Einstein were used by Frijlink (1952) to develope an equation that is a fit of the latter formulae and thus yields similar results. Other equations that should be mentioned are the equations of Bagnold (1966), Engelund and Fredsøe (1976) and van Rijn (1984). The latter were implemented in the present work and are presented in detail in Chapter 2.2.4. Several other more transport rate equations suitable for simulating sediment transport are also available, e.g Engelund and Hansen (1967), Zanke (1982a) and Cheng (2002).

Bed slopes are found to dramatically increase when scour occurs. As shown by the measurements of Smart (1984), this has a significant influence on the direction and magnitude of sediment transport. This effect may be taken into account by modifying the transport rate originally calculated for a horizontal bed. The transport rate in the longitudinal direction, i.e. the transport in the direction of the shear stress, is first adapted and then an additional transport rate is calculated in the transvere direction if a slope in this direction exists.

Changes in sediment transport rates along slopes were studied by Bagnold (1966), who developed an expression for adapting the transport rate on a horizontal bed for sloping bed conditions. Hardisty and Whitehouse (1988) found that the resulting transport rate underestimates the actual transport rate obtained from measurements. A similar approach was presented by van Rijn (1993), who compared the equation of Smart (1984) with the original formula of Meyer-Peter and Müller and found an expression for a slope factor applicable to a downward slope. Although the equation of Bagnold was developed for both an upward and downward slope, Damgaard et al. (1997) found that upward slope transport is adequately described by taking into account the changing threshold value in upward direction. Other approaches which take account of changing sediment transport rates are given by Koch and Flokstra (1981) and Kovacs and Parker (1994).

In the case that sediment transport occurs in the direction of the shear stress, a slope in the transverse direction causes additional gravity-induced transport in the direction of the transverse slope. This means that the resulting transport vector is no longer in the direction of the shear stress but slightly inclined in the direction of the slope. This behaviour was studied by Engelund (1974), Ikeda (1982, 1988) and Talmon et al. (1995). Ikeda developed a formula for calculating the sediment transport rate as a function of the longitudinal transport rate and the transverse slope. Talmon and Wiesemann (2006) found that the transverse transport rate is dependent on the grain size and presented a formula taking this into account.

Sediment particles resting on a slope are subjected to the acting shear stress as well as the force of gravity. The component of the gravity vector in the direction of the slope causes an increase in the critical Shields parameter when the shear stress acts in the upward direction and a decrease in the opposite case. A coefficient for the Shields parameter which takes account of the latter was first presented by Schoklitsch (1914). Similar expressions have also been derived by Whitehouse and Hardisty (1988), Lau and Engel (1999), Luque and Beek (1976), Hasbo (1995) and Chiew and Parker (1994).

1.2.3 Slope stability

The slopes that occur when a scour developes are subjected to shear stress, flow-induced pressure and gravity. Sediment grains begin to slide when the slopes become too steep, thus resulting in a loss of stability. In the presented numerical model this is taken into account by shifting sediment from higher to lower points in the computational mesh. The threshold of sediment sliding is identified by comparing the actual slope angle with the friction angle of the material. The only soil parameter used in this context is hence the friction angle, whereas slope stability is governed by additional parameters including the overall slope geometry.

Slope stability may be determined in a number of ways which are more or less accurate depending on the method used. Duncan (1996) has summarized the established methods, which include the ordinary method of slices (Fellenius, 1936), the modified method of Bishop (1955), Spencer's method (1967) and several other methods based on the assumption that it is appropriate to divide the soil mass into slices. Because these methods require an approach for estimating the side forces acting on each slice, the entire solution process combined with all other simplifying assumptions leads to uncertain results. The methods mentioned are nevertheless widely used in geotechnical engineering partly because of their ease of application and also due to the fact that the method of Bishop, for example, became a 'standard' for slope stability analysis (Griffiths and Marquez, 2007). Examples demonstrating the implementation of these methods may be found in Verruijt (1995).

In order to determine slope stability more accurately under scour conditions a finite element model for the soil was implemented in the present investigations. In contrast to the majority of numerical simulations carried out in geotechnical engineering, the analysis in the present case is three-dimensional rather than two-dimensional. The advantages of using a numerical model rather than one of the different methods of slices are e.g that the progression of failure can be monitored up to the point of total failure and that no assumptions are necessary concerning the shape or location of the failure surface. The point of total failure, as given by the results of the calculation, occurs when the soils shear strength is no longer able to sustain the acting force of gravity (Griffiths and Lane, 1999). An additional advantage of a three-dimensional model is the ability to more precisely define the slope geometry. This is especially important in the case of a scour hole whose slope is normally characterized by a round shape. In contrast to a two-dimensional model, a three-dimensional approach permits the modelling of a true three-dimensional shape rather than a two-dimensional geometry extended to the third dimension.

The force of gravity acting on a slope causes stresses in the soil which in turn lead to strains. Smaller strains are usually reversible and can therefore be described by the theory of linear elasticity (Verruijt, 1995; Davis and Selvadurai, 1996; Zienkiewicz and Taylor, 2000). When a slope is close to failure, however, plastic deformations occur in the soil as a result of irreversible strains. The adoption of an elastoplastic or viscoplastic approach for describing the stress-strain relationship offers a means of modelling soil behaviour more precisely (Zienkiewicz and Taylor, 2000; Davis and Selvadurai, 2002; Griffiths and Marquez, 2007). This is important in the presented cases where high stress levels occur and the slope is not only close to failure but also partially collapses (thereby leading to sliding sediment grains). Early examples of the application of these techniques are given by Smith and Hobbs (1974) and Zienkiewicz et al. (1975). In these examples the results were compared with the data of Taylor (1937) and with solutions obtained from the slip circle theory.

A distinction between linear and nonlinear deformations is possible using the Mohr-Coulomb criterion, which is suitable for soils possessing frictional and cohesive components (Smith and Griffiths, 1998). If the stress at a point in the computational mesh due to the acting force of gravity lies within the range of the failure criterion then it is assumed that only linear deformations occur. If the stress lies outside of the failure criterion, on the other hand, the deformation is irreversible and yield has occurred. The stress in the yielding region is then redistributed among the neighbouring elements in the mesh by a viscoplastic algorithm described by Perzyna (1966); Zienkiewicz and Cormeau (1974). Owing to the fact that the redistribution of stresses can cause yield in regions which were originally elastic, the stress redistribution process is carried out iteratively. The process ends when a stable condition is reached and no more plastic deformations occur.

The described algorithm was first implemented in a finite element model published by Smith and Griffiths (1988). The use of a finite element model for calculating slope stability is reported among others by Matsui and San (1992); Jeremic (2000); Sainak (2004); Griffiths and Marquez (2007).

1.2.4 Scour experiments

The process of scouring around structures is a widely studied effect. Many laboratory experiments have been carried out in the past to investigate scour phenomena. Physical modelling has mainly been carried out in flumes with either a steady current, waves or in rare cases a combination of both. Previous investigations have especially focused on scour around a pile in a steady current, as this type of scour has led to several severe failures of river bridge piers in the past. This phenomenon has been studied among others by Hjorth (1975); Melville (1975); Breusers et al. (1977); Ettema (1980); Zanke (1982b); Raudkivi and Ettema (1983); Chiew and Melville (1987); Melville and Sutherland (1988); Melville and Chiew (1999); Oliveto and Hager (2002); Link and Zanke (2004); Roulund et al. (2005).

A central question in most studies concerns the equilibrium scour depth, which is an important factor governing structural stability. Other topics of investigation include timescale, the shape of the scour hole or the influence of sediment composition. Early examples of the three-dimensional numerical modelling of current-induced scour are given by Olsen and Melaaen (1993) and Olsen and Kjellesvig (1998). Whereas the results in the former case were calculated using a steady-state solution of the flow, the latter case involved the modelling of unsteady flow with additional consideration of varying sediment transport rates along slopes. Measurements of current-induced scour together with the results of a numerical simulation have been presented by Roulund (2000). Besides introducing the concept of sliding sediment grains in numerical models, Roulund also took account of the changes in the critical shear stress along slopes. Weilbeer (2001) considered the same effects as Roulund and compared his results with Roulund's measurements. A later study based on the same measurements was published by Roulund et al. in 2005.

With the growth of offshore technology, questions arise concerning scour caused by tides and waves. Investigations are normally carried out with regular or irregular waves based on a particular wave spectrum (e.g. the Jonswap or the Pierson-Moskowitz spectrum). The wave-induced scour around a slender pile was investigated by Sumer et al. (1992, 1993, 2007). In this flow regime a horseshoe vortex and vortex shedding is present which leads to intense sediment transport in the proximity of the structure. It was shown by Sumer et al. (1992) and Kobayashi and Oda (1994) that the flow regime around a cylinder may be described by the Keulegan-Carpenter (KC) number. Slender piles lead to larger KC numbers ($KC > 6$) indicating the formation of a horseshoe vortex.

In contrast to the case of a slender pile, the flow regime around a large pile lacks a horseshoe vortex, vortex shedding and flow separation. Instead, diffraction of the wave occurs (Sumer and Fredsøe, 2002) and scour is caused by wave-induced velocities at the bed. This process was studied by Toue et al. (1992); Katsui and Toue (1993) and Sumer and Fredsøe (2001a). Zhao et al. (2002) and Zhao and Teng (2004) presented the results of a simulated scour in which the shear velocites were calculated by a wave model based on the Boussinesq equations and the mild-slope equations (Berkhoff, 1972), respectively. The influence of the slope on the sediment transport rate was not taken into account.

A wave with an underlying current leads to a scour hole similar to that produced by a steady current. This effect was studied by Eadie and Herbich (1986); Sumer and Fredsøe (2001b); Zhao et al. (2004); Rudolph and Bos (2006). If the flow is strong enough and the wave propagates in the same direction as the current, the horseshoe vortex is permanently present and becomes weaker and stronger in an alternating manner in accordance with the propagating waves. With increasing flow velocity the shape and depth of the scour hole converges to that of a scour hole produced by a current without wave action. The results of a two-dimensional numerical flow model with a combined wave model based on the mild-slope equations was presented by Zhao et al. (2004).

1.3 Outline of the present investigations

Following the foregoing literature review covering the various topics of this thesis, a brief outline of the present investigation is now given. The investigation focuses on the modelling of sediment transport and soil stability related processes. The input to the sediment transport model is calculated by a flow model described in Chapter 2.1. A brief explanation of the governing equations, pressure treatment, and free surface and turbulence modelling is presented. The boundary conditions for the case of a superimposed wave are given in Appendix A. First order Airy theory and the stream function theory for higher order waves are presented.

A description of near-bed sediment transport is given in Chapter 2.2. In this chapter the governing equations, transport rate equations, transport rate adjustments and the changing critical mobility parameter on slopes are presented. The inclusion and treatment of gravity-induced slidings of sediment grains in a numerical model are also explained.

The mathematical theory underlying the implemented soil model is described in Chapter 2.3. This chapter deals with the topic of linear and nonlinear deformations calculated by a three-dimensional numerical model. Boundary conditions and solution strategies are also taken into consideration.

Following a presentation of the different parts of the numerical model, Chapter

2.4 deals with the coupling and interaction of these models. The results of different numerical experiments to investigate flow and wave induced scour as well as scour hole stability analyses are subsequently presented in Chapter 3.

A conclusion of the presented results together with a closer examination of the perspectives of numerical models in scour and soil modelling are given in the closing chapter of this thesis.

2 Physical processes and model coupling

2.1 Flow model

The flow field in the proximity of structures is always complex. Because the flow field is predominantly three-dimensional, a three-dimensional model is necessary to correctly simulate flow behaviour. The governing equations of a three-dimensional (Reynold's averaged) Navier-Stokes equation solver are well known and may be found in numerous publications, e.g. Ziegler (1995); White (2003); Kundu and Cohen (2004). The following chapters present a summary of the equations used and the methods by which they are solved. Flow and sediment transport (see Chapter 2.2) model are based on the *Telemac* modelling system developed by the *Laboratoire National d'Hydraulique (LNHE)* of the *Electricité de France (EDF).*

The flow is solved on a three-dimensional mesh consisting of wedge elements. The advection in all simulations with flow only is computed using the method of characteristics or the streamline-upwind/Petrov-Galerkin (SU/PG) method. Both methods are of first order. While the method of characteristics is more stable and less time-consuming than the SU/PG, it is known to generate more numerical diffusion which has a smoothing effect on the solution. Other methods include the MURD (multidimensional upwind residual distribution) scheme, which is used in all nonlinear wave simulations, and the N and the PSI schemes. More detailed information on how these schemes handle advection may be found in Hervouet (2007). The non-hydrostatic algorithm used in the present study, which was originally developed by Jankowski (1999), is also presented in Hervouet (2007) together with information on the finite element method which is used to calculate the diffusion step. The handling of the free surface, as based on Hervouet and Pham (2007), is described in Chapter 2.1.4.

2.1.1 Governing equations

The mathematical description of flows is part of the theory of continuum mechanics. This consists of the equations for the conservation of mass and conservation of momentum (Eq. 2.1 and 2.2), i.e. the so-called Navier-Stokes equations. These describe the distribution of velocity and pressure in time and space, and are comprised of a system of nonlinear partial differential equations of second order. A basic assumption in the following equations is that the fluid is incompressible.

$$\nabla \vec{u} = 0 \tag{2.1}$$

$$\frac{\partial \vec{u}}{\partial t} + \vec{u} \cdot \nabla \vec{u} = -\frac{1}{\rho} \nabla p + \vec{\nu} \nabla^2 \vec{u} + \vec{f} \tag{2.2}$$

In order to solve the Navier-Stokes equations by numerical methods it is first necessary to simplify them. This is achieved by averaging the velocity and the pressure fields. The resulting equations are referred to as Reynold's averaged Navier-Stokes equations (RANS). Firstly, the velocity and the pressure are split into an averaged part and corresponding fluctuations:

$$\begin{aligned} u_i &= \overline{u_i} + u_i' \\ p &= \overline{p} + p' \end{aligned} \tag{2.3}$$

Inserting Eq. 2.3 into Eq. 2.2 leads to an expression (Eq. 2.4), in which the unknown variables are averaged and where the solution is an approximation of the Navier-Stokes equations.

$$\frac{\partial \overline{u_i}}{\partial t} + \frac{\overline{u_j u_i}}{\partial x_j} = \frac{\partial}{\partial x_j} \left[-\overline{p} \delta_{ij} + \mu \left(\frac{\partial \overline{u_i}}{\partial x_j} + \frac{\partial \overline{u_j}}{\partial x_i} \right) - \overline{u_i' u_j'} \right] + \overline{f_i} \tag{2.4}$$

The left-hand side of Eq. 2.4 represents the change of mean momentum due to the unsteadiness of the flow and the convection term. This is balanced by the stress resulting from the pressure field, the viscous stress term, the apparent stress $\left(-\overline{u_i' u_j'}\right)$ (also known as the Reynold's stress) and the acting body forces.

The Reynold's stress tensor may be approximated by means of the Boussinesq approach (Eq. 2.5). By inserting Eq. 2.5 in Eq. 2.4, an additional equation must be solved in order to obtain the turbulent viscosity ν_t. This is achieved with the aid of a suitable turbulence model (see Chapter 2.1.5).

$$\overline{u_i' u_j'} = -\nu_t \left(\frac{\overline{u}_i}{\partial x_j} + \frac{\overline{u}_j}{\partial x_i} - \frac{2}{3} \frac{\partial u_k}{\partial x_k} \delta_{ij} \right) + \frac{2}{3} k \delta_{ij} \tag{2.5}$$

2.1.2 Operator splitting

The method of operator splitting is used to split the Navier-Stokes equations into several parts based on the properties of the differential operators. Each part may then be treated in a single step by applying a suitable solution algorithm. All fractional steps together lead to the solution of the equation on the new time level. The splitting of an arbitrary variable is carried out according to the following equation:

$$\frac{\partial \vec{f}}{\partial t} = \frac{\vec{f}^{n+1} - \vec{f}^{d}}{\Delta t} + \frac{\vec{f}^{d} - \vec{f}^{a}}{\Delta t} + \frac{\vec{f}^{a} - \vec{f}^{n}}{\Delta t} \tag{2.6}$$

The first fractional step is the advection step, whereby the variable f^n is treated using one of the schemes mentioned in the introduction. This results in an interim solution f^a. The subsequent diffusion step, as computed by the finite element method, results in f^d. Applying the continuity equation, a preliminary solution for the variable f^{n+1} may be found. In the solution of the Navier-Stokes equations the variable f is a velocity u,v, or w or a tracer that is transported with the flow. Considering the velocity, Eq. 2.6 takes the form

$$\frac{\partial \vec{u}}{\partial t} = \frac{\vec{u}^{n+1} - \vec{u}^{d}}{\Delta t} + \frac{\vec{u}^{d} - \vec{u}^{a}}{\Delta t} + \frac{\vec{u}^{a} - \vec{u}^{n}}{\Delta t} \tag{2.7}$$

The hydrostatic pressure component is first taken into account. Splitting into fractional steps, the advection step is described by:

$$\frac{\vec{u}^a - \vec{u}^n}{\Delta t} + \vec{u} \cdot \nabla \vec{u} = 0 \tag{2.8}$$

Equation 2.8, which is hyperbolic in nature, may be solved by the method of characteristics or the Streamwise-Upwind/Petrov-Galerkin method (SU/PG). Although the latter is less diffusive, it is far more time-consuming in computational terms. Using the SU/PG method, advection and diffusion are solved in a single step. Otherwise the diffusion step is computed by means of Eq. 2.9.

$$\frac{\vec{u}^d - \vec{u}^a}{\Delta t} = \nabla \cdot (\vec{\nu} \nabla \vec{u}) + \vec{F}_u \tag{2.9}$$

The vector $\vec{F}_u$ includes source terms from free surface gradients and density gradients as well as miscellaneous sources. The solution of this equation may be obtained by the finite element method. The result obtained from the advection and diffusion step is an interim solution of the velocity field $\vec{u}$. In order to get the final velocity field the dynamic pressure must be calculated by means of the Poisson pressure equation (see Chapter 2.1.3).

2.1.3 Treatment of pressure

The frequently adopted assumption of a hydrostatic pressure distribution is no longer valid when dealing with waves or flow around structures. The acceleration of fluid particles in such cases results in a dynamic pressure component which must also be taken into account. This is achieved by splitting the overall pressure into a hydrostatic (p_H) and a dynamic (p_D) component (Jankowski, 1999; Hervouet, 2007):

$$p = p_H + p_D \tag{2.10}$$

The hydrostatic component p_H may be calculated by integrating over the water depth:

$$p_H = \int_z^S \rho g \, dz \tag{2.11}$$

By splitting the pressure into a hydrostatic and a dynamic component, the form of the momentum equation (Eq. 2.2) changes as follows:

$$\frac{\partial u}{\partial t} + \vec{u} \cdot \nabla u = -g\frac{\partial S}{\partial x} - g\frac{\partial}{\partial x}\left[\int\limits_z^S \frac{\Delta\rho}{\rho_0}dz\right] - \frac{1}{\rho_0}\frac{\partial p_D}{\partial x} + \nabla \cdot (\vec{\nu}\nabla u) \tag{2.12}$$

$$\frac{\partial v}{\partial t} + \vec{u} \cdot \nabla v = -g\frac{\partial S}{\partial y} - g\frac{\partial}{\partial y}\left[\int\limits_z^S \frac{\Delta\rho}{\rho_0}dz\right] - \frac{1}{\rho_0}\frac{\partial p_D}{\partial y} + \nabla \cdot (\vec{\nu}\nabla v) \tag{2.13}$$

$$\frac{\partial w}{\partial t} + \vec{u} \cdot \nabla w = -\frac{1}{\rho_0}\frac{\partial p_D}{\partial z} + \nabla \cdot (\vec{\nu}\nabla w) \tag{2.14}$$

Horizontal gradients of the free surface as well as pressure gradients appear in the above momentum equations (Eq. 2.12-2.14). In the vertical direction, only the hydrodynamic pressure gradient is retained. The hydrodynamic pressure component may be calculated by means of the Poisson pressure equation, which may be developed from the Navier-Stokes equations. The time derivative of velocities may be treated using the method of operator-splitting (see Chapter 2.1.2), which results in:

$$\frac{\partial u}{\partial t} = \frac{u^{n+1} - \tilde{u}}{\Delta t} + \frac{\tilde{u} - u^n}{\Delta t} \tag{2.15}$$

In Eq. 2.15 $\tilde{u}$ is an interim solution of the velocity field, which is not rquired to fulfil the condition of incompressibility. Eqs. (2.12-2.14) may be converted into two sets of equations, one of which includes the pressure gradients and the other of which is free of pressure terms:

$$\frac{\tilde{u} - u^n}{\Delta t} + \vec{u} \cdot \nabla u = -g\frac{\partial S}{\partial x} - g\frac{\partial}{\partial x}\left[\int\limits_z^S \frac{\Delta\rho}{\rho_0}dz\right] + \nabla \cdot (\vec{\nu}\nabla u) \tag{2.16}$$

$$\frac{\tilde{v} - v^n}{\Delta t} + \vec{u} \cdot \nabla v = -g\frac{\partial S}{\partial y} - g\frac{\partial}{\partial y}\left[\int\limits_z^S \frac{\Delta\rho}{\rho_0}dz\right] + \nabla \cdot (\vec{\nu}\nabla v) \tag{2.17}$$

$$\frac{\tilde{w} - w^n}{\Delta t} + \vec{u} \cdot \nabla w = -\frac{\rho}{\rho_0}g + \nabla \cdot (\vec{\nu}\nabla w) \tag{2.18}$$

$$\frac{\vec{u}^{n+1} - \tilde{\vec{u}}}{\Delta t} = -\frac{1}{\rho_0} \nabla p_D \tag{2.19}$$

Taking account of the fact that the resulting velocity field must fulfil the incompressibility condition ($\nabla \cdot \vec{u}^{n+1} = 0$), the following form of the Poisson pressure equation is obtained:

$$\nabla^2 p_D = \frac{\rho_0}{\Delta t} \nabla \cdot \tilde{\vec{u}} \tag{2.20}$$

The divergence-free velocity field for the next time step is obtained from Eq. 2.19 and the solution of Eq. 2.20.

2.1.4 Free Surface

The requirements placed on the quality of the free surface model increase noticeably when dealing with waves. Past simulations of streaming induced scour were carried out by calculating the free surface in an incremental step based on the solution of the two-dimensional (depth-averaged) continuity equation. The final velocity field was then computed in a second step after performing a velocity projection (see Jankowski (1999); Weilbeer (2001)). Simulations with nonlinear waves indicated the need for very small time steps. Using this type of scheme, it was also found that excessive wave damping occurred. This procedure was adapted and significantly improved by Hervouet and Pham (2007). All simulations dealing with waves in the present work implement a scheme for the free surface which solves the three-dimensional continuity equation and avoids the assumption of a hydrostatic pressure distribution. Instead, the dynamic pressure is calculated at the (former) hydrostatic step and is taken into account when solving the continuity equation. As a result, the waves show no damping when propagating through the computational domain.

The entire calculation is performed in a semi-implicit manner, whereby the velocity is calculated by Eq. 2.21, with θ as the implicitness factor (ranging from 0 to 1):

$$\overrightarrow{U} = \theta_u \overrightarrow{U}^{n+1} + (1-\theta)\overrightarrow{U}^n \tag{2.21}$$

Inserting Eq. 2.21 into the continuity equation and neglecting source terms leads to

$$\frac{h^{n+1}-h^{n}}{\Delta t}+\nabla h\left(\theta_{u}\overrightarrow{u}^{n+1}+(1-\theta)\overrightarrow{u}^{n}\right)=0 \tag{2.22}$$

While the above equation appears to be quite trivial, the problem of solving this equation is connected with the fractional step method. The final velocity field (and the final dynamic pressure, which is included in $\overrightarrow{u}^{n+1}$) is not known at this point in time. This means that an interim solution suitable for calculating the free surface is required. The variable $\overrightarrow{u}^{n+1}$ is calculated by averaging $\tilde{U}$ over the depth.

Assuming that an advection step based on the method of characteristics or an alternative explicit method has already been performed, the velocity U^{C} is known. Eq. 2.23 is derived from the momentum equation and provides a means of calculating the interim solution for the velocity $\tilde{U}$. In a hydrostatic solution $\tilde{U}$ would be equal to U^{n+1}. So far Eq. 2.23 has been used in this hydrostatic step. This includes the velocity after the advection step as well as the gradients of the free surface and the turbulent diffusion. The dynamic pressure is taken into account in a later fractional step. In order to overcome the modelling problems when simulating nonlinear waves, it is necessary to implement the full momentum equation, which includes the dynamic pressure (Eq. 2.24).

$$\frac{\overrightarrow{\tilde{U}}-\overrightarrow{U}^{C}}{\Delta t}=-s1u\;\overrightarrow{\tilde{U}}-g\;\overrightarrow{grad}(Z_{s})+div\;(\nu_{t}\;grad(\overrightarrow{U})) \tag{2.23}$$

$$\frac{\overrightarrow{\tilde{U}}-\overrightarrow{U}^{C}}{\Delta t}=-s1u\;\overrightarrow{\tilde{U}}-g\;\overrightarrow{grad}(Z_{s})-\frac{1}{\rho}\overrightarrow{grad}\,(p_{d})+div\;(\nu_{t}\;grad(\overrightarrow{U})) \tag{2.24}$$

The projection step for computing the velocity is carried out as the last fractional step and has a different meaning when treating the (fomer) hydrostatic step in the above-mentioned manner. The calculated pressure then only represents an increment which is added to obtain the final velocity. The vertical velocity, which has not been considered so far, must also to be taken into account in order to maintain consistency of the algorithm. The corresponding modification is given by Eq. 2.25.

$$\widetilde{W}^{n+1}=W^{D}-\frac{\Delta t}{\rho}\frac{\partial\,(p_{d})}{\partial z} \tag{2.25}$$

When considering the divergence of the momentum equation and splitting this into a hydrostatic step, which includes advection, diffusion, the effect of the hydrostatic pressure and the source terms, and a step for calculating the dynamic pressure, the resulting equation is Eq. 2.26. $\tilde{U}$ is again the interim solution for the velocity following the above-mentioned steps. A knowledge of the dynamic pressure at this fractional step leads to an improved solution of the continuity equation, especially when simulating a propagating nonlinear wave.

$$div\left(\frac{1}{\rho}\overrightarrow{grad}(p_d)\right)+\frac{1}{\Delta t}div\left(\overrightarrow{\widetilde{U}}-\overrightarrow{U}^n\right)=0 \tag{2.26}$$

2.1.5 Turbulence modelling

The k-ω model differs from the well-known and widely used k-ε model particularly in two particular aspects. Firstly, it is possible to integrate through the viscous boundary layer. This means that values for k and ω may be imposed directly at the boundary. Secondly, the model produces better results when dealing with adverse pressure gradients, as shown by Menter (1992) and Wilcox (1993). Weilbeer (2001), for example, testet different variants of the k-ω model for modelling flow around a cylinder. The standard version was first testet, followed by the so-called BSL and SSL variants. The latter variant is able to eliminate the high sensitivity of the model in the upstream region of the cylinder, as caused by the presence of a stagnation point.

The original k-ω model consists of two transport equations. The first of these is for the turbulent kinetic energy k:

$$\frac{\partial k}{\partial t}+\vec{u}\nabla k=\nabla\cdot\left(\nu+\frac{\nu_t}{\sigma_k}\right)\nabla k+P-\beta^* k\omega \tag{2.27}$$

and the second for the dissipation rate ω:

$$\frac{\partial \omega}{\partial t}+\vec{u}\nabla \omega=\nabla\cdot\left(\nu+\frac{\nu_t}{\sigma_\omega}\right)\nabla \omega+\alpha\frac{\omega}{k}P-\beta\omega^2 \tag{2.28}$$

The appropriate production term P may be written as:

$$P = \nu_t \left(\frac{\partial u_i}{\partial x_j} + \frac{\partial u_j}{\partial x_i} \right) \frac{\partial u_i}{\partial x_j} \tag{2.29}$$

It is finally possible to calculate the eddy viscosity, which may then be inserted into the RANS momentum equation:

$$\nu_t = \frac{k}{\omega} \tag{2.30}$$

Five empirical constants are required in the standard formulation of the k-ω model (Table 2.1).

α	β^*	β	σ_k	σ_ω
$\frac{5}{9}$	$\frac{9}{100}$	$\frac{3}{40}$	2	2

Table 2.1: Default values of the empirical k-ω constants

Menter (1992) developed two variants of the k-ω model in order to resolve the weaknesses of the standard version, namely the BSL (Baseline) and the SST (Shear Stress Transport) variants. The BSL model combines the positive behaviour of the k-ω model of Wilcox in the near wall region with the k-ε, which yields good results in the region outside of the boundary layer. The BSL variant of Menter was further enhanced by Wilcox, who developed the following transport equation for ω:

$$\frac{\partial \omega}{\partial t} + \vec{u} \nabla \omega = \nabla \cdot \left(\nu + \frac{\nu_t}{\sigma_\omega} \right) \nabla \omega + \alpha \frac{\omega}{k} P - \beta \omega^2 + \frac{\sigma_d}{\omega} \nabla k \nabla \omega \tag{2.31}$$

with

$$\sigma_d = \begin{cases} 0, & \nabla k \nabla \omega \leq 0 \\ \sigma, & \nabla k \nabla \omega \geq 0 \end{cases} \tag{2.32}$$

In addition to the assumptions made in the BSL model, the SST variant of the k-ω model takes into account the fact that for flows with a boundary layer the stress (Bradshaw et al., 1967) cannot exceed

$$\tau = 0.3\rho k \tag{2.33}$$

The turbulent viscosity is defined by

$$\nu_t = \frac{0.3k}{max(0.3\omega; \Omega F)} \tag{2.34}$$

in which the vorticity is calculated using Eq. 2.35.

$$|\Omega| = \left|\frac{\partial w}{\partial y} - \frac{\partial v}{\partial z}\right| + \left|\frac{\partial u}{\partial z} - \frac{\partial w}{\partial x}\right| + \left|\frac{\partial v}{\partial x} - \frac{\partial u}{\partial y}\right| \tag{2.35}$$

The blending function F (Eq. 2.36) is then applied in order to make use of the original formulation in regions outside of the boundary layer. In Eq. 2.36 z denotes the distance from the boundary.

$$F = tanh\left(\left[max\left(2\frac{\sqrt{k}}{0.09\omega z}; \frac{500\nu}{z^2\omega}\right)\right]^2\right) \tag{2.36}$$

2.1.6 Bottom shear stress

Experiments were carried out by Nikuradse (1933) on pipes with sand along the pipe walls. The grain size s varied from $s/R = 1/15$ to $s/R = 1/500$, whereby R denotes the pipe radius. The effective grain roughness coefficient that resulting from these experiments is referred to as k_s. This parameter describes the influence of roughness on the flow in the vicinity of a boundary. It is assumed that the total roughness k_s is the sum of the grain roughness $k_{s,g}$ and a form roughness $k_{s,f}$, due to bed forms such as ripples and dunes. In the scour experiments carried out in the present work the form roughness is neglected and therefore $k_{s,f} = 0$.

$$k_s = k_{s,g} + k_{s,f} \tag{2.37}$$

Based on the mean particle size, the grain roughness may be approximated as follows:

$$k_{s,g} = 3\ d_m \tag{2.38}$$

In the case of rough channels the viscous layer at the boundary is followed by a region with a logarithmic velocity distribution. The logarithmic law describing this distribution may be expressed as

$$\frac{u}{u_*} = \frac{1}{\kappa}\, ln \left(\frac{y_0}{k_s} \right) + B \tag{2.39}$$

Here, u/u_* is the ratio of the flow velocity to the shear velocity and κ is the von Karman constant, which is equal to 0.41. The distance from the boundary is denoted by y_0 and k_s is the boundary roughness mentioned above. The constant B is a function of the non-dimensional roughness parameter $k_s^+ = u_* k_s / \nu$. For a turbulent flow in a completely rough regime Nikuradse found that $B = 8.5$. This reduces Eq. 2.39 to

$$\frac{u}{u_*} = \frac{1}{\kappa}\, ln \left(\frac{30\, y_0}{k_s} \right) \tag{2.40}$$

In order to calculate the sediment transport rate, the shear stress at the bottom is also required. Using the shear velocity from Eq. 2.40 and inserting this into Eq. 2.41 leads to the shear stress that is used in the sediment transport model.

$$u_* = \sqrt{\frac{\tau_B}{\rho}} \tag{2.41}$$

2.2 Sediment transport and bottom evolution

When a fluid flows over a movable bed consisting of sediment particles, a shear force develops and acts on the single grains. The shear forces are caused by the coarseness of the bed, which gives rise to pressure fluctuations, and also due to the fact that fluids tend to adhere to solid walls (Zanke, 1982a). In the case that the shear forces are large enough to set the grains in motion, sediment transport takes place. Lighter sediments go into suspension and are carried away by the flow. Heavier sediments are transported as bed-load near the bottom surface in the direction of the shear stress. As will be demonstrated in Chapter 2.2.5, this behaviour is also influenced by the bottom slope. In the present model the suspended sediment transport is neglected, as only coarser material is used in the numerical experiments which tends to be transported as bed-load.

2.2.1 Material properties

Sediments in a natural environment consist of particles or grains which primarily result from the disintegration of rocks. Grain sizes range from large fragments to small, colloidal particles. The shape of grains is formed by the natural environment, which leads to rounded as well as angular grains. The density of grains varies according to the composition of the constituent materials. The predominant materials present in sediment grains are quartz and clay. While quartz is non-cohesive, clay is generally cohesive due to the fact that it consists of flat plates with a diameter of less than about 0.06mm. This means that clay tends to flocculate. The size of sandy particles, as used in the present experiments, lies in the range of 0.06mm to 2mm. The density of the above-mentioned materials is approximately $\rho_s = 2650$ kg/m^3. The specific gravity is given by the ratio of the fluid density to the sediment density: $s = \rho_s/\rho$. An additional property relevant to the present study is the angle of repose, which is a limiting parameter with regard to slope angles.

The sediment properties considered here are:

- density
- shape

- size
- angle of repose

Neglecting suspended sediment transport in the present investigation (see Chapter 2.2.2), a knowledge of the fall velocity is not required. This also applies to the porosity, which is only required when considering the packing of sediments and consolidation history. A single dimensionless parameter D_* (Eq. 2.43) is used here to describe sediment particles and their properties. This parameter reflects the influence of the gravity g, the particle density ρ and the fluid viscosity ν. Sediments in a natural environment consist of a range of particle sizes. Here d_{50} is used, which is the median particle diameter of the bed material, i.e. the particle size below which 50% by weight is finer. Another characterisation often used is the mean particle size, which is defined as

$$d_m = \Sigma\ (p_i\ d_i)/100 \tag{2.42}$$

whereby p_i is the percentage by weight of each grain.

$$D_* = \left(\frac{(\rho_S - \rho)}{\rho} \frac{g}{\nu^2} \right)^{\frac{1}{3}} d_{50} \tag{2.43}$$

2.2.2 Bottom evolution

The result of a flow simulation provides a knowledge of the magnitude and the direction of the shear stress acting on the sediment particles ($\vec{\tau}_B$). This information may be used to determine the transport capacity (see Chapter 2.2.4) and the direction of the sediment flux $\vec{q}_s$. The sediment flux and the shear stress are related by Eq. 2.44. This vector does not include the force of gravity acting on the sediment particles. The influence of slopes and therefore gravity will be discussed in Chapter 2.2.5.1. The sediment flux alone offers no information on how the bed will change in height. Inserting the result of Eq. 2.44 in the bottom evolution equation (Eq. 2.45) leads to the change of bed height with time, i.e. the bottom evolution.

$$\vec{q_s} = q_s \frac{\vec{\tau}_B}{\|\vec{\tau}_B\|} \tag{2.44}$$

$$\frac{\partial z_B}{\partial t} = -\ \mathrm{div}\ \vec{q_s} = -\left(\frac{\partial q_{sx}}{\partial x} + \frac{\partial q_{sy}}{\partial y}\right) \tag{2.45}$$

2.2.3 Inception of sediment motion

Sediment transport takes place when the acting shear stress exceeds a critical value. A large number of experimental studies dealing with this topic have been carried out by various investigators, e.g. Shields (1936); Graf (1971); Raudkivi (1976); Yalin and da Silva (2001). In most studies the critical value for incipient motion of sediment is related to the critical bed shear stress $\tau_{b,cr}$. In a non-dimensional expression this is referred to as the critical Shields parameter θ_{cr} (Eq. 2.47), as shown in Fig. 2.1. Although this is still the most widely adopted criterion for defining the inception of sediment motion, a number of inconsistencies and misconceptions (Buffington, 1999) and discrepancies exist in the experiments (Shvidchenko and Pender, 2000).

The critical Shields parameter may be calculated by parametrizing the Shields curve (Eq. 2.46), as carried out by van Rijn (1993). the shear stress and mobility parameters are related by Eq. 2.47. While Shields relates the critical shear stress to a Reynold's number which includes the actual shear stress acting on the particles, van Rijn uses the dimensionless particle diameter D_*, which includes the material density in order to calculate the critical value. Both methods lead to similar results.

$$\begin{aligned}
\theta_{cr} &= 0.24\, D_*^{-1} && for && 1 < D_* \leq 4 \\
\theta_{cr} &= 0.14\, D_*^{-0.64} && for && 4 < D_* \leq 10 \\
\theta_{cr} &= 0.04\, D_*^{-0.1} && for && 10 < D_* \leq 20 \\
\theta_{cr} &= 0.013\, D_*^{0.29} && for && 20 < D_* \leq 150 \\
\theta_{cr} &= 0.055 && for && D_* > 150
\end{aligned} \tag{2.46}$$

$$\theta = \frac{\tau_b}{(\rho_S - \rho) g d} \geq \theta_{cr} \tag{2.47}$$

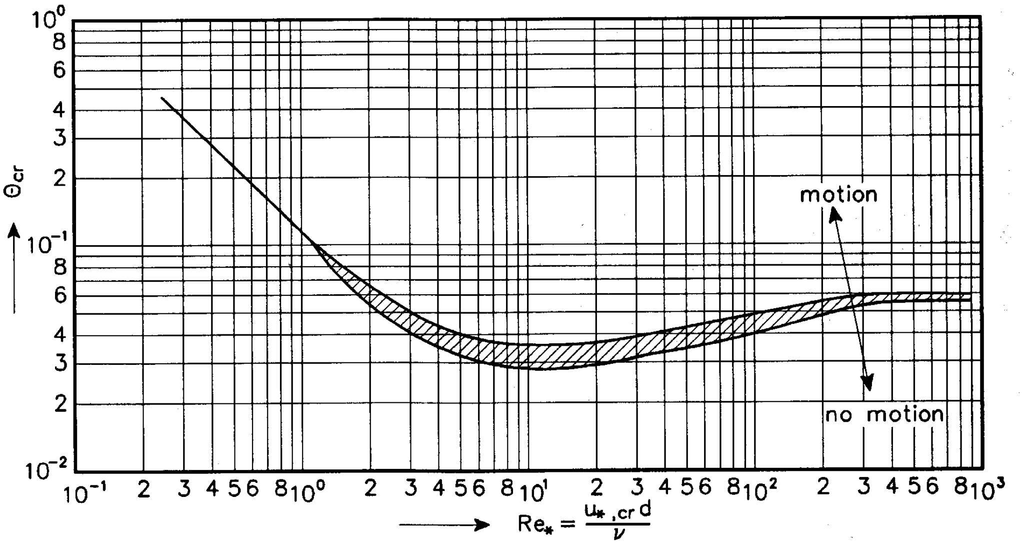

Figure 2.1: Inception of sediment motion (Shields, 1936)

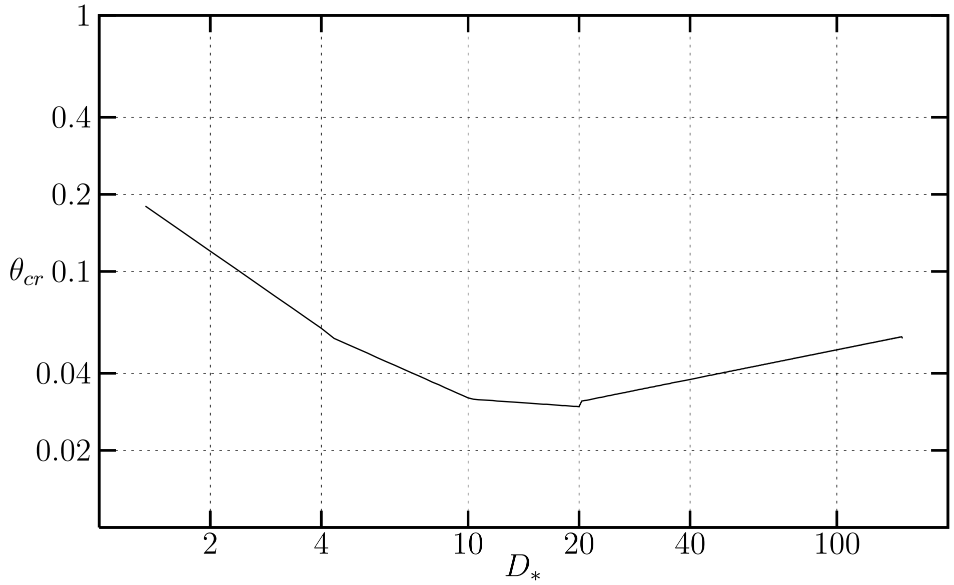

Figure 2.2: Parametrization of the Shields curve

2.2.4 Transport rate

2.2.4.1 Van Rijn

Eq. 2.49 developed by van Rijn (1984) is based on laboratory experiments. The grain diameters considered in the experiments were in the range of $200\mu m < d_{50} < 2000\mu m$. The water depth was greater than 0.1m in all experiments and the Froude number was less than 0.9.

Van Rijn assumes in his approach that particle movement is dominated by jumps and saltation. The bed height may then be approximated by the following equation:

$$\frac{\delta_b}{d} = 0.3\, D_*^{0.7}\, T^{0.5} \quad \text{with} \quad T = \frac{\tau_b - \tau_{b,cr}}{\tau_{b,cr}} \tag{2.48}$$

$$q_s = \alpha \sqrt{\frac{\rho_s - \rho}{\rho} g d_{50}^3}\, D_*^{-0.3} T^{\beta} \tag{2.49}$$

An equation for the particle velocity was also developed from experiments and has the following form:

$$\frac{u_b}{\left[(s-1)\, g\, d\right]^{0.5}} = 1.5\, T^{0.6} \quad \text{with} \quad s = \frac{\rho_S}{\rho} \tag{2.50}$$

Using the equation for the sediment concentration

$$\frac{c_b}{c_o} = 0.18\, \frac{T}{D_*} \tag{2.51}$$

and inserting it into $q_s = \delta_b u_b c_b$ results in Eq. 2.49, which may be used to determine the transport capacity under the given conditions.For a value of $T > 3$ the equation was found to overestimate the transport capacity and was hence modified in order to fit the results of the laboratory experiments:

$$\begin{aligned} q_s &= 0.053\, (s-1)^{0.5}\, g^{0.5}\, d_{50}^{1.5}\, D_*^{-0.3}\, T^{2.1} \\ q_s &= 0.1\, (s-1)^{0.5}\, g^{0.5}\, d_{50}^{1.5}\, D_*^{-0.3}\, T^{1.5} \quad \text{for} \quad T \geq 3 \end{aligned} \tag{2.52}$$

2.2.4.2 Meyer-Peter and Müller

An alternative approach for calculating the bed-load transport capacity is by means of Eq. 2.53, as developed by Meyer-Peter and Müller (1948, 1949). Numerous experiments were carried out in a flume with a length of 50m and a cross-section of $2 \times 2m^2$. The water depth was 0.1 to 1.2m. The resulting equation is only valid for particle sizes greater than 0.4mm and less than 29mm, which approximately corresponds to the diameter range of coarse sand. This equation is therefore more applicable in a river than in a coastal environment. In the present work the equation was used e.g. for calculating the transport capacity in a simulated laboratory experiment with an artificial sediment (see Chapter 3.1.1).

$$\begin{aligned} q_s &= 8\sqrt{\frac{\rho_s-\rho}{\rho} g d_m^3 (\mu\theta - \theta_{cr})^3} \\ q_s &= 8\frac{1}{\rho^{1/2}(\rho_s-\rho)g}(\mu\tau_b - \tau_{cr}) \end{aligned} \tag{2.53}$$

In Eq. 2.53, θ is again the mobility parameter (Eq. 2.47) and μ is the bed-form factor, which may be calculated using the overall Chézy coefficient (Eq. 2.55) and the grain-related Chézy coefficient (Eq. 2.56).

$$\mu = \frac{C}{C'} \tag{2.54}$$

$$C = 18\; ln(12h/k_s) \tag{2.55}$$

$$C' = 18\; ln(12h/d_{90}) \quad \text{with} \quad d_{90} = 3d_m \tag{2.56}$$

Meyer-Peter and Müller used the mean diameter d_m in their work. This is about 1.1 to 1.3 times greater than the d_{50} parameter for almost uniform material. By way of an example Van Rijn (1993) demonstrated that the influence of the particle diameter on the resulting sediment transport capacity is only very small and therefore the median particle diameter d_{50} may also be used.

2.2.4.3 Engelund and Fredsøe

The transport rate equation developed by Engelund and Fredsøe (1976) describes the transport rate as a product of the particle volume, the particle velocity u_b and the probability of occurrence of moving particles per particle area. This equation reads as follows:

$$q_s = \frac{\pi}{6} d^3 \frac{p}{d^2} u_b \tag{2.57}$$

The required particle velocity may be calculated using a semi-empirical equation (Eq. 2.58), where u_* is the shear velocity and α is a parameter in the range of 6 to 10. In the experiments presented at a later stage a value of $\alpha = 10$ is used.

$$\vec{u}_b = \alpha\, \vec{u}_* \left(1 - 0.7\sqrt{\frac{\theta_{cr}}{\theta}}\right) \tag{2.58}$$

The probability of occurrence of moving particles is calculated using Eq. 2.59, where μ_d is the dynamic friction coefficient. For the materials considered in the present study a value $\mu_d = 0.51$ was adopted.

$$p = \left[1 + \left(\frac{\frac{\pi}{6}\,\mu_d}{\theta - \theta_{cr}}\right)^4\right]^{-\dfrac{1}{4}} \tag{2.59}$$

2.2.4.4 Cheng

Most transport rate equations are of an empirical nature and were developed with the aid of laboratory measurements. As these measuerements were made under different conditions, e.g. for low, moderate or high shear stress, the derived equations are only valid for the particular conditions corresponding to each set of measurements. The sediment transport formula of Cheng (2002) was derived to fit measurements and transport formulae for low, moderate and high shear stress conditions. The concept of critical shear stress was not taken into account owing to its limitations when dealing with low shear stress and hence weak sediment transport. Experiments such as those of Paintal (1971) show that there is no shear stress below which absolutely no grains move. Although the transport rate becomes very small for very low shear stress values, it never equals zero.

The non-dimensional transport rate equation of Cheng is derived from the relationship $\Phi \sim \theta^n$ and takes the form

$$\Phi = 13\,\theta^{1.5}\,\exp\left(-\frac{0.05}{\theta^{1.5}}\right) \tag{2.60}$$

whereby the transport rate q_s may be written as

$$q_s = \Phi\, d\sqrt{(s-1)gd} \tag{2.61}$$

Eq. 2.60 fits the measurements of Meyer-Peter and Müller (1948), Einstein (1950), Bagnold (1973) and Yalin (1977) well for moderate and high shear stress. A comparison of Eq. 2.60 with the formulae of Paintal (1971) and Einstein (1942) shows that it is also able to correctly reproduce transport rates under low shear stress conditions.

2.2.5 Influence of bottom slope

The bottom slope is the inclination of the bottom surface measured from a horizontal plane. The bottom slope influences both the direction and the amount of the transported sediment due to the gravity force components acting on the sediment particles. In the case of a developing scour simulated by a numerical model, the slope angle grows quickly and unhindered owing to the absence of a limiting parameter for erosion or the slope gradients in the bottom evolution or transport rate equations. Almost all transport rate equations were developed for a horizontal bed. In an environment with bottom slopes, however, these equations do not yield a meaningful solution. In addition to the flowing fluid, which gives rise to shear stress at the bottom surface, a slope-induced downhill force is present which must also be taken into account. This causes a change in the sediment transport rate and shifts the point of inception of the sediment motion.

An additional slope-induced effect is the sliding of sediment grains when the bottom angle attains the friction angle and a failure of bottom stability occurs. Approaches taken from the literature which are used in the numerical model will be discussed in the following chapters.

2.2.5.1 Transport rate

An increase in the transport rate on a downward slope is taken into account by applying different equations for a longitudinal and a transverse slope. Eq. 2.62 as developed by van Rijn (1993) based on the equation of Smart (1984), predicts the amplification factor k_L for the transport rate on a downward slope. In Eq. 2.62 C is the Chézy coefficient and β_L is the slope angle in the longitudinal direction.

Although it seems reasonable to assume that the transport rate in the uphill direction should be decreased, Damgaard et al. (1997) found that no modification is necessary in this case. It is only necessary to take into account the modification of the Shields parameter (see Chapter 2.2.5.2) for an increasing elevation when calculating the bed-load.

$$k_L = \frac{1}{2} g^{-0.5} \left(\frac{d_{90}}{d_{30}} \right)^{0.2} C \tan^{0.6} \beta_L \left(\frac{\tau_b}{(\tau_b - \tau_{b,cr})} \right)^{0.5} \tag{2.62}$$

The bed-load transport in the transverse direction was studied by Engelund (1974), Ikeda (1988) and Sekine and Parker (1992). The approach of Ikeda was chosen in the present study and implemented in the sediment transport model. The transport rate in the transverse direction is described by:

$$q_{s,T} = 1.5 \left(\frac{\tau_{cr,T}}{\tau} \right)^{0.5} \tan \beta_T \;\; q_S \tag{2.63}$$

Fig. 2.3 shows the effects of Eq. 2.63. Because the slope is perpendicular to the acting shear velocity, the direction of sediment transport is influenced by the slope. The resulting sediment transport rate vector is then no longer in the direction of the shear velocity, but slightly inclined in the direction of the slope. The other extreme situation is when the shear velocity is in the same direction as the slope. Figure 2.4 shows how the sediment transport rate is increased by Eq. 2.62 in the latter case without any alteration in its direction.

2.2.5.2 Critical Shields parameter

Sediment particles lying on a downhill slope are affected by a downhill force which increases the particle mobility in the direction of the slope and vice versa in the

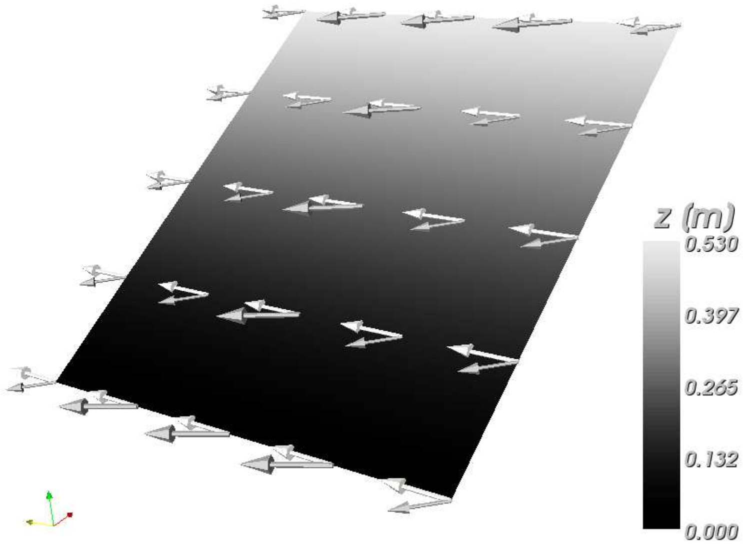

Figure 2.3: Influence of a transverse slope on q_s

uphill direction. Experimental data indicate that not only the transport rate (Smart, 1984) but also the threshold conditions change on a sloping bed. It is necessary to modify the critical mobility parameter θ_c in order to take account of this effect. The latter is decreased when the shear velocity points in the same direction of the slope and increased when it points upwards.

The Shields parameter for a horizontal bed is thus adjusted by Eq. 2.64 and Eq. 2.65 for longitudinal and transverse slopes based on the direction of the bed shear velocity. Eq. 2.64 which was first presented by Schoklitsch (1914), was derived from the equilibrium of forces acting on a single particle on a sloping bed. A comparison with experimental data was found to show good agreement (Whitehouse and Hardisty, 1988). An adjustment of the critical Shields parameter for transverse slopes (Eq. 2.65) was also derived by Lane (1955) and Ikeda (1982), and first presented by Leiner (1912). In Eq. 2.64 and Eq. 2.65, ϕ is the angle of repose and β is the actual slope angle. Fig. 2.5 shows a plot of both equations. Although these equations are only defined for small slope angles, the results for steeper slopes are still found to be reasonable. Both approaches converge to zero

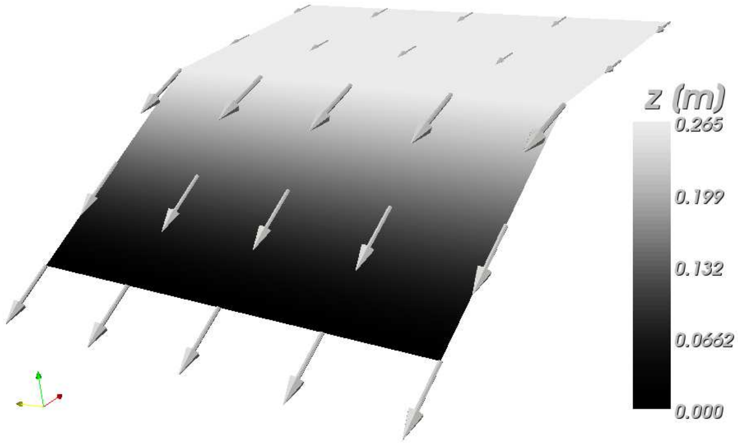

Figure 2.4: Influence of a longitudinal slope on q_s

when the slope angle converges to the friction angle. As a consequence, both values must to be limited in order to avoid meaningless results.

$$\alpha_L = \frac{sin(\phi - \beta_L)}{sin\phi} \tag{2.64}$$

$$\alpha_T = \cos\beta_T \left[1 - \tan^2\beta_T / \tan^2\phi\right]^{0.5} \tag{2.65}$$

Similar investigations carried out by Chiew and Parker (1994), Hasbo (1995), Whitehouse and Hardisty (1988), Lau and Engel (1999) and Luque and Beek (1976) resulted in similar expressions for the correction of critical Shields parameter. The approaches of Schoklitsch and Leiner were used in the present study owing to the reasonable results obtained.

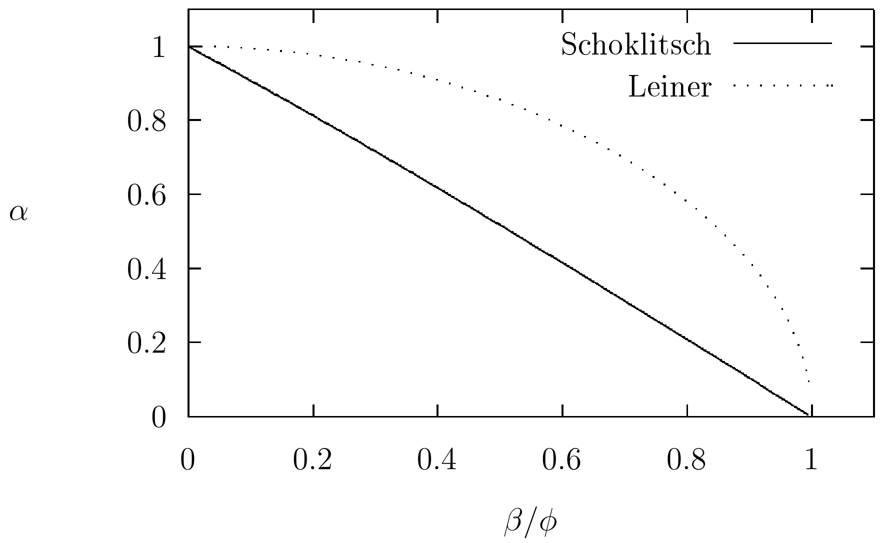

Figure 2.5: Correction factor of Schoklistch and Leiner

2.2.6 Sliding sediments

Developing scour gives rise to steep slopes along all sides of a scour hole. The slope angle increases and converges to the friction angle (Table 2.2). This eventually leads to failure of slope stability and to sliding sediments along the slope in the direction of the downward gradient. This process, which has been studied in laboratory experiments (Roulund et al., 2005), must to be taken into account in order to obtain reasonable results from the numerical model. The resulting bottom geometry is therefore limited by this stability criterion. The scour process is only defined for sandy material without any cohesive sediments. Fig. 2.6 shows a definition sketch of the sediment grains sliding down a slope whith a slope angle β greater than the friction angle.

This process may be modelled in a number of different ways. Roulund et al. (2005) developed an algorithm in which a sediment transport is initiated from the highest points in the direction of the downward gradient. The unstable condition of the bottom is transformed into a stable condition by an iterative procedure in which the final geometry is attained in incremental steps.

An alternative method for simulating sediment slide is the iterative shifting of

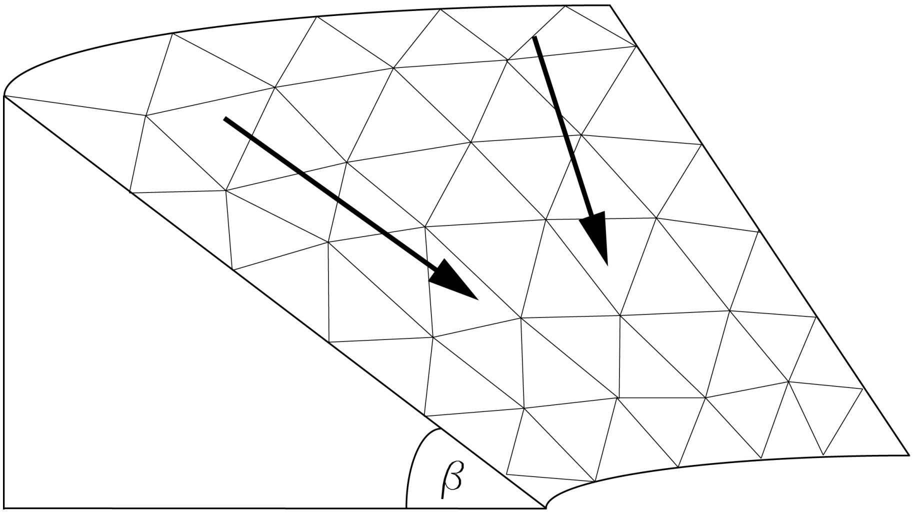

Figure 2.6: Slope with a slope angle β showing the sediment slide direction

sediment without the need to calculate a transport rate and solve the bottom evolution equation. Sediment shifting implies that the material at a higher mesh point is transferred to a nearby neighbouring point lower than the sediment source, and where the slope angle between those two points exceeds a certain limit. This limit is naturally the friction angle plus a small threshold value. The algorithm is terminated when the friction angle is attained. This guarantees that the resulting bottom geometry satisfies one soil parameter and that no points of discontinuity exist. As threshold value of two degrees proposed by Roulund et al. (2005) was also used in the present model.

d_{50} $[m]$	Friction angle (ϕ)	
	Rounded particles	Angular particles
≤ 0.001	30°	35°
0.005	32°	37°
0.01	35°	40°
0.05	37°	42°
≥ 0.1	40°	45°

Table 2.2: Range of the friction angle (van Rijn, 1993)

2.3 Soil model

When a slope develops, the slope gradient increases continuously until failure occurs. The sliding of sediment grains then takes place in order to re-establish a stable slope condition. Flow and fracture are the two main failure modes. A sandy soil tends to flow when the stress exceeds a critical value, whereas fracture is of more interest when considering rocks and concrete. The modelling procedure thus involves a calculation of the deformations, a determination of the point of failure and then an estimation of how the material responds under flow conditions.

The first part of this procedure is dealt with by an elastic model that approximates the material behaviour as beeing linear elastic (Chapter 2.3.2.1). Secondly, a failure criterion is introduced which is suitable for determining the transition point between linear elasticity and plastic deformations.

Although soil is a mixture of particles of different minerals in which the pore spaces are filled by either a fluid, gas or both, it is treated and idealised as a continuum. This implies that it may be subdivided into a number of elements whereby each element represents a part of the continuum. Although the particulate nature of soil is neglected in most engineering applications, several theories exist which take this into account (Davis and Selvadurai, 2002).

2.3.1 Stress and strain

Forces acting on a body cause a deformations which may be expressed with the aid of a displacement vector (Eq. 2.66). This vector points from the origin to the location where a point has moved due to the deformation process. By assigning a vector to every point of the body a vector field covering the complete volume is obtained. Taking spatial derivatives of the components of the displacment vector gives the displacement gradient matrix ∇u (Eq. 2.67). The components are denoted by ε for the extensional strains and γ for the shear strains, respectively.

The stresses and corresponding strains resulting from the acting forces are related by the constitutive equations. These equations, which are material-dependent, are described in Chapter 2.3.2.

$$\vec{u} = \begin{bmatrix} u \\ v \\ w \end{bmatrix} \tag{2.66}$$

$$\begin{array}{cccc} \begin{bmatrix} \epsilon_x \\ \epsilon_y \\ \epsilon_z \\ \gamma_{xy} \\ \gamma_{yz} \\ \gamma_{xz} \end{bmatrix} & = & \begin{bmatrix} \frac{\partial}{\partial x} & 0 & 0 \\ 0 & \frac{\partial}{\partial y} & 0 \\ 0 & 0 & \frac{\partial}{\partial z} \\ \frac{\partial}{\partial y} & \frac{\partial}{\partial x} & 0 \\ 0 & \frac{\partial}{\partial z} & \frac{\partial}{\partial y} \\ \frac{\partial}{\partial z} & 0 & \frac{\partial}{\partial x} \end{bmatrix} & \begin{bmatrix} u \\ v \\ w \end{bmatrix} \\ \boldsymbol{\varepsilon} & = & \mathbf{A} & \mathbf{u} \end{array} \tag{2.67}$$

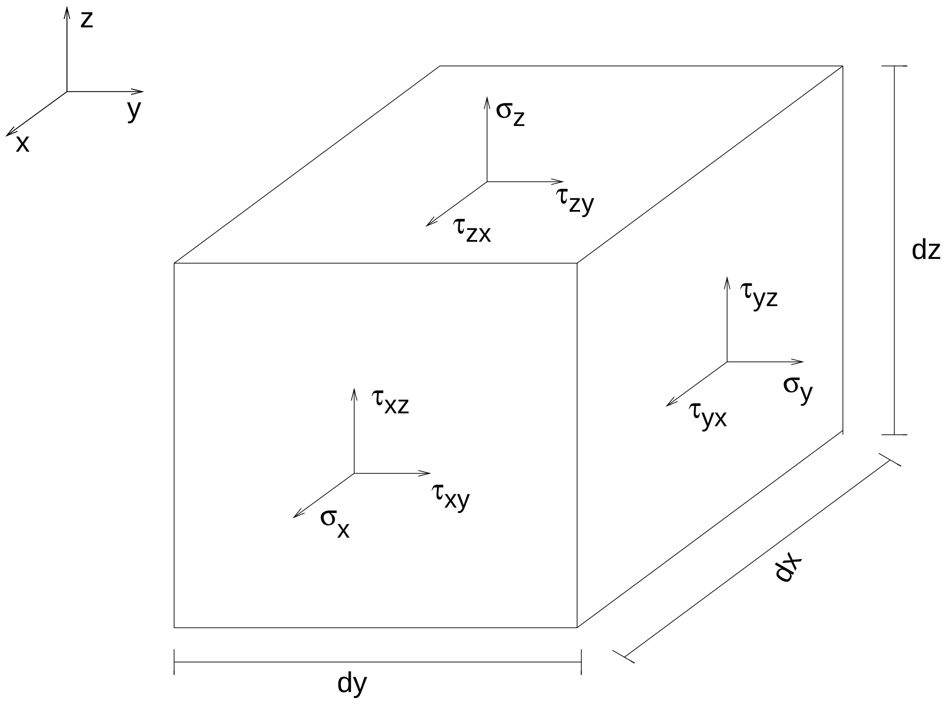

Figure 2.7: Forces acting on a single element

Considering static equilibrium, body and contact forces within the body and agitating forces acting on the body surface summate to zero. The body force in the present context is simply the gravitational force. The relationship between agitating forces and stresses within the body is expressed by

$$
\begin{aligned}
\frac{\partial \sigma_x}{\partial x} + \frac{\partial \tau_{xy}}{\partial y} + \frac{\partial \tau_{xz}}{\partial z} \quad +F_x &= 0 \\
\frac{\partial \tau_{yx}}{\partial x} + \frac{\partial \sigma_y}{\partial y} + \frac{\partial \tau_{yz}}{\partial z} \quad +F_y &= 0 \\
\frac{\partial \tau_{zx}}{\partial x} + \frac{\partial \tau_{zy}}{\partial y} + \frac{\partial \sigma_z}{\partial z} \quad +F_z &= 0 \\
\\
\mathbf{A^T}\boldsymbol{\sigma} \qquad\qquad +\mathbf{F} &
\end{aligned}
\tag{2.68}
$$

whereby σ and τ denote the normal stress and the shear stress, respectively. Agitating forces are denoted by F. Fig. 2.7 shows the corresponding forces acting on a single element.

These three equations must be satisfied at all points in the body. The right-hand side of these equations is zero due to the assumption of static equilibrium. For the solution of the above-mentioned equations it is necessary to determine the three displacements, the six strain components and the six independent stress components. The strains from the corresponding displacements are computed by the finite element method. The equilibrium condition alone yields only three equations, whereas a total of six equations must be solved for the stress components. The missing equations are provided by the constitutive equations.

In a finite element model the body is divided into single elements forming a mesh. The stresses and strains are calculated at spatial points within these elements by using Eqs. 2.66-2.68. A description of the finite elements used for the spatial discretization and the method of solution of the above-mentioned equations are presented in the following Chapters.

2.3.1.1 The wedge element

The sediment transport and flow models are based on a mesh comprised of triangular elements. A mesh of wedge elements (Fig. 2.8) is used for the three-dimensional

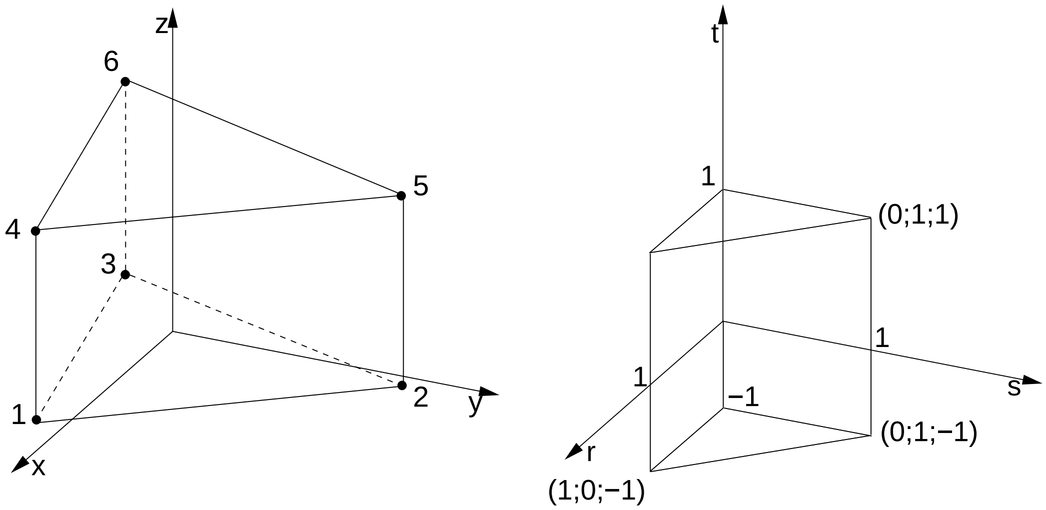

Figure 2.8: Wedge element, global (left) and local (right) coordinates

computation of flow. These prismatic elements are merely extruded from the mesh of triangles used for the two-dimensional computation of sediment transport. Both meshes make use of the same information regarding element connectivity and mesh point locations on a horizontal plane. The same wedge elements are also implemented at a later stage in the three-dimensional soil model. The shape functions of the three-dimensional wedge element are given by (Zienkiewicz and Taylor, 2000):

$$\begin{array}{ll} N_1 = \frac{1}{2}(1-r-s)(1+t) & N_4 = \frac{1}{2}(1-r-s)(1-t) \\ N_2 = \frac{1}{2}r(1+t) & N_5 = \frac{1}{2}r(1-t) \\ N_3 = \frac{1}{2}s(1+t) & N_6 = \frac{1}{2}s(1-t) \end{array} \tag{2.69}$$

Forming the derivatives of the shape functions leads to:

$$\nabla N = \left\{ \begin{array}{cccccc} \frac{\partial N_1}{\partial r} & \frac{\partial N_2}{\partial r} & \frac{\partial N_3}{\partial r} & \frac{\partial N_4}{\partial r} & \frac{\partial N_5}{\partial r} & \frac{\partial N_6}{\partial r} \\ \frac{\partial N_1}{\partial s} & \frac{\partial N_2}{\partial s} & \frac{\partial N_3}{\partial s} & \frac{\partial N_4}{\partial s} & \frac{\partial N_5}{\partial s} & \frac{\partial N_6}{\partial s} \\ \frac{\partial N_1}{\partial t} & \frac{\partial N_2}{\partial t} & \frac{\partial N_3}{\partial t} & \frac{\partial N_4}{\partial t} & \frac{\partial N_5}{\partial t} & \frac{\partial N_6}{\partial t} \end{array} \right\}$$

$$= \frac{1}{2} \left[\begin{array}{cccccc} -(1+t) & (1+t) & 0 & -(1-t) & (1-t) & 0 \\ -(1+t) & 0 & (1+t) & -(1-t) & 0 & (1-t) \\ (1-r-s) & r & s & -(1-r-s) & -r & -s \end{array} \right] \tag{2.70}$$

2.3.1.2 Numerical integration

The numerical integration of the shape functions (Eq. 2.69) or their derivatives (Eq. 2.70) is performed using the Gauss quadrature method. The desired functions for an element are evaluated at the Gauss points. Summing up the single values and multiplying them by their weightings yields the integral over the element area. All quadrature rules take the form:

$$\int_{-1}^{1} f(r)dr = \sum_{i=1}^{N_{G,r}} W_i(r_i)f(r_i) \tag{2.71}$$

Here, W_i is the weighting function at the coordinate position r_i within the element. Extending the quadrature method to three dimensions leads to the following expression (Eq. 2.72):

$$\int_{-1}^{1}\int_{-1}^{1}\int_{-1}^{1} f(r,s,t)\ dr\ ds\ dt = \sum_{i=1}^{N_{G,r}}\sum_{j=1}^{N_{G,s}}\sum_{k=1}^{N_{G,t}} W_i(r_i)W_j(s_j)W_k(t_k)f(r_i,s_j,t_k) \tag{2.72}$$

For a wedge element the location of the Gauss points and the corresponding weightings are as followed (Ratke et al., 1996):

	GP1	GP2	GP3	GP4	GP5	GP6	GP7	GP8
r	1/3	3/5	1/5	1/5	1/3	3/5	1/5	1/5
s	1/3	1/5	3/5	1/5	1/3	1/5	3/5	1/5
t	$\sqrt{1/3}$	$\sqrt{1/3}$	$\sqrt{1/3}$	$\sqrt{1/3}$	$-\sqrt{1/3}$	$-\sqrt{1/3}$	$-\sqrt{1/3}$	$-\sqrt{1/3}$
W_iW_j	-9/32	25/96	25/96	25/96	-9/32	25/96	25/96	25/96
W_k	1	1	1	1	1	1	1	1

Table 2.3: Gauss point locations and weightings

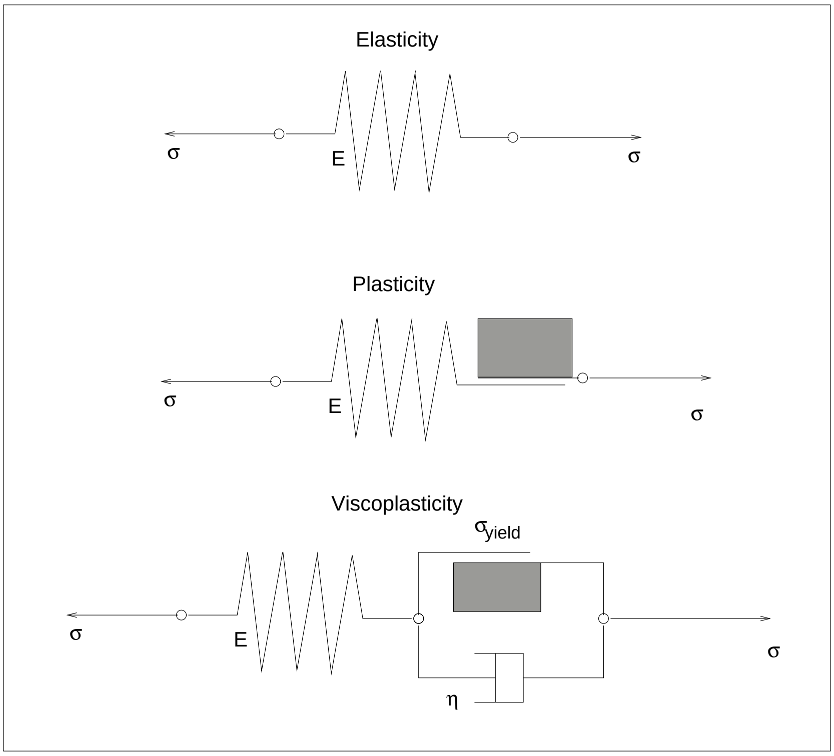

Figure 2.9: Rheological models

2.3.2 Constitutive equations

While the kinematic equations relate strain to displacement gradients, and the equilibrium equations relate stress to the applied forces at the boundary, the constitutive equations relate the applied stresses to strains. These equations take into account the considered material and it's physical parameters. The constants in these equations express the behaviour of the material under the action of stress.

In the following chapter the equations for an isotropic, elastic material are presented. As anisotropic material is not considered in the present study, the equations for this case are omitted.

2.3.2.1 Linear elasticity

Elasticity describes the behaviour of a material that undergoes a deformation under the action of stress and returns to its original form once the stress is removed.

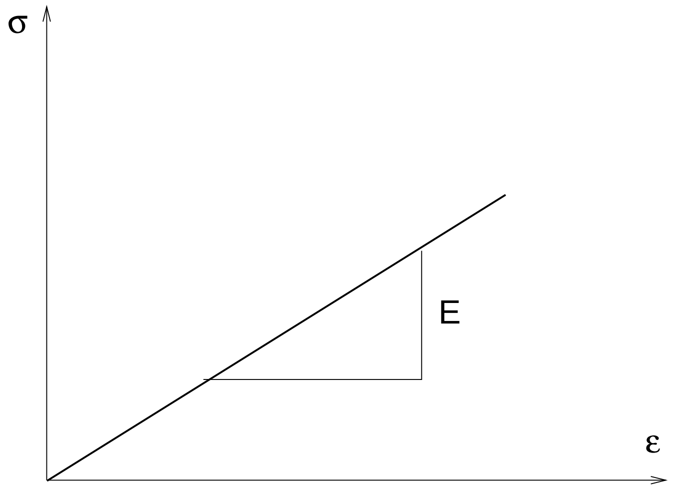

Figure 2.10: Linear elastic material behaviour

If strain and stress are related by a linear function, this is referred to as linear elasticity and may be described by *Hooke's* law (Eq. 2.73). Here, σ is the stress acting on the material, ε is the strain and E is the elasticity modulus (also known as Young's modulus). The rheological model (Fig. 2.9) is a spring with a designated stiffness E. The shear may be calculated by means of Eq. 2.74, where G is the shear modulus and γ is the twist angle.

$$\sigma = E\,\varepsilon \tag{2.73}$$

$$\tau = G\,\gamma \tag{2.74}$$

Another important material parameter is *Poisson's* ratio, which describes the contraction in the lateral direction when a material is extended. In Eq. 2.75, ν_P is *Poisson's* ratio, which is the ratio of the longitudinal strain ε_l to the transverse strain ε_t.

$$\nu_P = \frac{\varepsilon_l}{\varepsilon_t} \tag{2.75}$$

For an isotropic elastic material (i.e., an elastic material for which the properties are the same in all directions) there are only two independent material constants.

The relationship between these three moduli are given by the equation

$$G = \frac{E}{2(1+\nu_P)} \tag{2.76}$$

In a three-dimensional, rectangular Cartesian coordinate system the six equations of *Hooke's* law take the form (Timoshenko and Goodier, 1951)

$$\begin{array}{ccccc}
\begin{bmatrix} \sigma_x \\ \sigma_y \\ \sigma_z \\ \tau_{xy} \\ \tau_{yz} \\ \tau_{xz} \end{bmatrix} & = & \frac{E}{(1+\nu_P)(1-2\nu_P)} & \begin{bmatrix} 1 & \nu_P & \nu_P & 0 & 0 & 0 \\ \nu_P & 1 & \nu_P & 0 & 0 & 0 \\ \nu_P & \nu_P & 1 & 0 & 0 & 0 \\ 0 & 0 & 0 & \frac{1-\nu_P}{2} & 0 & 0 \\ 0 & 0 & 0 & 0 & \frac{1-\nu_P}{2} & 0 \\ 0 & 0 & 0 & 0 & 0 & \frac{1-\nu_P}{2} \end{bmatrix} & \begin{bmatrix} \epsilon_x \\ \epsilon_y \\ \epsilon_z \\ \gamma_{xy} \\ \gamma_{yz} \\ \gamma_{xz} \end{bmatrix} \\
\boldsymbol{\sigma} & = & & \mathbf{D} & \boldsymbol{\varepsilon}
\end{array} \tag{2.77}$$

2.3.2.2 Material nonlinearity

The linear elasticity described in the foregoing chapter is only valid for a very idealised case in which the agitating forces acting on a body lie in a particular range. The behaviour of the material outside this range is no longer linear and fully reversible. Instead, the relationship between stress and strain is a complicated function containing coefficients in the equations that depend on the solution. As the material begins to flow, parts of the deformations are permanent. Fig. 2.11 shows the behaviour of a perfectly plastic material. The flow is constant when reaching the corresponding critical stress state is attained. No hardening or softening of the material occurs. This behaviour is not taken into account in the present study because the considered (sandy) material does not exhibit these effects.

Considering the process of nonlinear material behaviour in a finite element analysis leads to a more complex analytical problem than in the case of material linearity. Two main solution procedures exist for this problem. The first method implements a once-only constructed stiffness matrix which is identical to the matrix for the linear elastic case. Nonlinearity is taken into account by iteratively

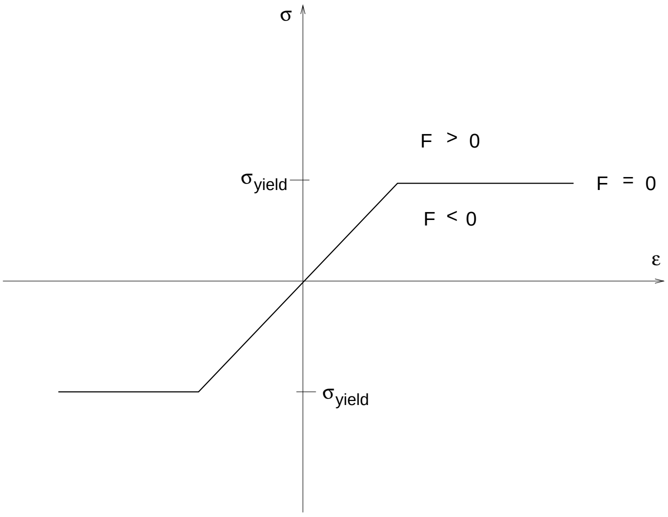

Figure 2.11: Elastic - prefectly plastic material behaviour

increasing the (external) load vector, whereby each single iteration involves an elastic analysis.

$$\varepsilon = \varepsilon_e + \varepsilon_p \tag{2.78}$$

The total strain of a yielding material (Eq. 2.78) is the sum of recoverable strains ε_e, which may be described by the theory of linear eleasticity, and the irrecoverable strains ε_p, which are present after unloading. The latter must be calculated by a method suitable for describing plastic material behaviour (see Chapter 2.3.2.6).

2.3.2.3 Invariants

The stress tensor expressed in Cartesian coordinates is defined as

$$\begin{Bmatrix} \sigma_x & \tau_{xy} & \tau_{xz} \\ \tau_{yx} & \sigma_y & \tau_{yz} \\ \tau_{zx} & \tau_{zy} & \sigma_z \end{Bmatrix} \tag{2.79}$$

This is equivalent to the principal stress tensor (Eq. 2.80), which defines the maximum and minimum normal stresses in a plane. These are always perpendicular to each other and oriented in directions in which the shear stresses are zero.

$$\{\sigma_1 \; \sigma_2 \; \sigma_3\} \tag{2.80}$$

Although the principal stresses give the magnitude of the stresses acting at a point, a disadvantage of this tensor is the need for information on how the coordinate system is oriented in physical space. The use of invariants is therefore often more practical than the use of principal stresses. Invariants are scalar functions of tensors that have the same values regardless of which coordinate system they are referenced to. Using the notation of Smith and Griffiths (1998), the invariants are given by

$$\begin{aligned} s &= \tfrac{1}{\sqrt{3}}\left(\sigma_x + \sigma_y + \sigma_z\right) \\ t &= \tfrac{1}{\sqrt{3}}[(\sigma_x - \sigma_y)^2 + (\sigma_y - \sigma_z)^2 + (\sigma_z - \sigma_x)^2 + \\ &\quad 6\tau_{xy}^2 + 6\tau_{yz}^2 + 6\tau_{xz}^2]^{\frac{1}{2}} \\ \theta &= \tfrac{1}{3}arcsin\left(\tfrac{-3\sqrt{6}J_3}{t^3}\right) \end{aligned} \tag{2.81}$$

where s denotes the distance from the origin of the coordinate system to the plane (Fig. 2.12) in which the considered point is located, t is the perpendicular distance of the point from the space diagonal and θ is the Lode angle which gives the angular position of the point in the plane. The required J_3 and s_i are defined by

$$J_3 = s_x s_y s_z - s_x\tau_{yz}^2 - s_y\tau_{zx}^2 - s_z\tau xy^2 + 2\tau_{xy}\tau_{yz}\tau_{zx} \tag{2.82}$$

and

$$s_x = \left(2\sigma_x - \sigma_y - \sigma_z\right)/3, \; etc. \tag{2.83}$$

As the given invariants (Eq. 2.81) have no physical meaning, a more expressive formulation is given by Eq. 2.84. Here, σ_m is the mean stress and $\bar{\sigma}$ is the stress contained in the deviatoric tensor. The invariants in this form are adopted in the following chapters.

$$\begin{aligned} \sigma_m &= \tfrac{s}{\sqrt{3}} \\ \bar{\sigma} &= t\sqrt{\tfrac{3}{2}} \end{aligned} \tag{2.84}$$

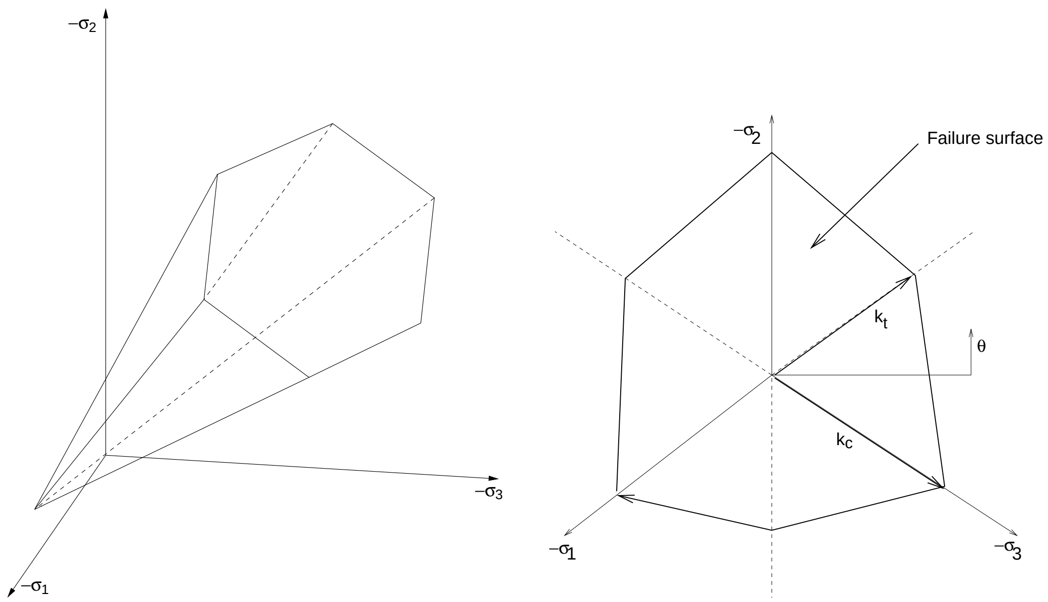

Figure 2.12: Mohr-Coulomb failure criterion

The principal stresses and invariants are related to each other by the following equations:

$$\begin{aligned}
\sigma_1 &= \sigma_m + \tfrac{2}{3}\bar{\sigma} sin(\theta - \tfrac{2\pi}{3}) \\
\sigma_2 &= \sigma_m + \tfrac{2}{3}\bar{\sigma} sin\theta \qquad (2.85) \\
\sigma_3 &= \sigma_m + \tfrac{2}{3}\bar{\sigma} sin(\theta + \tfrac{2\pi}{3})
\end{aligned}$$

2.3.2.4 Failure criterion

In order to describe the plastic behaviour of soil a criterion is required to distinguish between the material in a state of elastic deformation or plastic deformations. Several criteria have been developed which are suitable for different kinds of material. They may be distinguished from each other by the form of the yield surface in the principle stress space. Fig. 2.12 shows the criterion of Mohr-Coulomb, which provides an adequate description of the plastic behaviour of sandy soil. As the latter depends on the first and third principle stresses, it takes the form of an irregular hexagonal cone. Using the friction law

$$\tau = c - \sigma \tan\phi \tag{2.86}$$

the Mohr-Coulomb failure criterion may be written as

$$\frac{\sigma_1 + \sigma_3}{2} \sin\phi - \frac{\sigma_1 - \sigma_3}{2} - c \cos\phi \tag{2.87}$$

where c is the cohesion factor, ϕ is the friction angle and $\sigma_1 > \sigma_2 > \sigma_3$. Substituting Eqs. 2.85 into Eq. 2.87 leads to the following expression for the Mohr-Coulomb criterion:

$$F = \sigma_m \sin\phi + \bar{\sigma} \left(\frac{\cos\theta}{\sqrt{3}} - \frac{\sin\theta \sin\phi}{3} \right) - c \cos\phi \tag{2.88}$$

The form of the hexagonal cone is defined by k_t and k_c (Fig. 2.12) (Findeiß, 2001). The latter are dependent on the cohesion factor and the friction angle, and are defined by

$$\begin{aligned} k_t &= \frac{2\sqrt{6}\, c \cos\phi}{3 + \sin\phi} \\ k_c &= \frac{2\sqrt{6}\, c \cos\phi}{3 - \sin\phi} \end{aligned} \tag{2.89}$$

When the stress reaches the yield surface, the associated plastic flow leads to physically unrealistic volumetric expansion or dilation (Smith and Griffiths, 1998). In this case, the non-associated flow rule is applied. The plastic strain is then described by a plastic potential function Q, which is geometrically identical to the yield function F. In this case, however, the dilation angle ψ is used instead of the friction angle ϕ. Difficulties arise in the determination of the derivative of Eq. 2.96. Because the form of the Mohr-Coulomb yield surface is non-continuous, the derivative in Eq. 2.96 becomes indeterminate. This occurs when the Lode angle $\theta = \pm 30°$. In order to ensure numerical stability the hexagonal surface is replaced by a conical surface. When the following condition holds

$$|\sin\theta| > 0.49 \tag{2.90}$$

the value for the Lode angle in Eq. 2.88 is replaced by $\theta = 30°$ or $\theta = -30°$, depending on the sign of θ.

2.3.2.5 Body-loads

Using algorithms with a repeated elastic solution, such as the constant stiffness method, it is necessary to redistribute the loads acting on the system in order to achieve convergence (Smith and Griffiths, 1998). The small load increments involved in such algorithms lead to a system of equations whose solution yields small increments of displacement (Eq. 2.91). Here, K is the stiffness matrix and p are the internal and external loads. The index i denotes the number of iterations.

$$K\delta^i = p^i \tag{2.91}$$

In order to obtain the total strain increments of the system the displacements of each element u are extracted from the system displacement vector δ and then calculated via the strain-displacement relationship

$$\Delta\varepsilon^i = Bu^i \tag{2.92}$$

In regions where the stress is beyond the yield surface the total strains include an elastic and a visco-plastic component, as expressed by

$$\Delta\varepsilon^i = (\Delta\varepsilon^e + \Delta\varepsilon^{vp}) \tag{2.93}$$

Considering only the elastic strain increments $\Delta\varepsilon^e$, the corresponding stresses can easily be calculated using the stress-strain relationship

$$\Delta\sigma^i = D^e\left(\Delta\varepsilon^e\right) \tag{2.94}$$

The stress increments from Eq. 2.94 are then added to the already existing increments from the previous load step, and the actual stress acting on the system may be used in the failure criterion equations. In case of stress redistribution the load vector p (Eq. 2.91) is altered. The load vector itself is comprisd of two different types of load (Eq. 2.95), namely the actual load increment p_a and the body-load increment p_b, which change with each iteration.

$$p^i = p_a + p_b^i \tag{2.95}$$

Commonly used methods for calculating the body-loads are the initial stress method and the method of visco-plasticity (also referred to as the initial strain method). The latter method, which was adopted in the present study, is described in the following chapter.

2.3.2.6 Visco-plasticity

Taking a viscous or a visco-plastic material behaviour into account leads to a time-dependent relationship between strains and displacements. This may be illustrated by means of a damper with a relaxation time in the rhelogical model (Fig. 2.9). A fundamental description of the theory of visco-plasticity may be found in Perzyna (1966), Perzyna (1971) or Zienkiewicz and Cormeau (1974). The approach of Zienkiewicz and Cormeau (1974) was used by Smith and Griffiths (1998) to formulate a numerical algorithm which is implemented in the present study. When simulating and analysing soil strains and displacements under saturated conditions, a pronounced time-dependency exists, which is mainly due to transport processes such as the flow of pore fluid. The cases considered in the foregoing are all under saturated conditions with a flow acting on the upper surface of the bed. It is therefore necessary to take the time-dependency of the process into account. This is realised in the constitutive equations in the form of visco-plasticity. As an alternative, this process could be modelled as a two-phase process involving the soil and the pore fluid flow.

In the method of Zienkiewicz and Cormeau (1974) the material is allowed to attain a stress state beyond the failure criterion (Fig. 2.12). In contrast to the elasto-plasticity, whereby the stress is immediately redistributed within the computational mesh to force the stresses to reach the failure surface, stresses beyond the failure surface are permitted for a small period of time. These are the visco-plastic strains that are related to the amount by which the yield has been violated by

$$\dot{\varepsilon}^{VP} = F \frac{\partial Q}{\partial \sigma} \tag{2.96}$$

where $\dot{\varepsilon}^{VP}$ is the visco-plastic strain, σ is the stress and $Q = Q(\sigma, q)$ is the plastic potential function that describes the material behaviour in the case of plasticity (e.g. softening, hardening or ideal plasticity). The time-dependency is taken into account by summating the increments of the visco-plastic strain rate (Eq. 2.96) at each time step. This may be expressed by

$$\left(\delta\varepsilon^{VP}\right)^i = \Delta t \left(\dot{\varepsilon}^{VP}\right)^i \tag{2.97}$$

and

$$\left(\Delta\varepsilon^{VP}\right)^i = \left(\Delta\varepsilon^{VP}\right)^{i-1} + \left(\delta\varepsilon^{VP}\right)^i \tag{2.98}$$

The time step Δt as derived by Cormeau (1975), is a pseudo time step which varies for different soil materials in order to achieve numerical stability. The time step for "von Mises" materials is

$$\Delta t = \frac{4\,(1+\nu_P)}{3\,E} \tag{2.99}$$

and for Mohr-Coulomb materials

$$\Delta t = \frac{4\,(1+\nu_P)(1-2\nu_P)}{E(1-2\nu_P+\sin^2\phi)} \tag{2.100}$$

In order to calculate the visco-plastic strain rates the derivatives of the plastic potential function with respect to the stresses are required. These are expressed by

$$\frac{\partial Q}{\partial \sigma} = \frac{\partial Q}{\partial \sigma_m}\frac{\partial \sigma_m}{\partial \sigma} + \frac{\partial Q}{\partial J_2}\frac{\partial J_2}{\partial \sigma} + \frac{\partial Q}{\partial J_3}\frac{\partial J_3}{\partial \sigma} \tag{2.101}$$

with the invariant $J_2 = 1/2\,t^2$. In a numerical model the visco-plastic strain rate (Eq. 2.96) is calculated acording to

$$\dot{\varepsilon}^{VP} = F\left(DQ1\;M^1 + DQ2\;M^2 + DQ3\;M^3\right)\sigma \tag{2.102}$$

Here, $M^1\sigma$, $M^2\sigma$ and $M^3\sigma$ are vectors that represent $\partial\sigma_m/\partial\sigma$, $\partial J_2/\partial\sigma$ and

$\partial J_3/\partial\sigma$, while $DQ1$,$DQ2$ and $DQ3$ are scalars equal to $\partial Q/\partial\sigma_m$, $\partial Q/\partial J_2$ and $\partial Q/\partial J_3$, respectively (Smith and Griffiths, 1998; Zienkiewicz and Taylor, 2000).

The body-loads p_b^i (see Chapter 2.3.2.5) are then calculated by

$$p_b^i = p_b^{i-1} + \sum_{element} \int B^T D^e (\delta\varepsilon^{VP})^i \; d(element) \tag{2.103}$$

The body-loads are accumulated at each pseudo time step at for all elements that contain a yielding Gauss point. This is an iterative process which is repeated until no point violates the yield surface within a given tolerance.

2.3.3 Solution strategies

2.3.3.1 Constant stiffness matrix

Denoting the previously mentioned equilibrium, strain-displacement and constitutive equations by their abridged forms as already introduced in Eqs. 2.68, 2.67 and 2.77, the three sets of equations are represented by

$$\begin{aligned} \mathbf{A^T}\boldsymbol{\sigma} &= -\mathbf{F} \\ \boldsymbol{\sigma} &= \mathbf{D}\boldsymbol{\varepsilon} \\ \boldsymbol{\varepsilon} &= \mathbf{Au} \end{aligned} \tag{2.104}$$

where $\mathbf{A}$ is the strain-displacement operator, $\boldsymbol{\sigma}$ is the stress tensor, $\mathbf{D}$ is the constitutive stress-strain relationship, $\boldsymbol{\varepsilon}$ are the strains and $\mathbf{u}$ the displacements. The purpose of the numerical model is to calculate the displacements (and hence the strains) for a given stress resulting from gravity and external loads. The above-mentioned set of equations is solved by eliminating $\boldsymbol{\sigma}$ and $\boldsymbol{\varepsilon}$ from Eq. 2.104. This is carried out by inserting the third equation from the set of Eqs. 2.104 into the second equation and the result of the latter into the first equation:

$$\begin{aligned} \mathbf{A^T}\boldsymbol{\sigma} &= -\mathbf{F} \\ \mathbf{A^T D}\boldsymbol{\varepsilon} &= -\mathbf{F} \\ \mathbf{A^T DAu} &= -\mathbf{F} \end{aligned} \tag{2.105}$$

The result of this elimination process is a set of partial differential equations which are dependent on the continuous space variables u,v and w. In order to solve these equations the considered body is discretized by finite elements such as the prismatic element described in Capter 2.3.1.1. The continuous variables are then replaced by the appropriate shape functions.

$$u_i = [N_1\ N_2\ N_3\ N_4\ N_5\ N_6] \begin{bmatrix} u_{i,1} \\ u_{i,2} \\ u_{i,3} \\ u_{i,4} \\ u_{i,5} \\ u_{i,6} \end{bmatrix} = \mathbf{Nu} \tag{2.106}$$

In Eq. 2.106, N_k are the shape functions and $i = x, y, z$.

Discretization of the continuous variables must be taken into account for the strain-displacement operator. Expressing the shape functions in matrix form yields

$$\mathbf{S} = \begin{bmatrix} \mathbf{N}_u & 0 & 0 \\ 0 & \mathbf{N}_v & 0 \\ 0 & 0 & \mathbf{N}_w \end{bmatrix} \tag{2.107}$$

$$\mathbf{N}_u = \mathbf{N}_v = \mathbf{N}_w = [N_1\ N_2\ N_3\ N_4\ N_5\ N_6]$$

After inserting the latter into Eq. 2.105, the last step is to integrate the shape functions (Chapter 2.3.1.2) over space. This leads to the stiffness matrix for the considered body (Eq. 2.108).

$$\mathbf{M_S} = \int\int\int \mathbf{AS^T D(AS)}\, dx\, dy\, dz = \int\int\int \mathbf{B^T DB}\, dx\, dy\, dz \tag{2.108}$$

The result is a system of linear equations (Eq. 2.109) comprised of the stiffness matrix, the external loads, and the displacement vector, which must be solved for the system. The resulting displacements may then be used to calculate the corresponding strains and stresses within the body.

$$\mathbf{M_S}\,\mathbf{u} = -\mathbf{F} \tag{2.109}$$

2.3.3.2 Element-by-element techniques

Regardless of whether the stability analysis is linear or nonlinear, it is necessary to solve a system of linear equations (Eq. 2.109). This generally takes the form

$$\mathbf{A}\mathbf{x} = \mathbf{b}$$

where $\mathbf{A}$ is the coefficient matrix, $\mathbf{b}$ is the result vector and $\mathbf{x}$ is the vector containing the unknown system variables. A solution method such as the Gaussian elimination method could then be applied to calculate $\mathbf{x}$. This would require a system matrix for the entire computational domain, however. Assembling a matrix for the whole system even using special storage schemes such as the skyline technique (Bathe, 1996) would be far too expensive, especially for the three-dimensional case. In view of this, the element-by-element technique was implemented as an alternative method in the present study in order to ensure that the required memory space is limited to a manageable size. The algorithm used with this technique is based on the method of conjugate gradients described by Jennings and McKeown (1992).

The steps outlined in the following equation (Eq. 2.110) are performed k times in order to minimize the difference between $\mathbf{x}^{k+1}$ and $\mathbf{x}^{k}$.

$$\boxed{\begin{aligned} \mathbf{u}^k &= \mathbf{A}\mathbf{p}^k \\ \alpha^k &= \frac{(\mathbf{r}^k)^T\mathbf{r}^k}{(\mathbf{p}^k)^T\mathbf{u}^k} \\ \mathbf{x}^{k+1} &= \mathbf{x}^k + \alpha^k\mathbf{p}^k \\ \mathbf{r}^{k+1} &= \mathbf{r}^k - \alpha^k\mathbf{u}^k \\ \beta^k &= \frac{(\mathbf{r}^{k+1})^T\mathbf{r}^{k+1}}{(\mathbf{r}^k)^T\mathbf{r}^k} \\ \mathbf{p}^{k+1} &= \mathbf{r}^{k+1} + \beta^k\mathbf{p}^k \end{aligned}} \tag{2.110}$$

where the initial value for $\mathbf{p}$ is calculated according to

$$\mathbf{p}^0 = \mathbf{b} - \mathbf{A}\mathbf{x}^0$$

The vector $\mathbf{x}$ is initialized with a value that should be as close as possible to the final solution in order minimize the number of iterations. In all operations except the first in Eq. 2.110 only vectors and scalars are involved. The first operation is a matrix-vector multiplication, which is performed according to the above-mentioned element-by-element technique. By this means, the local products of the $\mathbf{p}$ vector and the element stiffness matrix i are assembled consecutively to form the global result vector. Summing up the local results leads to the global results:

$$\mathbf{u} = \sum \mathbf{M}_{\mathbf{S},i}\, \mathbf{b}_i \tag{2.111}$$

2.3.3.3 Boundary conditions

A solution of the matrix given in Chapter 2.3.3.1 also requires the specification of boundary conditions in order to obtain a solution. The specification of boundary conditions in the considered experiments is fairly simply in so far as a mesh point is either allowed to move in a spatial direction or not. In the case that a mesh point is fixed the result is known to be zero. The line and column in the matrix corresponding to the node and spatial direction for a non-moving boundary condition may thus be neglected as these are not required for the solution of the other components of the matrix. In the case a boundary node which is allowed to move in a spatial direction, the contributions for this node are retained in the matrix and the system of equations.

In practice there are two alternative ways of treating the above-mentioned boundary condition for a fixed node. The first variant is to eliminate the corresponding line and column from the system of equations so that they are not taken into account at all. The variable is then simply set to zero. As an alternative the (non-zero) value of a variable may be prescribed by adding a large number (e.g. 10^{20}) to the leading diagonal of the stiffness matrix in the row corresponding to the considered variable. Additionally, the value of the **b** vector in that row must be modified by multiplying it with the adapted stiffness term (Eq. 2.112).

$$\left(M_{i,j} + 10^{20}\right) \phi + [\text{small terms}] = [\text{prescribed value}] \times \left(M_{i,j} + 10^{20}\right) \qquad (2.112)$$

As a result the considered variable will take the value $\phi = [\text{prescribed value}]$, provided the [small terms] are negligible compared to the large term added. This has the advantage that not only zero but any arbitrary value may be prescribed at a given meshpoint.

Boundary conditions involving gradients of the unknown are not discussed here as they are not required in the experiments considered in Chapter 3.

2.3.4 Influence of pressure on soil stability

Considering wave-induced scour as outlined in Chapter 3.2 leads to the question of the influence of wave pressure loading on soil stability. The soil consists of small particles, whereby the stresses resulting from gravity and external loads are transferred by normal stresses across the particle contact surfaces. Shear forces can only exist as friction between the contact surfaces when a normal stress is present. As the soil is saturated, the voids between the soil particles are filled with water. In a natural environment it is likely that small amounts of gas are present in the pores (Tørum, 2007). The gas is considered to be part of the liquid and can be taken into account by altering the compressibility of the fluid (de Groot et al., 2006). Normal forces are not only transferred by the soil particles but also by the pore water. This means that the effective normal stress consists of the total normal stress from the soil skeleton and the pore pressures. In the event that the pore pressure increases and becomes equal to the total normal stress, the effective normal stress becomes zero. Consequently, shear forces can no longer be transferred. Water and sediment then convert from a former solid state into a liquefied state. This liquefaction may not only be caused by increased pore pressure but also by a decrease in the total stress.

In a maritime environment the described behaviour is basically due to two different effects. The first of these effects is due to wave-induced momentary pressure variation which propagates into the soil and compresses and decompresses the fluid/gas mixture. The second effect is due to a decrease in the pore space with no or only slight drainage of the pore fluid. This causes a gradual increase in the pore pressure, which results in a residual pressure contribution which may possibly neutralise the total normal stress. The latter effect is a result of the movement or rearrangement of sediment particles in a loose soil. Liquefaction can only occur if the particle size distribution of the soil satisfies certain requirements. Firstly, the soil must be fine enough in order to prevent drainage of the fluid while pore pressure is accumulated, and secondly, it must be non-cohesive in order that particles can move and rearrange freely. The range of particle sizes which allows liquefaction to occur is shown in Fig. 2.13.

Momentary liquefaction only occurs if the pore fluid is compressible, i.e. a small amount of gas must be present in the fluid. Otherwise, the reduction in the effective stress is insufficient to cause a momentary liquefaction, even directly below the soil surface (de Groot et al., 2006). On the contrary, the compressible nature of the fluid permits the flow and storage of additional water in the pores when the external pressure increases (under the crest). When the pressure reduces (under the trough) the additional fluid causes an increased pressure in the pores which lowers the soil stability and may possibly lead to total liquefaction.

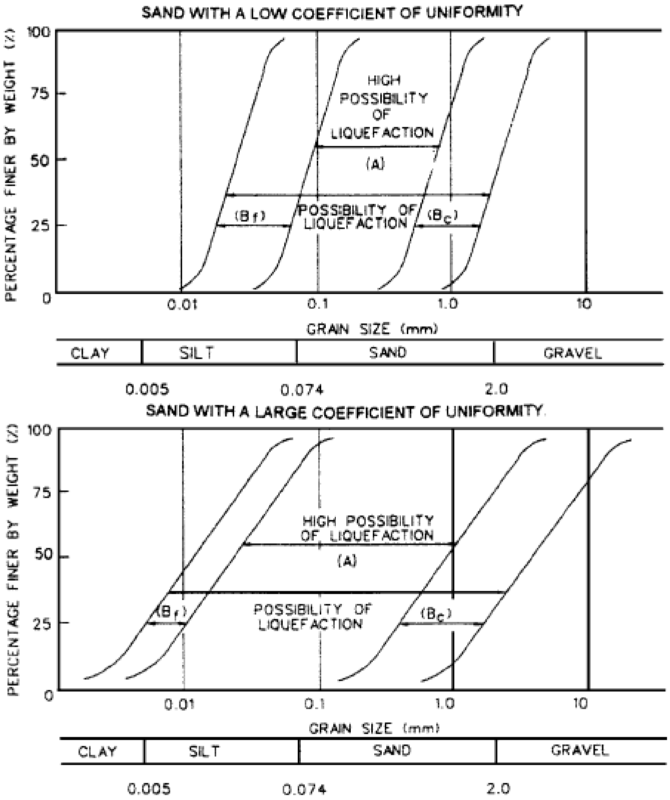

Figure 2.13: Risk of liquefaction as a function of particle size distribution (Damgaard et al., 2006)

Wave-induced liquefaction caused by a residual excess pore presssure was studied by Sumer et al. (2006b) in a wave flume. A loosely-packed silty sediment with a particle diameter of 0.06mm was placed in the flume and measurements of the pressure in the soil and the water depth were made. The results of liquefaction and compaction were extracted from videotape recordings made during the tests. The observations range from the point in time when waves are introduced up to the point of soil liquefaction and compaction and the occurrence of ripples on the bed. This time series is shown schematically in Fig. 2.14. Directly after the waves begin to propagate through the flume, the pressure in the soil pores begins to rise. The wave-induced cyclic shear stress causes the sediment particles to rearrange, which results in a decrease of pore volume and hence an increase of pore pressure. When the excess pore pressure (= the difference between the hydrostatic pressure and the actual pore pressure) attains the total normal stress, the soil liquefies and the water and soil behave like a liquid.

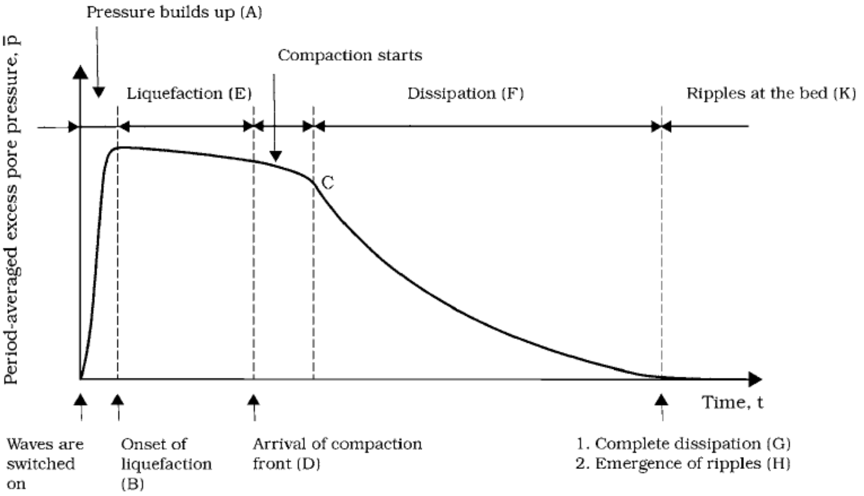

Figure 2.14: Time series of liquefaction and compaction (Sumer et al., 2006a)

The excess pore pressure increases in the vertical direction with a maximum at the impermeable base represented by the bottom of the sediment box in the considered experiment (cf. Fig. 2.15a). As a consequence, a vertical pressure gradient exists which drives the pore fluid upwards out of the soil. Reducing the amount of water in the pores leads to settlement and consolidation of the soil particles. This process begins at the lowest point of liquefaction and is followed by an upward movement of the compaction front (cf. Fig. 2.15b) until the mudline is reached. The process is accompanied by a decrease of pore pressure. The consolidation process additionally leads to a decrease in the height of the sediment layer.

The above-described process of liquefaction was simulated by Dunn et al. (2006) using a two-dimensional numerical model. The results were compared with an analytical solution as well as with the experiments of Teh et al. (2003). The model

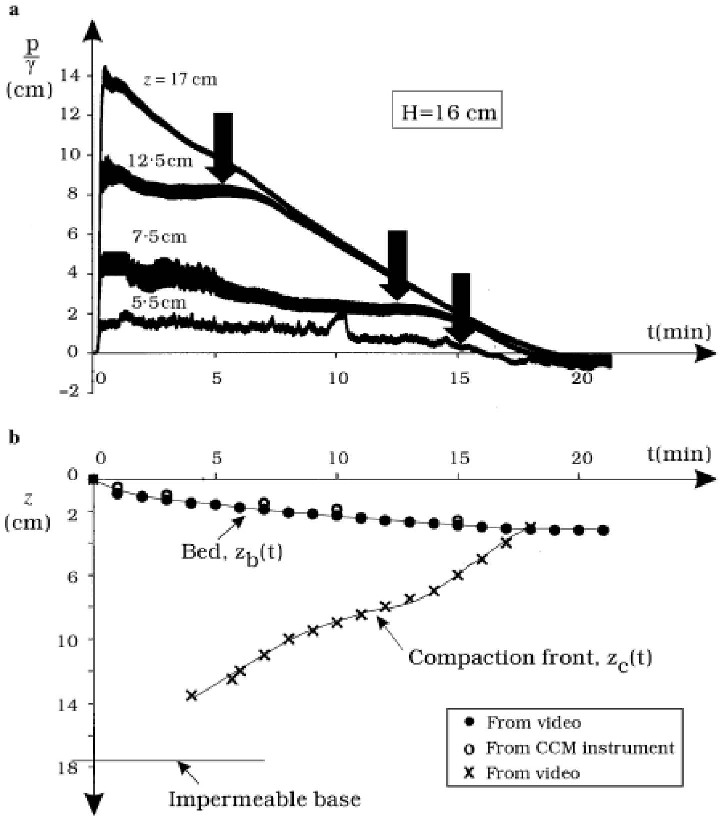

Figure 2.15: Pressure distribution (a) and depth of compaction front and soil surface (b) (Sumer et al., 2006b)

implements Biot's consolidation theory (1941) in order to calculate pore pressures and soil deformation. A detailed knowledge of the soil and its parameters is necessary in order to prescribe realistic boundary conditions for the numerical model. Although these data were available for the analytical solution as well as for the considered validation experiments, such detailed information is rare to find for soil in a natural environment or even for laboratory experiments. As such, the number of cases in which this type of model may be applied is severely limited.

2.4 Model coupling

Having described the individual models and the considered processes in the foregoing chapters, the interaction of the latter will now be examined in closer detail. The description which follows is valid for all of the conducted experiments given in Chapter 3.

All sediment transport and bottom evolution results are based on a flow period representative of the flow regime present at the structure concerned. In the case of a propagating wave this is clearly the wave period, whereas for a steady flow, this is the period of a wake separation. The periods are held constant for the entire scour simulation.

Prescribing regular waves as a boundary condition is carried out by calculating the wave properties by means of a suitable mathematical theory, as described in Appendix A. The imposed waves are of a periodic character, which means that a stable wave is always bounded by a preceding and a following equal wave. The first wave imposed cannot be used as a representative wave as it is not stable and is slowly damped while propagating through the channel. Tests showed that usually the third imposed wave is stable and gives good results with regard to the free surface and velocities. The first two waves are thus neglected and are not used for calculating sediment transport and bottom evolution. These are part of the initial phase, as outlined in Fig. 2.16.

In the case of a steady flow the current is gradually increased at the boundary in order to obtain the first result period. After calculating the bottom evolution for the first period the flow result from the previous run is projected onto the new geometry and then used as the initial value. In the following initial phase of the flow calculation the velocity adapts to the new (bottom geometry) conditions and the flow regime is reconstructed. Afterwards, the next representative period of flow is simulated and is used as input for the bottom evolution.

The result period obtained from the flow model is used repeatedly for calculating the bottom evolution. The number of iterations is limited on the one hand by the extent of bottom evolution, as the calculated shear stress is only valid for small deviations of the bottom geometry. On the other hand, a frequent recalculation of the flow is not possible as the flow simulation is comparatively time intensive.

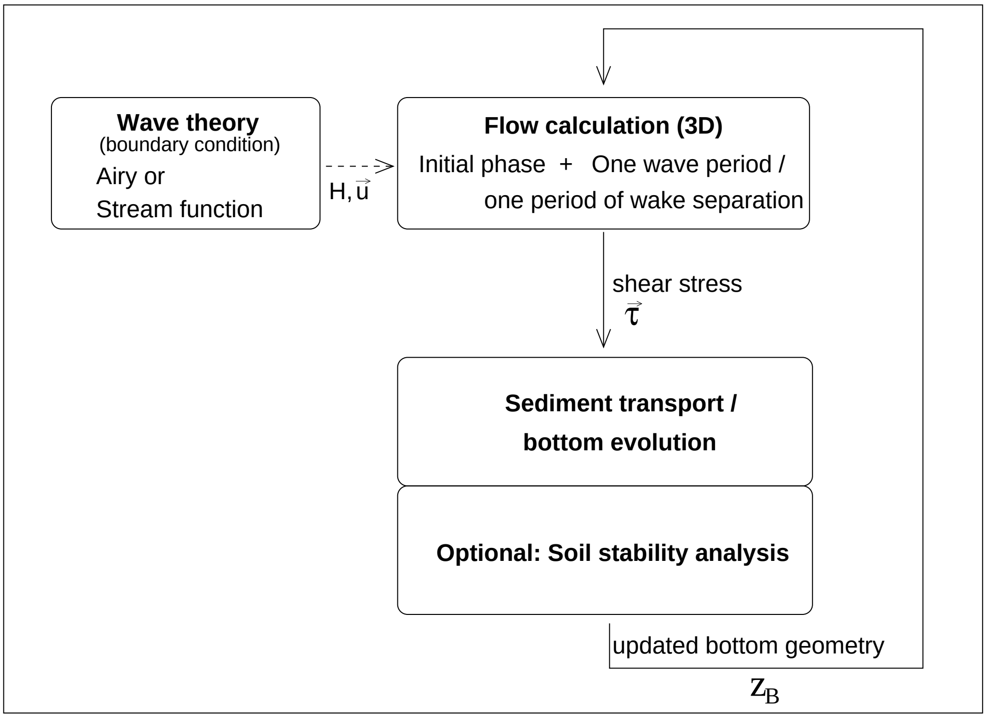

Figure 2.16: Model dependencies

How often a flow result is re-used is defined individually for the particular case concerned.

The resulting bottom geometry is then imported by the flow model and the mesh is adapted to the new conditions. Following the initial phase when the flow regime is reconstructed, a new period of flow results is calculated.

3 Numerical experiments and model validation

3.1 Flow-induced scour

3.1.1 Abutment

Local scour at abutments has been studied by Radice et al. (2006). A flow channel made of plexiglass (Fig. 3.1) with a length of 5.8m, a width of 40cm and a height of 16cm was used for this purpose. The effective duct height after installing roughness elements on the bottom upstream and downstream of the sediment basin was 15.5cm. The top of the channel was also covered with plexiglass so that the channel could be pressurised during the tests. Two different types of abutments were used, namely a vertical wall (Fig. 3.2) and a trapezoidal abutment with side lengths of 10cm and 8cm. The sediment used consisted of artificial cylinders made of PVC with a median equivalent diameter of 3.6mm. The uniformity coefficient was close to unity and the specific gravity of the sediment was $(\rho_s - \rho)/\rho = 0.43$. A water discharge of $Q = 18.5\, l/s$ was used in all of the conducted experiments. This was chosen to match the incipient motion of particles.

In this experiment the channel was covered with plexiglass. This was taken into account in the numerical model by freezing the free surface at the given water depth and prescribing a wall boundary condition. The cover as well as the side walls were assumed to be rough and a small Nikuradse roughness coefficient was prescribed at these boundaries. At the bottom the roughness coefficient was taken to be as three times the median particle diameter ($k_s = 3d_{50}$).

The numerical scour simulation was performed using different sediment transport rate equations. The reason for this is that the results were known to differ considerably depending on the equation used. The results obtained using the equation of Engelund and Fredsøe were found to agre well with the laboratory results regarding the scour depth at the nose of the abutment. The scour depth attained approximately 20cm in the laboratory as well as in the numerical experiment (cf. Fig. 3.4 and Fig. 3.3). The simulated geometry of the erosion channel of the right of the abutment was found to be too broad and too short, however (Fig. 3.7). The results obtained using the equation of Meyer-Peter and Müller on the other hand showed better agreement regarding the scour shape. The long erosion channel to the right of the abutment was similar to the measured shape. Unfortunately, the scour depth was underestimated by about 18%.

The scour depth at the corner of the abutment was not correctly predicted by the model regardless of the sediment transport equation used. This is possibly the result of the coarse spatial discretisation at this location, which was optimized to improve the efficiency of the computational scheme. The alternate calculation of flow and sediment transport may also contribute to this effect as well as the fact that an artificial sediment with an unnatural specific gravity was used in the experiments. The sediment transport rate equation and the equations for calculating incipient motion were derived from measurements and observations involving natural sediment particles with a much higher specific gravity. This means that the implemented equations are inappropriate for the artificial sediment used in the simulations.

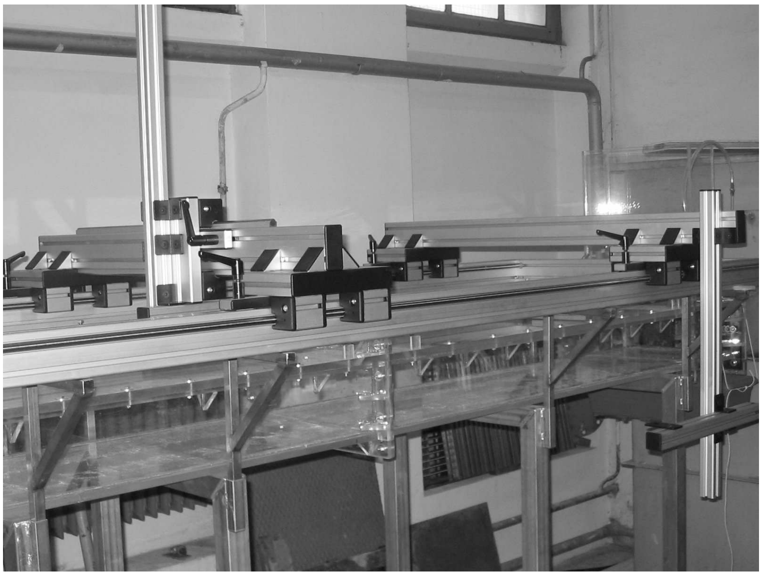

Figure 3.1: Flow channel (Ballio et al., 2006)

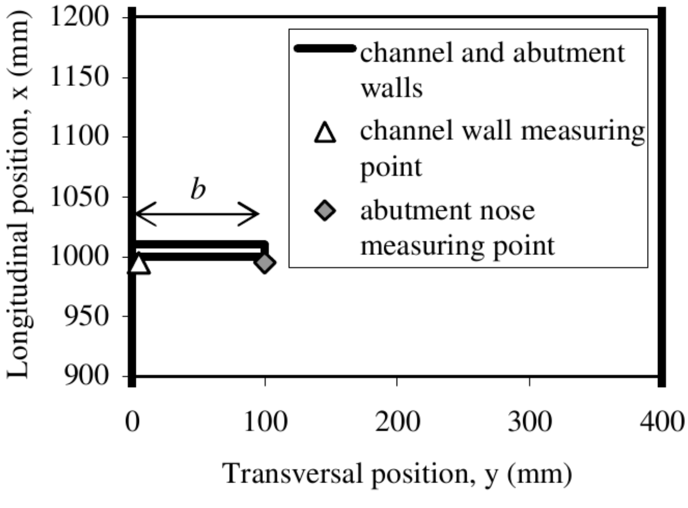

Figure 3.2: Definition sketch of the vertical wall (Radice et al., 2006)

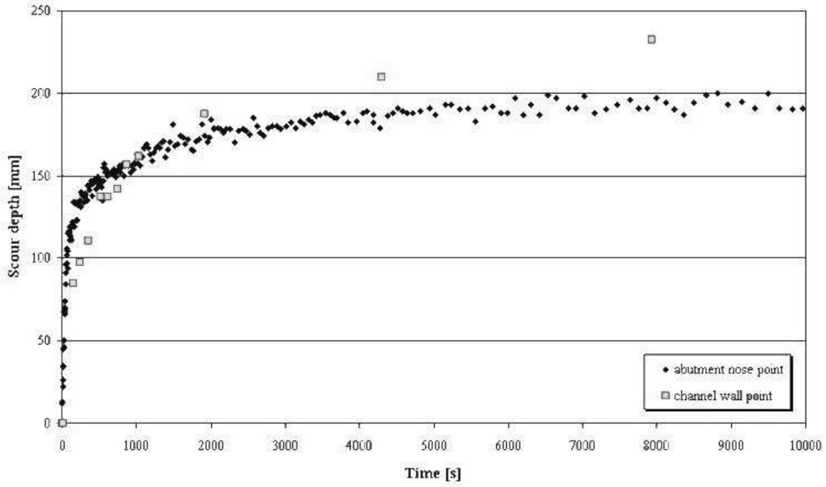

Figure 3.3: Temporal evolution of measured scour (Ballio et al., 2006)

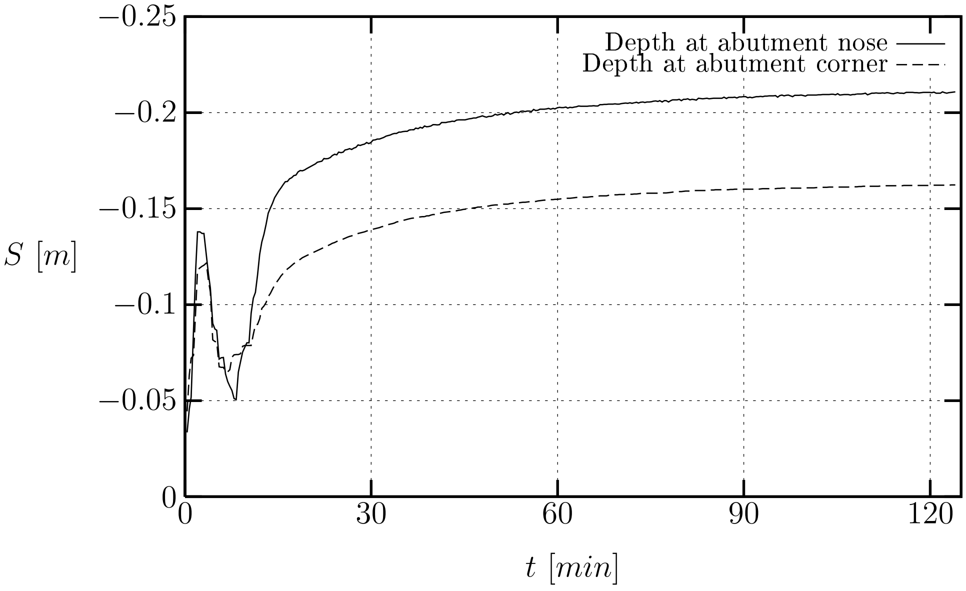

Figure 3.4: Temporal evolution of scour using the transport rate equation of Engelund and Fredsøe

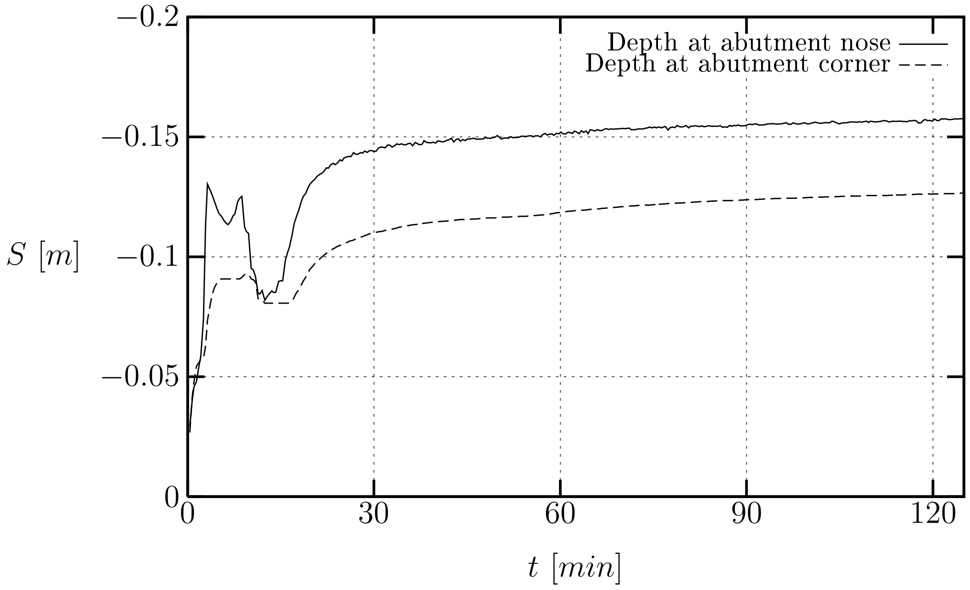

Figure 3.5: Temporal evolution of scour using the transport rate equation of Meyer-Peter and Müller

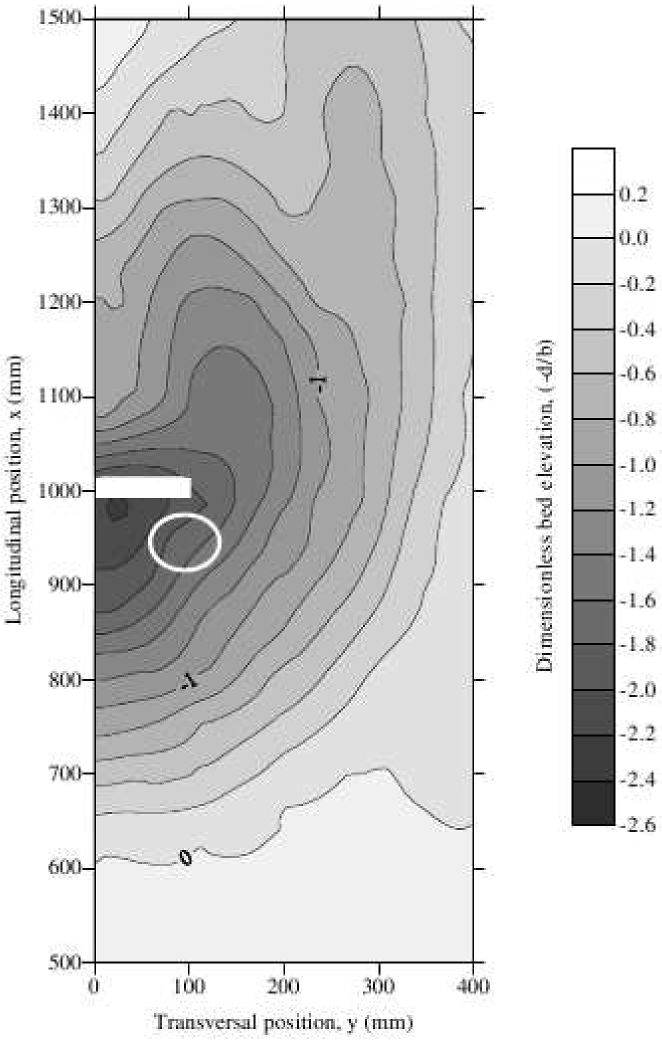

Figure 3.6: Scour after attaining the equilibrium depth (Radice et al., 2006)

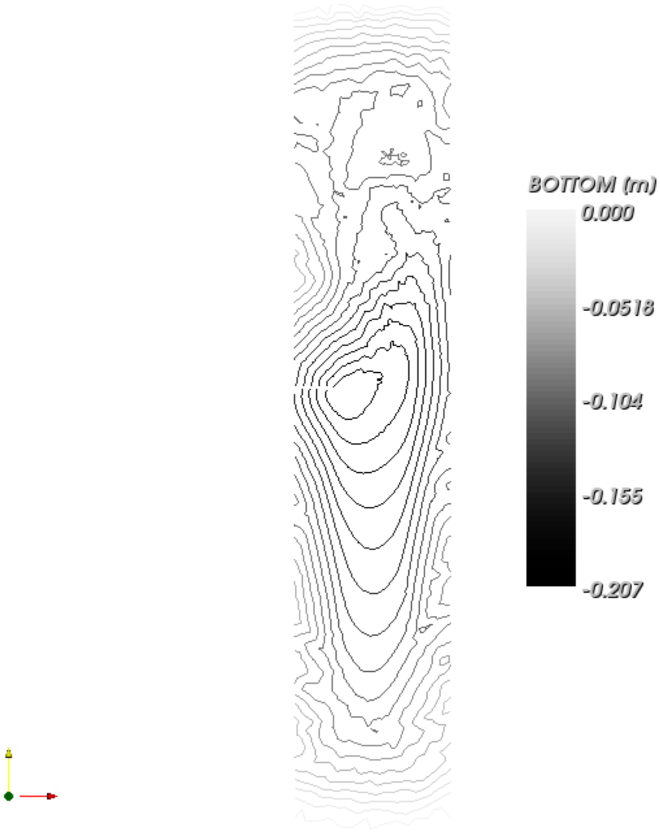

Figure 3.7: Scour isolines after 2h using the transport rate equation of Engelund and Fredsøe

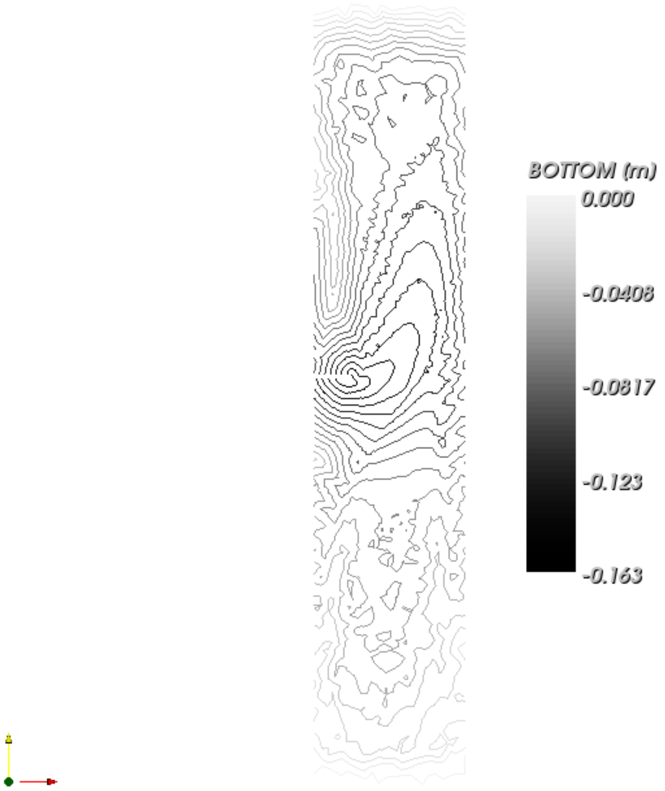

Figure 3.8: Scour isolines after 2h using the transport rate equation of Meyer-Peter and Müller

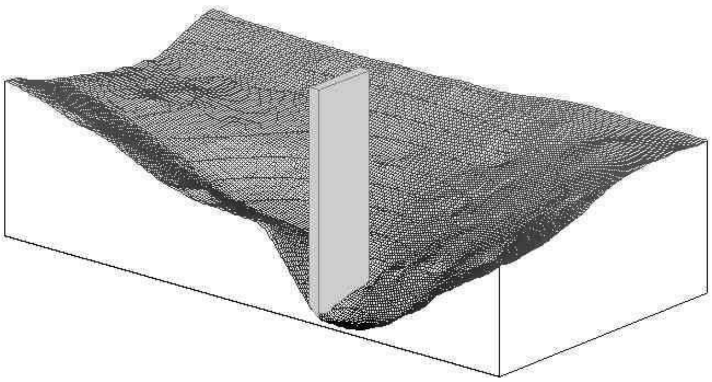

Figure 3.9: Scour hole after 2h45m (Ballio et al., 2006)

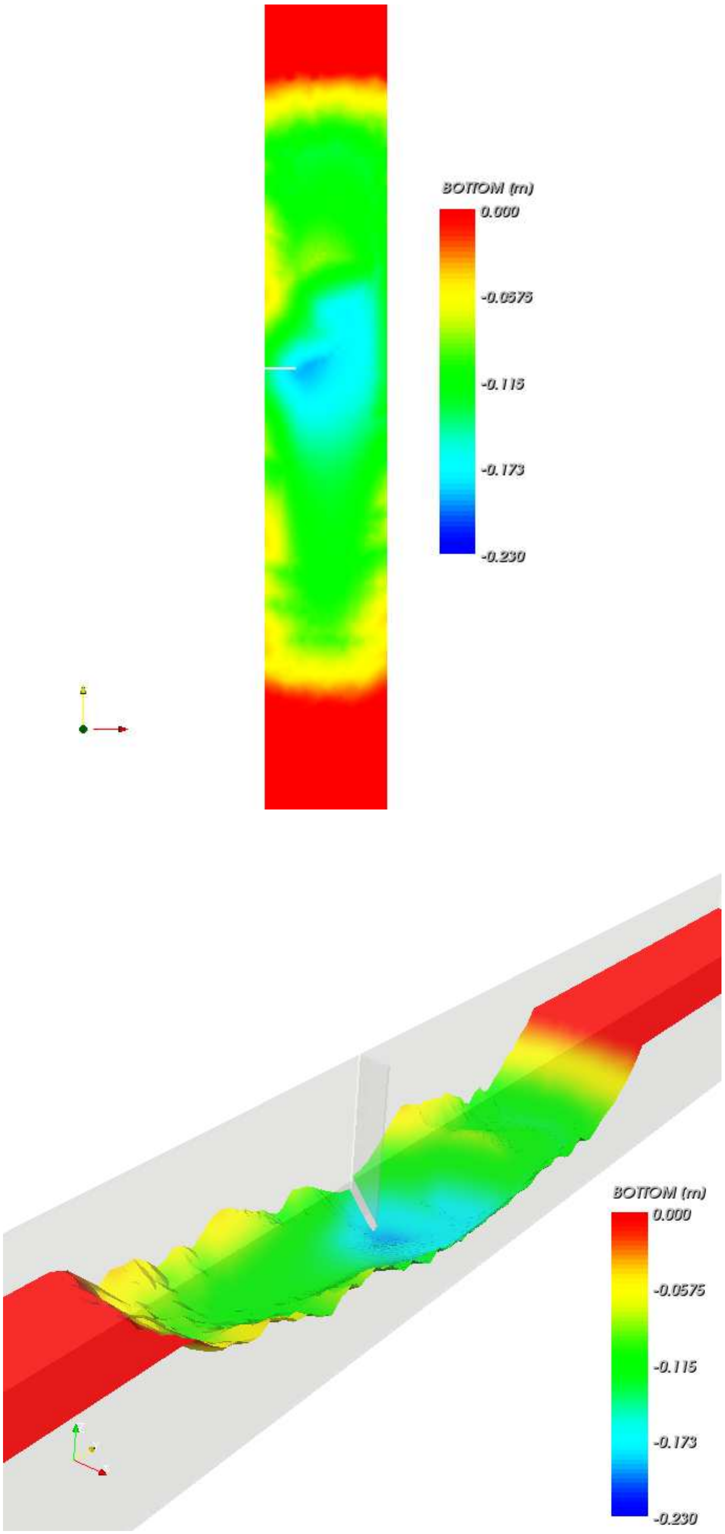

Figure 3.10: Resulting scour after 1800s using the transport rate equation of Engelund and Fredsøe

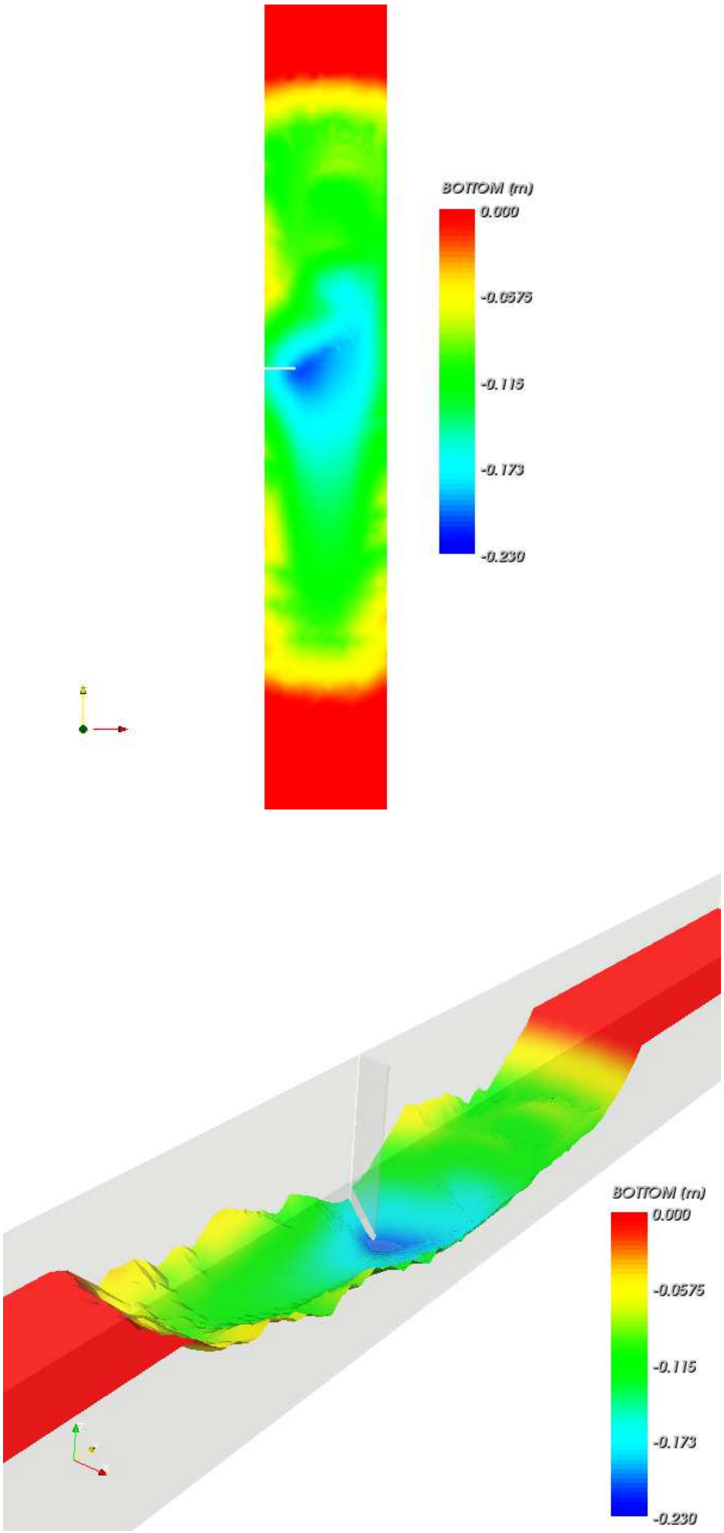

Figure 3.11: Resulting scour after 3600s using the transport rate equation of Engelund and Fredsøe

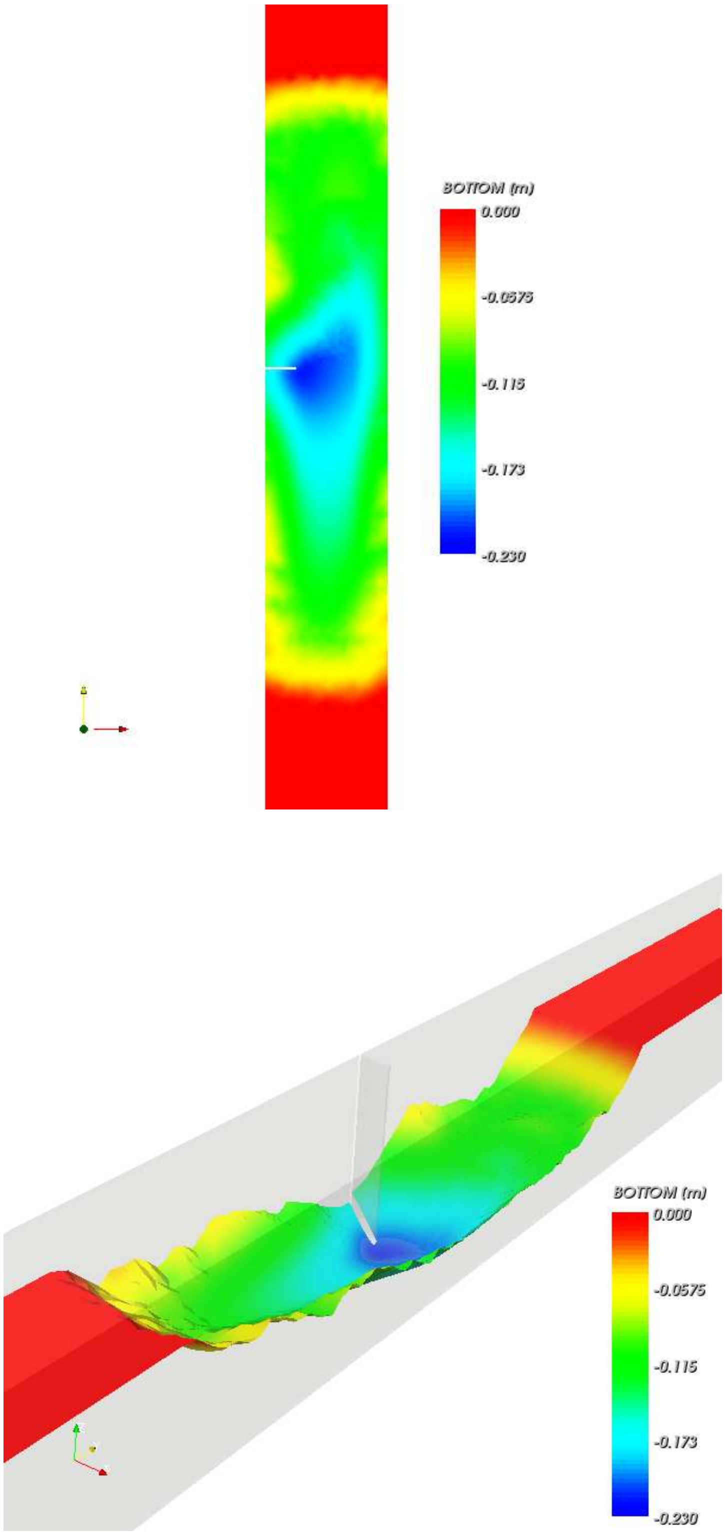

Figure 3.12: Resulting scour after 7200s using the transport rate equation of Engelund and Fredsøe

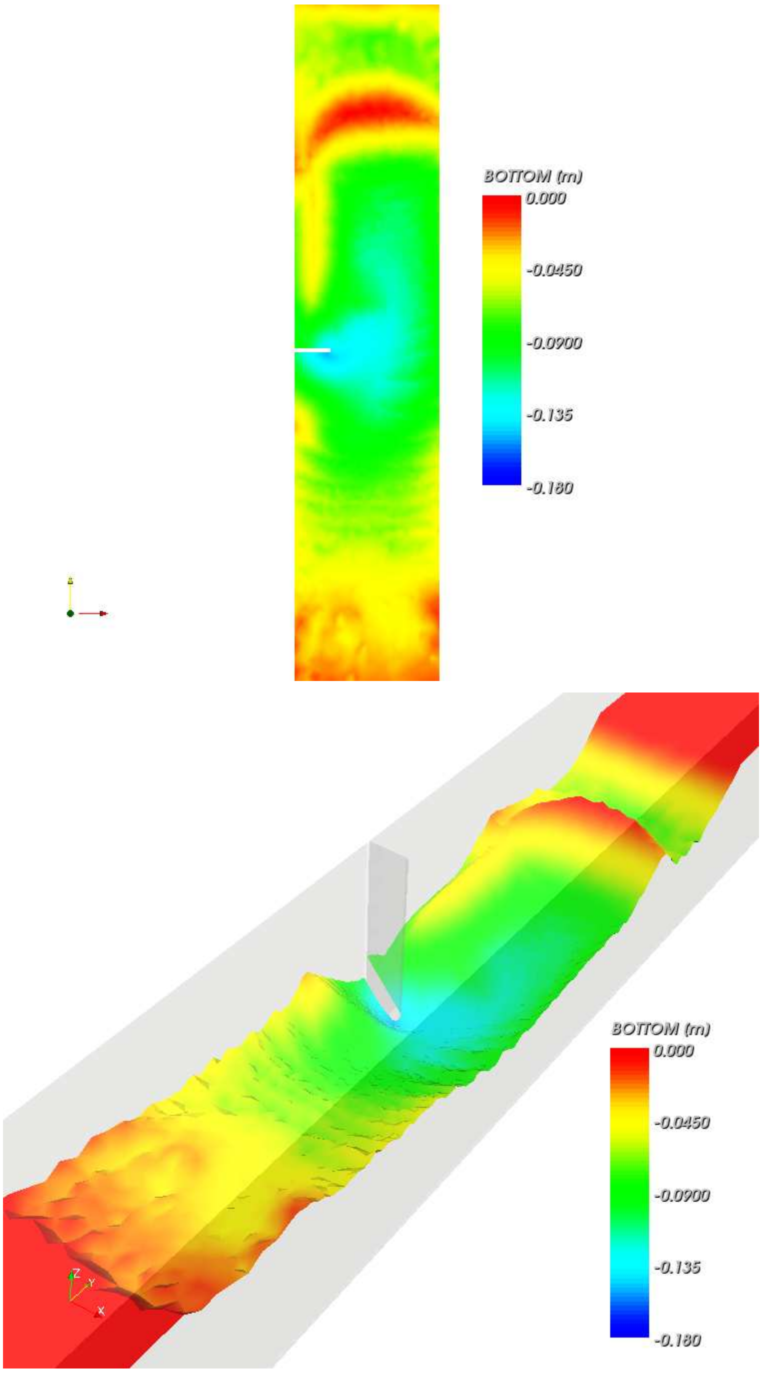

Figure 3.13: Resulting scour after 1800s using the transport rate equation of Meyer-Peter and Müller

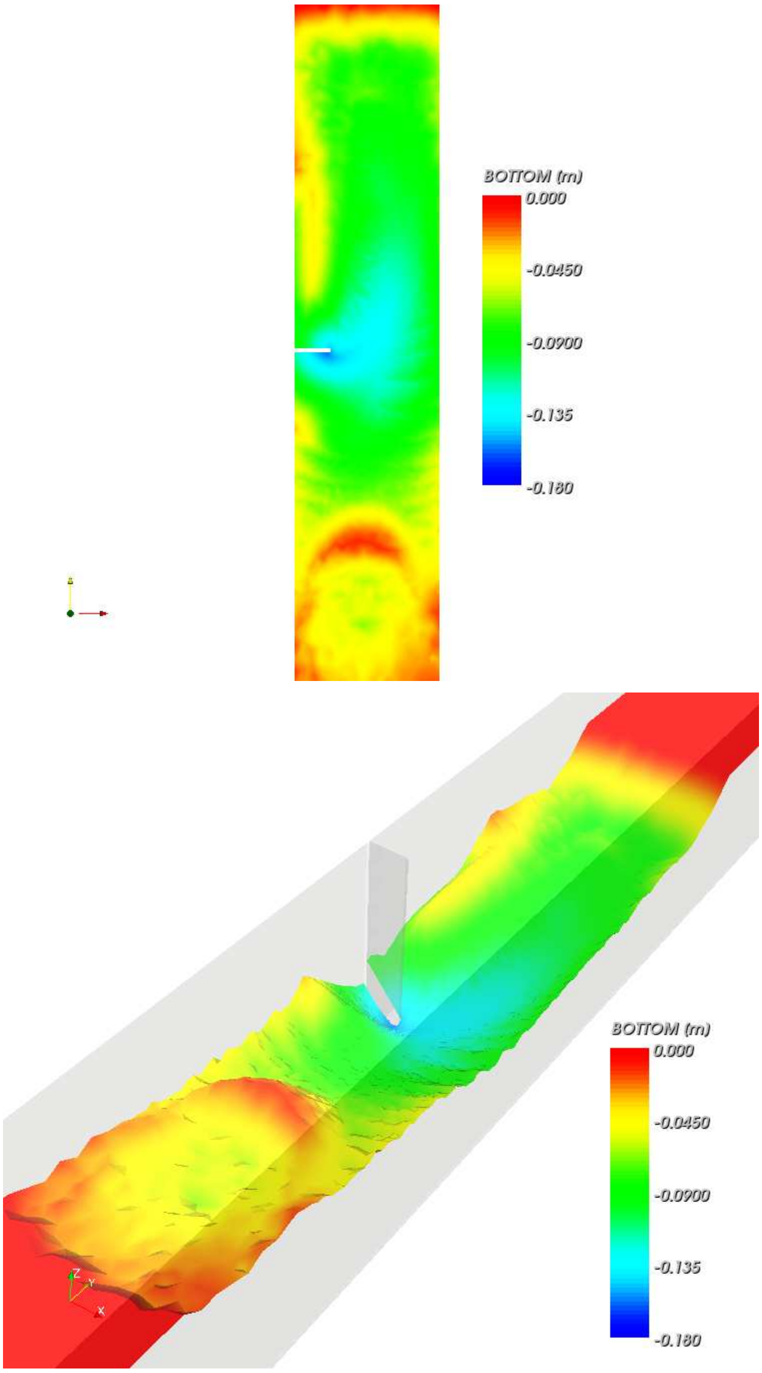

Figure 3.14: Resulting scour after 3600s using the transport rate equation of Meyer-Peter and Müller

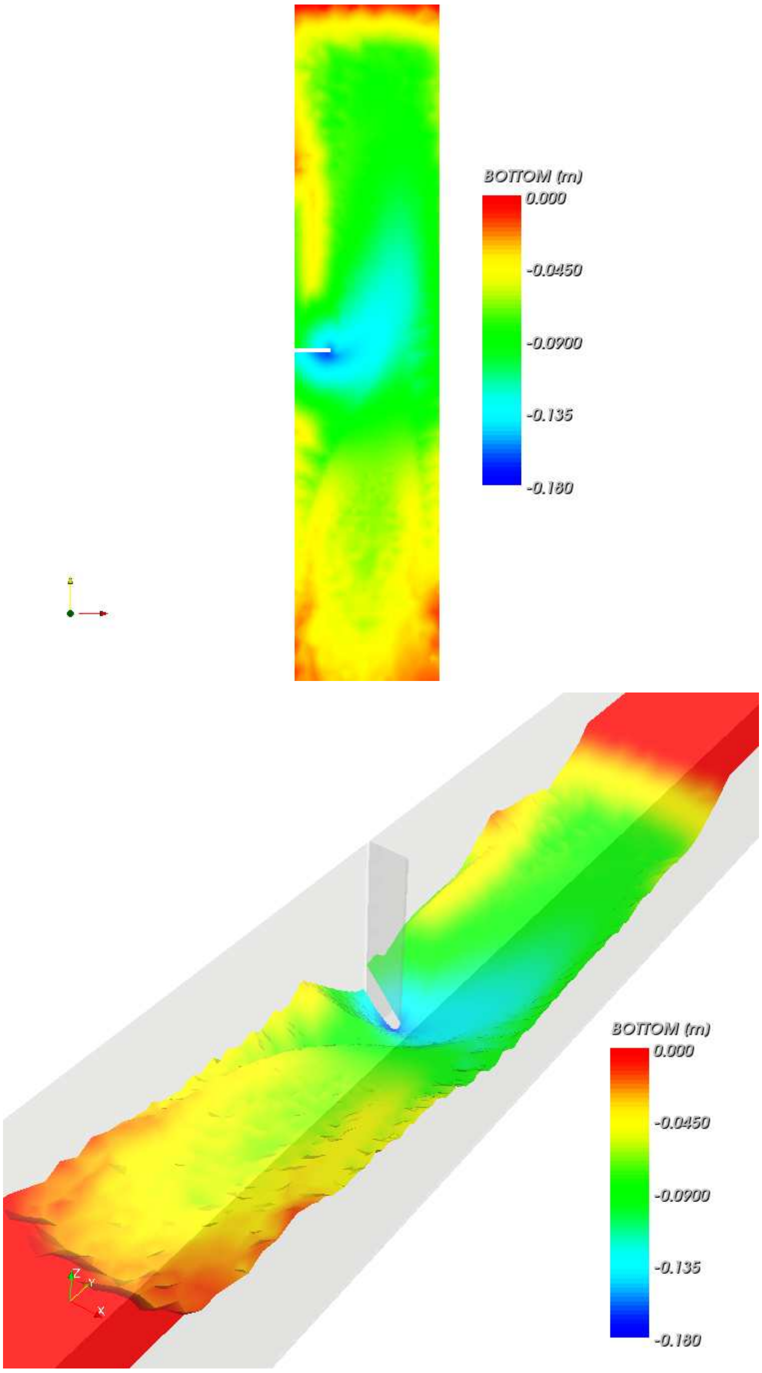

Figure 3.15: Resulting scour after 7200s using the transport rate equation of Meyer-Peter and Müller

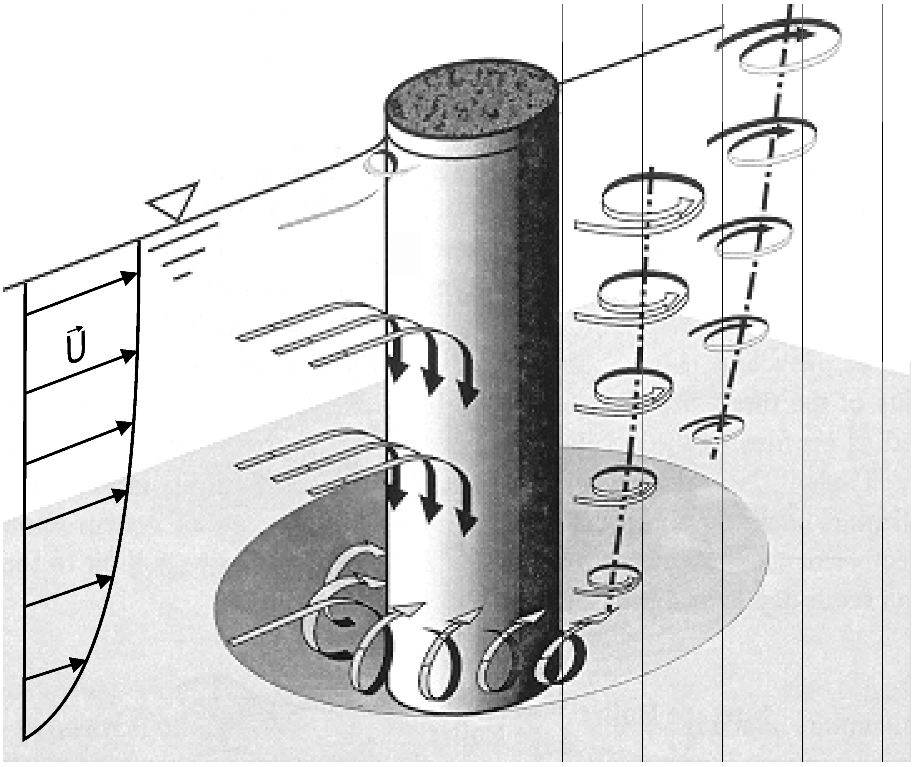

Figure 3.16: Flow pattern around a cylinder (Melville and Coleman, 2000)

3.1.2 Vertical cylinder

The flow around a circular cylinder (Fig. 3.16) features several effects that lead to an increased shear stress acting on the soil surrounding the structure. A boundary layer flow has a vertical pressure gradient which leads to a downward directed flow on approaching a vertical pile. This results in a horseshoe vortex, which is recognised as being one of the main mechanisms promoting scour. The flow is also contracted, which leads to an increased velocity on both sides of the cylinder. Vortex shedding tends to convey the sediment particles that have been eroded downstream away from the pile.

The flow around a pile may be described by dimensionless parameters. Whereas the Keulegan-Carpenter number (Eq. 3.3) describes the flow around a pile in an oscillatory flow, the Reynold's number describes the flow regime at a cylinder approached by a steady flow. This is defined by

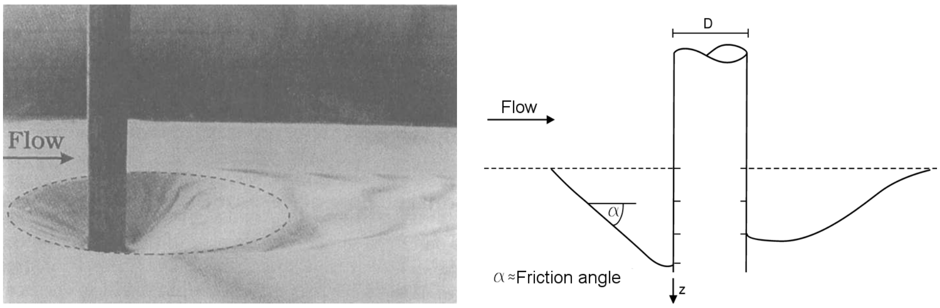

Figure 3.17: Flow-induced scour in a laboratory experiment (Eadie and Herbich, 1986)(left) and scheme of vertical cross-section (right)

$$Re = \frac{U_\infty\, D}{\nu} \tag{3.1}$$

A vortex system does not develop for a Reynold's number below five. With increasing Reynold's number (>40), vortex shedding occurs and a vortex street develops (Sumer and Fredsøe, 1997). The presented case of flow and scour around a cylinder has a pile Reynold's number of 46000. This means that the wakes are fully turbulent while the boundary layer is still laminar. The thickness of the boundary layer according to Schlichting (1982) may be approximated by

$$\frac{\delta}{D} = O\left(\frac{1}{\sqrt{Re}}\right) \tag{3.2}$$

where δ is the boundary layer thickness and D is again the diameter of the cylinder. The presence of a boundary layer causes deceleration of the flow close to the cylinder wall, and the resulting velocity gradients lead to vortices that occur for Reynold's numbers greater than five.

In the case of an erodible soil the above-mentioned flow effects lead to intense sediment transport close to the structure. A scour hole develops with slope angles approaching the angle of repose. At locations where the slope angle exceeds the angle of repose, sediment sliding occurs. This process continues until the slope returns to a stable condition. An example of such a scour hole is shown in Fig. 3.17. High slope angles are especially noticeable in the upstream part of the scour hole where the primary vortex is present.

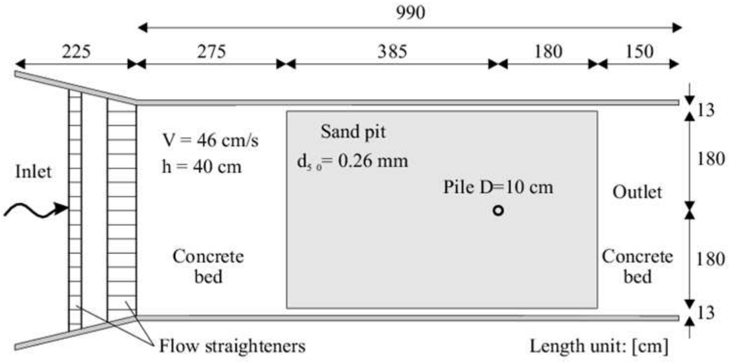

Figure 3.18: Experimental setup (Roulund et al., 2005)

The presented case of local scour around a vertical pile in a steady flow is based on the work of Weilbeer (2001), who compared the results of his numerical model with the measurements of Roulund (2000); Roulund et al. (2005). In contrast to the work of Weilbeer, a transport rate in direction transverse to the acting shear stress is also taken into account in the present study (see Chapter 2.2.5.1). The sediment transport rate equation of van Rijn was found to yield the best results in the case considered.

Figure 3.18 shows the experimental setup for the above-mentioned laboratory experiment. The flow channel was 9.90m long and 3.60m wide. The water depth was 40cm and the averaged velocity in the channel was given as 46cm/s. The 10cm diameter pile used in this experiment was placed in a sand pit containing sand with a particle diameter of 0.26mm. In the numerical experiment the mesh and numerical parameters for the flow were the same as used by Weilbeer. The results of the laboratory experiment are shown in Fig. 3.19. The scour hole is seen to have a round shape while the ripples are indicative of live-bed conditions.

The results of the flow simulations are comparable to the results of Weilbeer (2001). Although the turbulence model and numerical parameters are identical, a different advection method was adopted. In order to reduce the numerical diffusion SUPG (Streamline-Upwind Petrov/Galerkin) method was used in the present case. Fig. 3.20 shows the flow at a depth of 30cm. The horseshoe vortex at the pile and its effect on the near-bed velocities are clearly evident in Fig. 3.21.

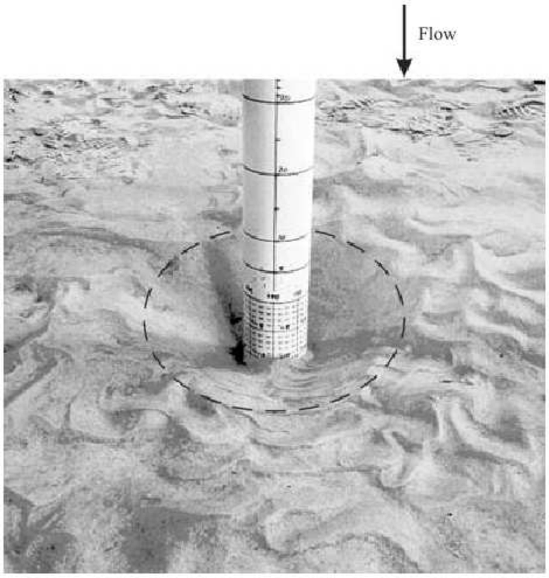

Figure 3.19: Flow-induced scour in the experiments of Roulund et al. (2005)

This leads to a flow which opposes the approaching flow upstream of the cylinder. As a consequence, high sediment transport takes place in this region. This is primarily directed away from the pile and leads to fast development of the scour hole. The amplification of the shear stress caused by flow contraction is shown in Fig. 3.22. In the present the amplified shear stress is about eight times the shear stress in the undisturbed flow.

As already discussed in Chapter 2.2.5, an existing scour hole has an influence on the direction of sediment transport. The change in direction in a scour hole is shown in Fig. 3.23. Due to the action of gravity, sediment transport is less radial and more tangential at the pile. The result of the simulation after two hours is a scour hole with a round shape (Fig. 3.24) resembling the shape observed in the presented laboratory experiment (Fig. 3.19). The scour depth is slightly overestimated by the model. The temporal evolution (Fig. 3.25) of the scour hole shows that the dynamics of the process are not exactly modelled especially during the initial phase and that the equilibrium depth is attained later than in the laboratory experiment.

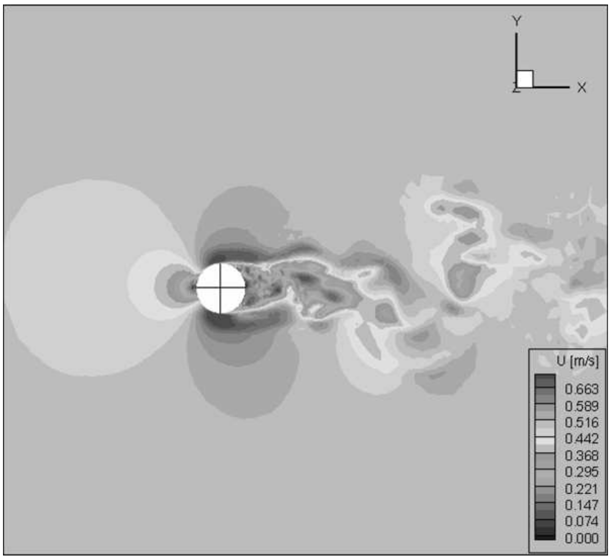

Figure 3.20: Flow around the cylinder at $d = 0.3m$

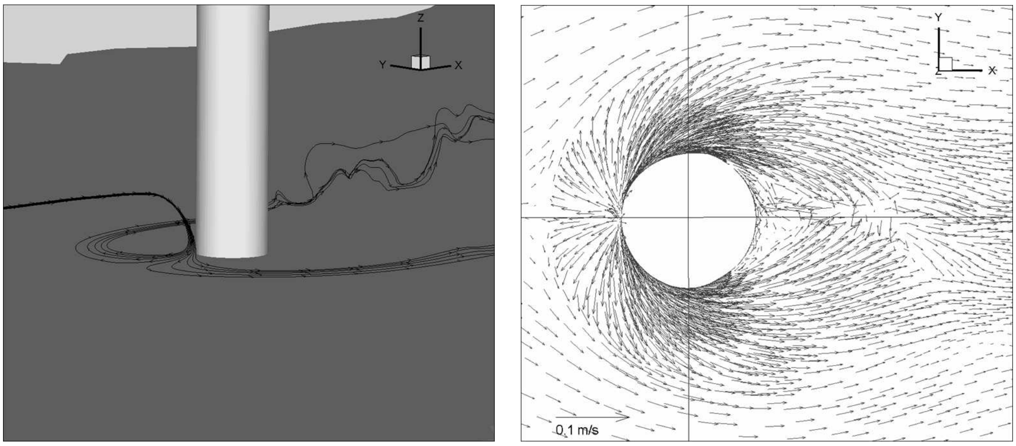

Figure 3.21: Horseshoe vortex (left) and shear velocities (right) in the numerical simulation

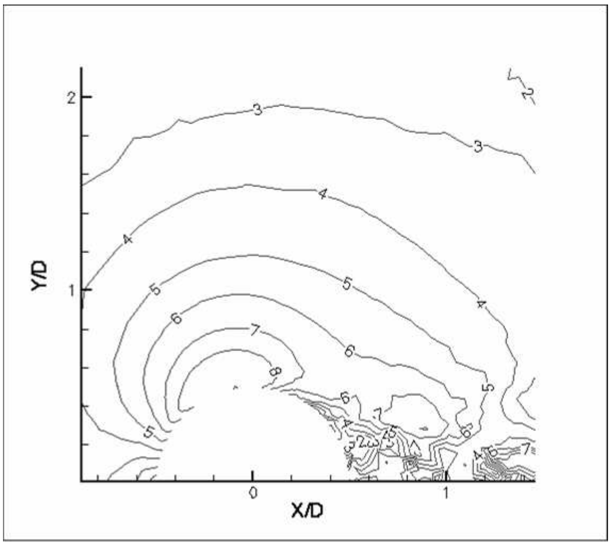

Figure 3.22: Shear stress amplification factor around the cylinder

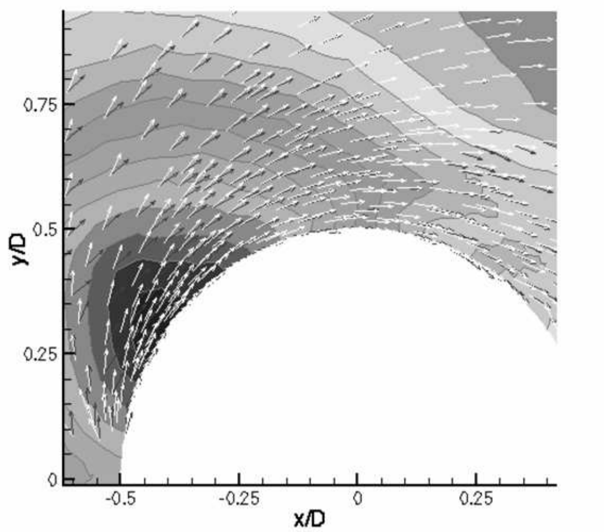

Figure 3.23: Influence of slope on the direction of sediment transport

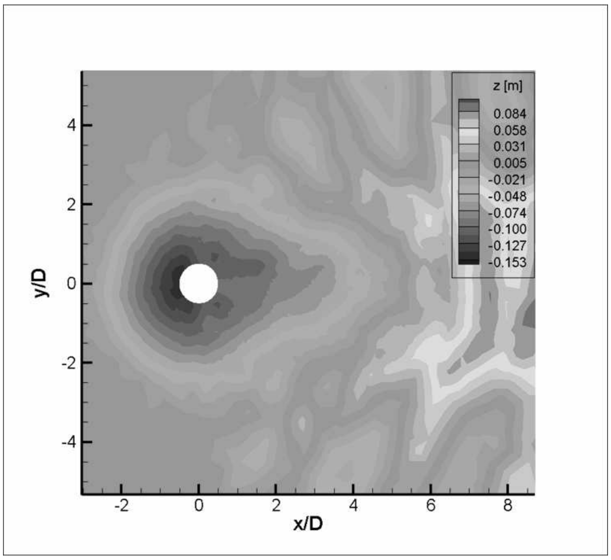

Figure 3.24: Simulated scour after two hours

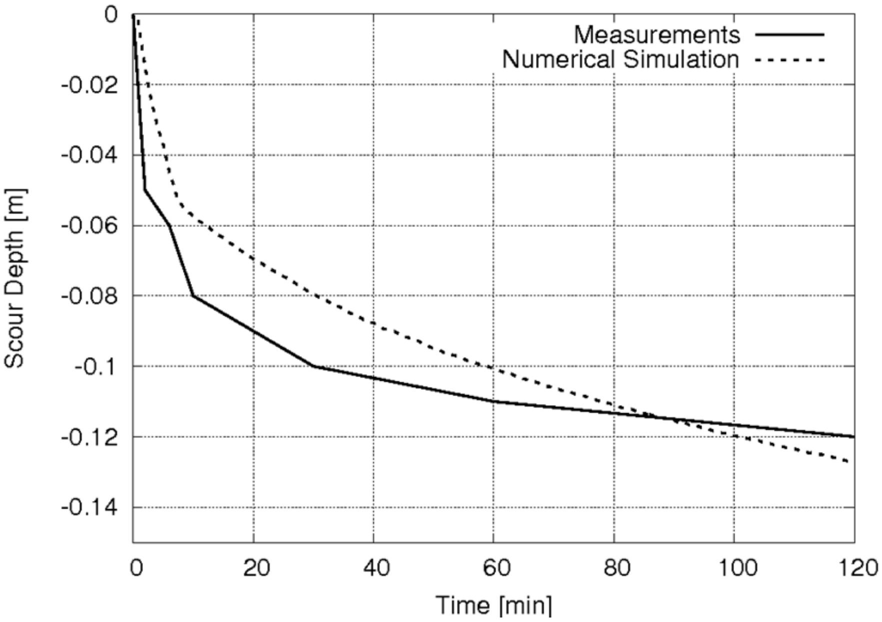

Figure 3.25: Temporal evolution of simulated scour

3.2 Wave-induced scour

The flow around a cylinder that is exposed to an oscillatory flow may be characterised by a dimensionless parameter, namely the Keulegan-Carpenter (KC) number (Eq. 3.3). In this equation U_m is the maximum near bed velocity, T_w is the period of the oscillatory flow and D is the diameter of the pile. The KC number describes the ratio of the motion of water particles to the diameter of the cylinder. Small KC numbers thus indicate that the motion of water particles is small compared to the diameter of the pile. Flow separation does not occur for very small KC numbers.

Large KC numbers on the other hand indicate a distinct motion of particles with flow separation and the possible occurence of vortex shedding. If the flow period is long enough, a vortex system similar to the steady flow case (see Chapter 3.1.2) developes at the pile for a maximum of half a flow period. The flow and vortex shedding regimes to be expected for different KC numbers may be found in Sumer and Fredsøe (1997).

$$KC = \frac{U_m T_w}{D} \tag{3.3}$$

3.2.1 Waves with KC numbers < 6

The first example of the numerical modelling of wave-induced scour is based on experiments by Sumer and Fredsøe (2001a) carried out in a 10.6m wide and 8m long wave flume (Fig. 3.26). A cylinder of 1m diameter was placed in a sand pit. The median diameter of the sediment grains was 0.2mm. Waves of different length and height were used in the experiments. The KC number was in the range of 0.08 to 0.61 for the scour experiments and 0.34 to 1.1 for the rigid bed experiments. The velocities from the numerical model were verified by a rigid bed experiment with a KC number = 1.1 (Fig. 3.27). The velocities were measured at a distance of 10cm from the cylinder surface. A scour simulation was carried out with a KC number of 0.61, which represents the highest available value of the KC number for which scour measurements were made. Because the sediment transport rates and hence the bottom evolution were very small, it was possible to repeatedly use

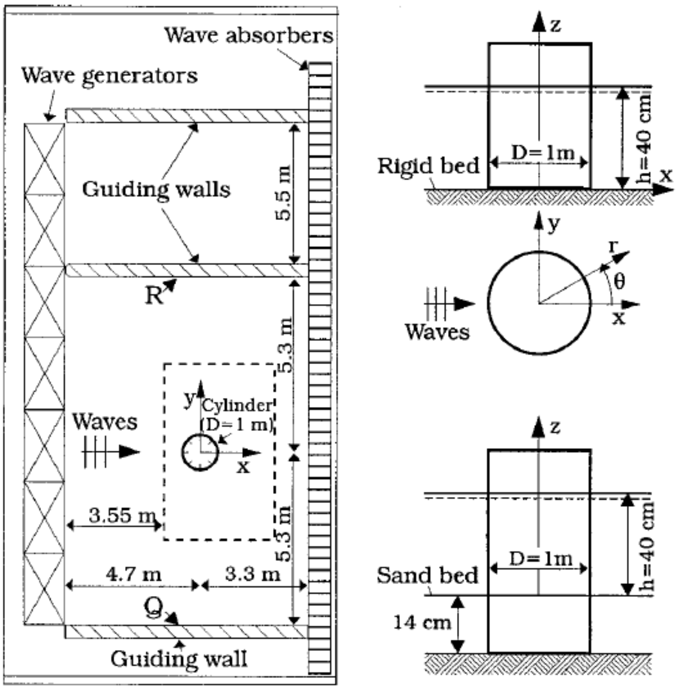

Figure 3.26: Wave channel for experiments with KC < 6 (Sumer and Fredsøe, 2001a)

the flow results of one wave over twenty minutes of sediment transport simulation. The overall simulation lasted ten hours.

The results of the numerical experiment for the verifying of the velocities are shown in Fig. 3.28. The magnitude of the tangential velocity as well as the phase are in good agreement with the measured results. Considering the radial velocity values, a small deviation is evident, especially during the first half of the wave period. This is apparently due to reflections in the simulated wave channel, which were mainly absorbed in the laboratory channel. As predicted, no horseshoe vortex was formed. The wave-induced flow is contracted along the sides of the cylinder, which leads to higher velocities in this region. The resulting sediment transport is still very small, however, owing to the overall low velocities and the absence of a horseshoe vortex. The sediment transport rate equation of Cheng was therefore used in this experiment, as Cheng's equation permits a calculation of transport rates even when only a very small shear stress is present at the

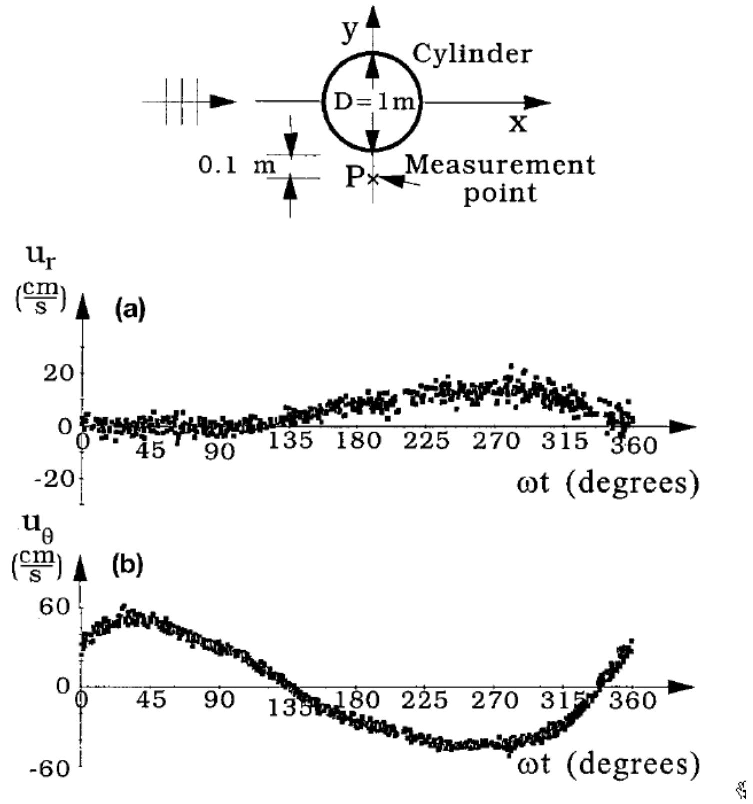

Figure 3.27: Measured velocities (Sumer and Fredsøe, 2001a)

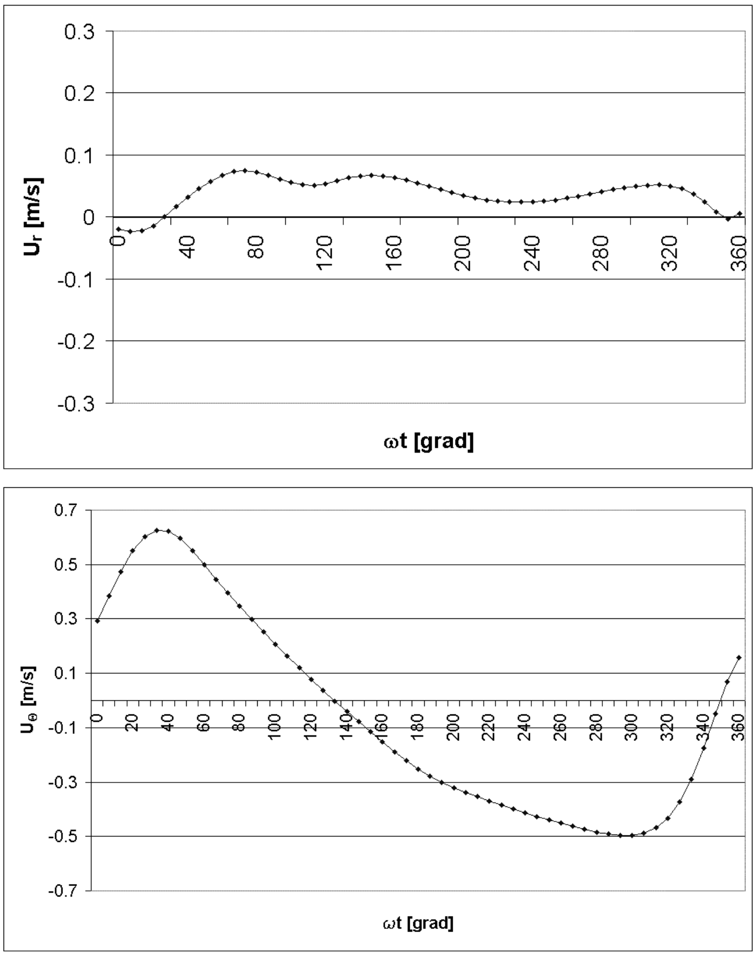

Figure 3.28: Simulated velocities

bed. Figure 3.30 shows the resulting scour profile after a simulation of ten hours. Although the scour depth closely agrees with the results from the laboratory experiment, the scour hole profile is slightly different. Although the scour hole is located downstream of the cylinder, it has a different radial extension. This is presumably due to the increasing coarseness of the spatial discretisation with increasing distance from the cylinder.

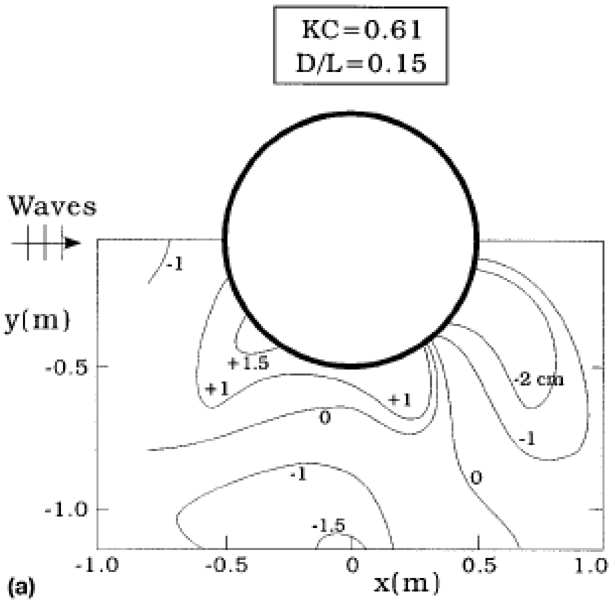

Figure 3.29: Measured scour profile (Sumer and Fredsøe, 2001a)

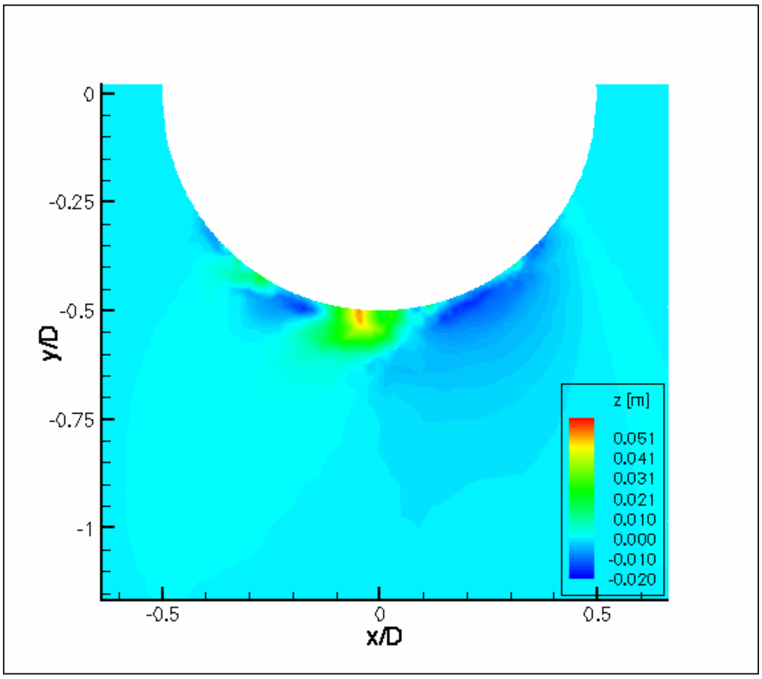

Figure 3.30: Simulated scour profile

3.2.2 Waves with KC numbers > 6

Assuming that the verification of the flow model for waves carried out in Chapter 3.2.1 is also valid for experiments with a much larger KC number, the following wave scour simulation based on the experiments of Sumer et al. (1992) was performed. In contrast to the previous experiments, a horseshoe vortex is expected over a certain time period during a half wave cycle for a KC number > 6.

The 10cm diameter pile used in this experiment was placed in 28m long and 4m wide wave flume. Waves with different KC numbers were used in the experiments. Wave scour for a KC number of 24 and a pile diameter of 10cm was simulated by the numerical model and the results were compared to the measurements of Sumer et al. (1992). The median diameter of the sediment grains was 0.18mm. The flow results for a single wave were repeatedly used to calculate sediment transport over a period of one minute. The flow over the scoured bed was subsequently recalculated.

Waves with a KC number > 6 produce a horseshoe vortex (Sumer and Fredsøe, 2002) around the structure similar to the vortex obtained for a steady current. This behaviour is correctly reproduced by the numerical model (Fig. 3.31). As shown by the results, the vortex is present for less than half of the wave period. Because sediment transport rates increase with the developing horseshoe vortex, the shape of the scour hole is more similar to that given by experiments with a steady current than the shape obtained for a small KC numbers (KC$<$6). The transport rate equation of van Rijn was applied in this experiment, whereby one wave was used for one minute of sediment transport.

Unfortunately, this experiment provides no information concerning the temporal evolution and shape of the scour hole. Only the final scour hole depth is known. The non-dimensional equilibrium scour depth (S/D) in the laboratory experiment was 0.31 for the given KC number of 24, whereas a scour depth of 0.32 was attained in the numerical simulation.

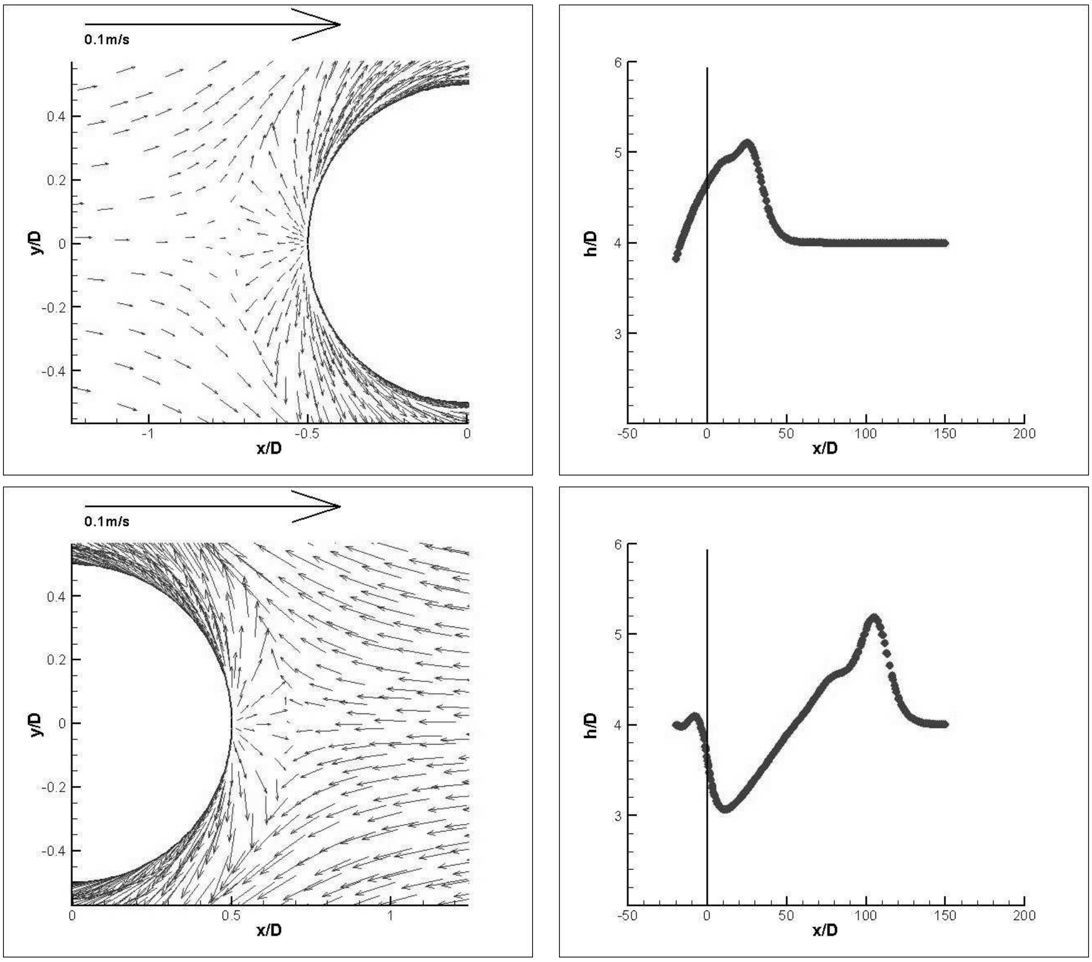

Figure 3.31: Resulting bottom velocities (left) and wave position (right)

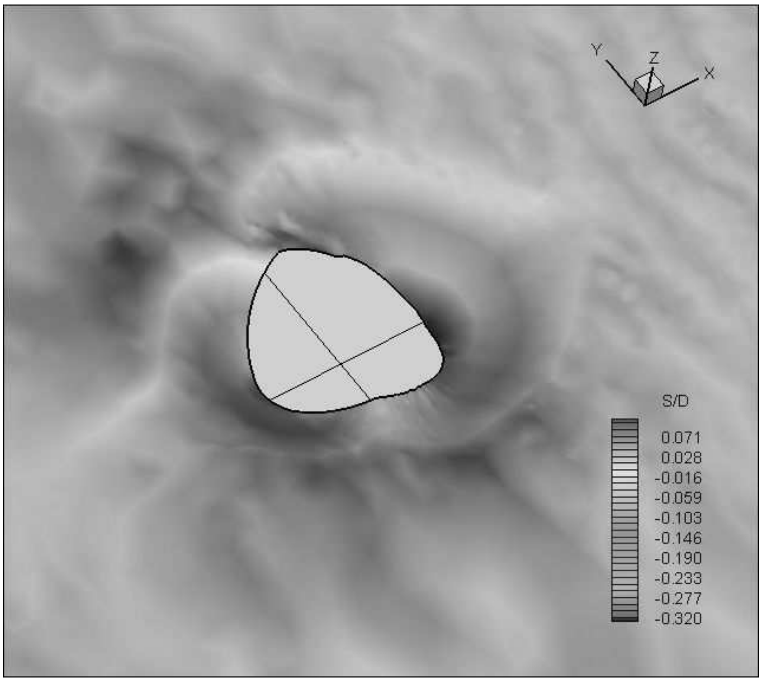

Figure 3.32: Resulting scour shape

3.2.3 Large Wave Channel experiments

In 2006 and 2007 large-scale wave scour experiments were carried out in the Large Wave Channel (GWK) of the Coastal Research Centre (FZK) in Hanover, Germany. This wave flume is 307m long, 7m deep and 5m wide. The diameter of the pile used in the investigation was 0.55m (see Figs. 3.33 and 3.34). Because the model scale is 1:10, scale effects regarding the wave-induced flow and fine sands are minimized (Grüne et al., 2006). The median diameter of the sediment grains used in the experiment was 0.33mm. Irregular waves were used in order to simulate scour development in a natural environment. The lengths and heights of the waves were determined from the Jonswap (Joint North Sea Wave Project) spectrum, which was derived from wave measurements in the North Sea in 1968 and 1969. The spectrum was represented by 500 waves generated by a wavemaker. By repeating this spectrum twelve times, a total number of 6000 waves were generated for test series 2 and 3. In test series 1 and 4 the total number of waves was 9000 and 6500, respectively. The tests were carried out using four different

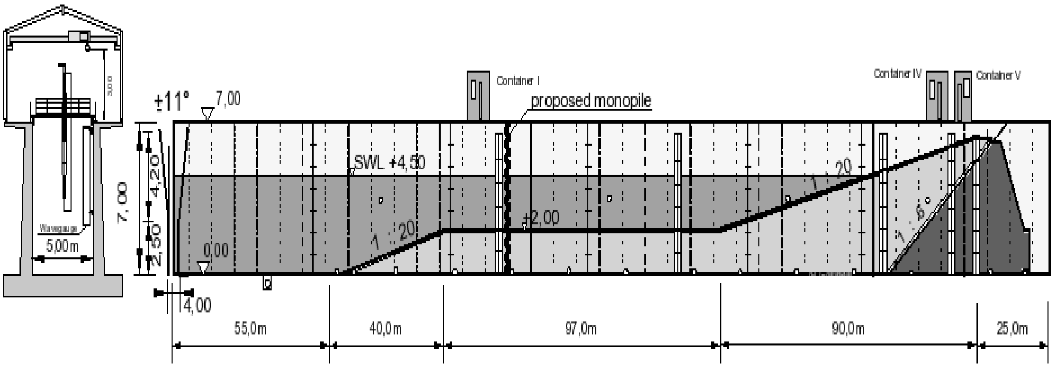

Figure 3.33: Large Wave Channel (Grüne et al., 2006)

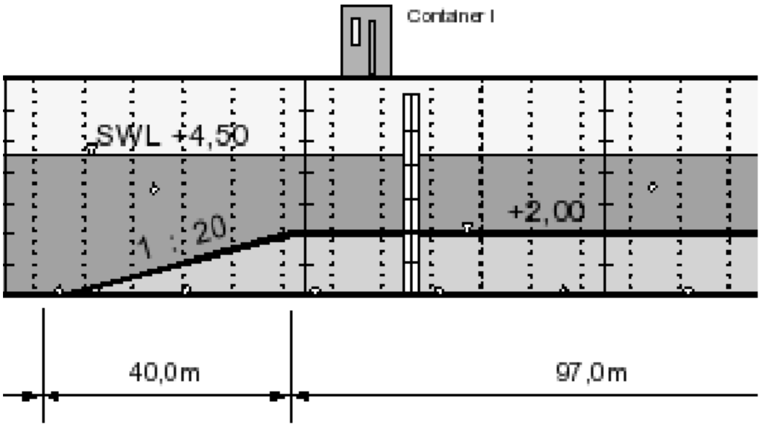

Figure 3.34: Large Wave Channel: position of pile

spectrum parameters (see Table 3.1).

Velocities and free surface levels were measured near the bottom in an undisturbed area close to the pile. In Table 3.1 d is the water depth, d_{sb} the bottom height, H_s the significant wave height and T_p the wave peak period. The results shown in Table 3.2 represent the measured data. These were calculated for a full spectrum (i.e. 500 waves) and afterwards averaged for the complete test series (i.e. 9000/6000/6500 waves). H_{max} is the maximum wave height, $H_{1/3}$ is the significant wave height (i.e. the average of 33% of the highest waves) and H_m is the mean value of all wave heights. Analogous to the wave heights v_{max} is the

No	$d[m]$	$d_{sb}[m]$	$H_s[m]$	$T_p[s]$
1	4.15	2.0	0.75	5.04
2	4.15	2.0	0.80	6.66
3	4.15	2.0	0.90	7.60
4	4.15	2.0	1.00	8.60

Table 3.1: GWK scour test parameters

maximum measured velocity, v_m is the mean velocity, $v_{1/3}$ is the average velocity of 33% of the highest velocities and T_p is the measured peak period.

No	$H_{max}[m]$	$H_{1/10}[m]$	$H_{1/3}[m]$	$H_m[m]$	$v_{max}[m/s]$	$v_{1/3}[m/s]$	$v_m[m/s]$	$T_m[s]$	$T_p[s]$
1	1.53	1.12	0.85	0.57	1.31	0.82	0.53	4.58	5.14
2	1.74	1.36	1.03	0.64	1.85	1.04	0.67	5.61	6.59
3	1.7	1.48	1.21	0.77	1.89	1.21	0.75	6.47	7.68
4	2.2	1.76	1.4	0.9	2.4	1.44	0.9	7.63	8.94

Table 3.2: Results of the GWK scour tests

Figs. 3.35 to 3.40 show the results of test series 3 after 3000 waves. The scour hole attains a depth of approximately 26cm and the deepest part is located downstream of the pile. The scour depth after 6000 waves was 25cm. The deepest scour was measured in test series 4, whereby the equilibrium scour depth attained 34cm after 6500 waves (Oumeraci et al., 2007). In test series 2 and 3 the equilibrium scour depth was already attained after approximately 3000 waves.

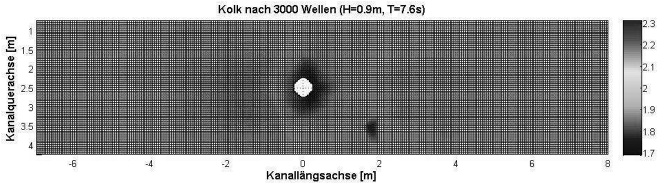

Figure 3.35: Test series 3: scour after 3000 waves (plan view)

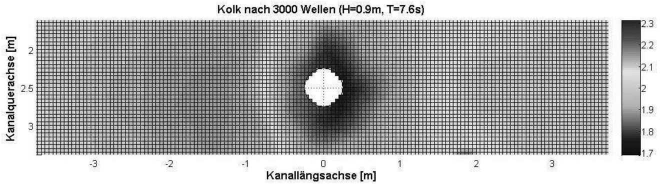

Figure 3.36: Test series 3: scour after 3000 waves (zoom)

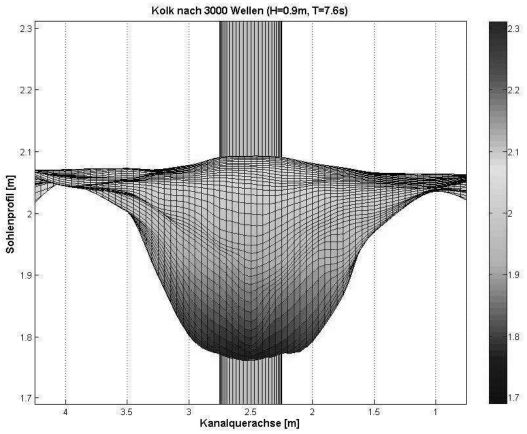

Figure 3.37: Test series 3: scour after 3000 waves (downstream)

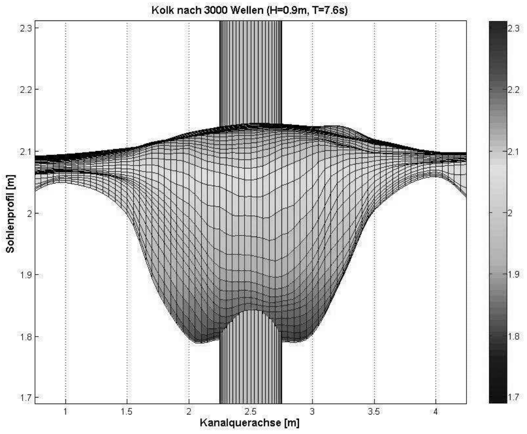

Figure 3.38: Test series 3: scour after 3000 waves (upstream)

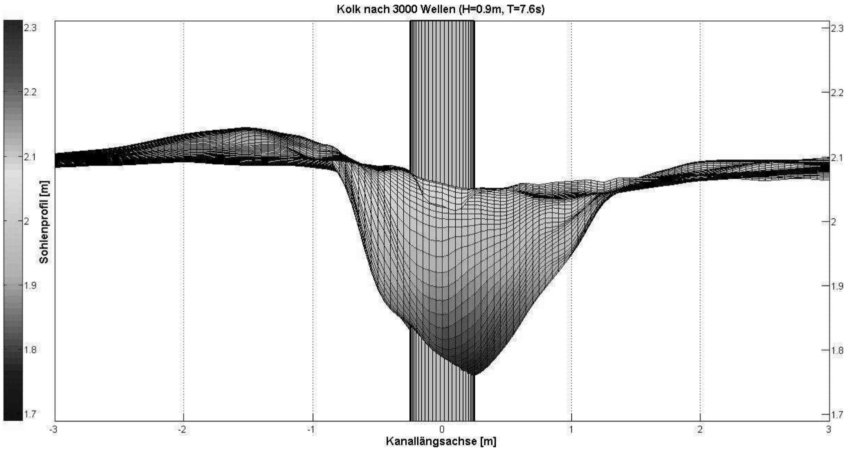

Figure 3.39: Test series 3: scour after 3000 waves (side view)

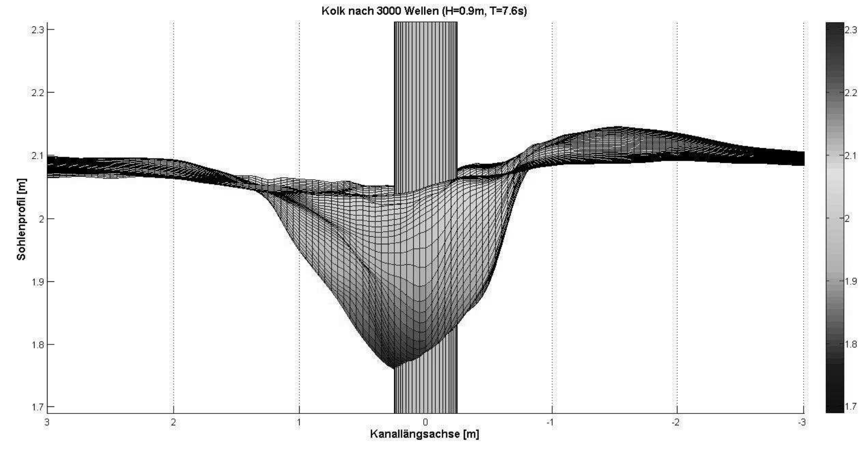

Figure 3.40: Test series 3: scour after 3000 waves (side view)

Only a part of the full channel length was used in the numerical model in order to reduce computation time. The wave inlet was positioned 10m in front of the pile and the boundary conditions for the numerical model were as followed: the three-dimensional velocity field and water depth were prescribed, whereas the dynamic pressure was unconstrained at the wave inlet. According to Sumer et al. (1999) the wave parameters for a regular wave which are representative for a wave spectrum may be approximated by $H = H_s/\sqrt{2}$ and $T = T_z$, where T_z is the zero upcrossing period and H_s is the significant wave height. Tests showed that in the considered case this approximation leads to an underestimation of the scour depth. The wave height $H_{1/3}$ and the peak period T_p were therefore used for defining a representative wave. The flow results for one wave were used for two hundred waves of sediment transport simulation. The total number of couplings between flow and sediment transport was hence thirty. The sediment transport rate was calculated using the equation of Engelund and Fredsøe.

The results of the numerical experiments for test series three are shown in Figs. 3.41-3.44. The first tests were carried out with the sediment ramp included in the numerical model. The results show that the waves become steeper and shorter when passing the ramp. As this shape is not stable, the waves return to their original shape once the ramp has been passed. Although this effect is not totally through at the pile, it is included in the measurements of T_p. The results of the numerical simulations show that the difference in shear stress is small when the ramp is included in the numerical simulation. In view of this, the ramp was neglected in the scour calculations.

The results of the scour simulation are shown in Figs. 3.43 and 3.44. The shape of the scour hole differs significantly from the shape obtained in the flume experiments. This could be due to the fact that a regular wave was used instead of a wave spectrum. The deepest point of the scour hole is located along the side of the pile rather than downstream. This is where the highest shear stresses occur in the numerical model. The temporal evolution progresses very rapidly for the first three hundred waves and then slows down. This may be caused to some extent by the arrival of sediment from upstream of the pile. This may also be the reason for the decreasing scour rate in the temporal range of five hundred waves. The coupling period might also have an influence on this model behaviour. The

Figure 3.41: Simulated wave series

scour depth after 3000 waves is underestimated, presumably because the wave parameters are derived from spectrum parameters and the resulting wave is not intense enough to produce the a representative sediment transport obtained in the flume experiments.

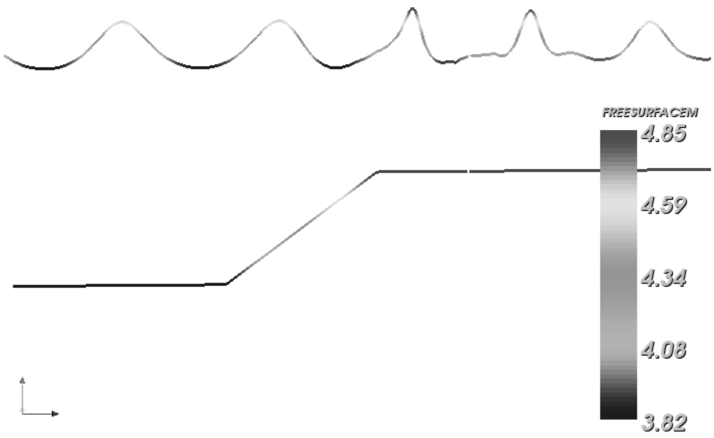

Figure 3.42: Simulated wave series (side view)

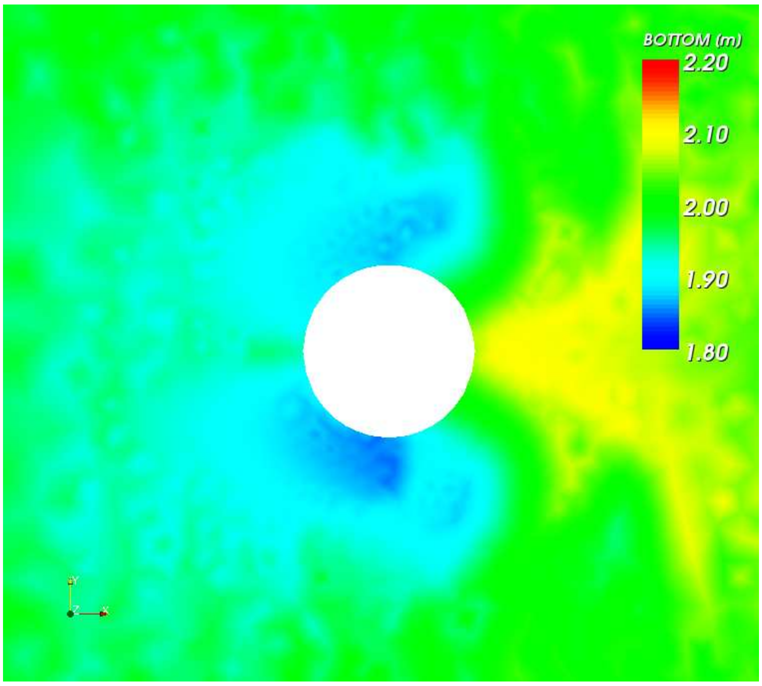

Figure 3.43: Simulated scour after 3000 waves

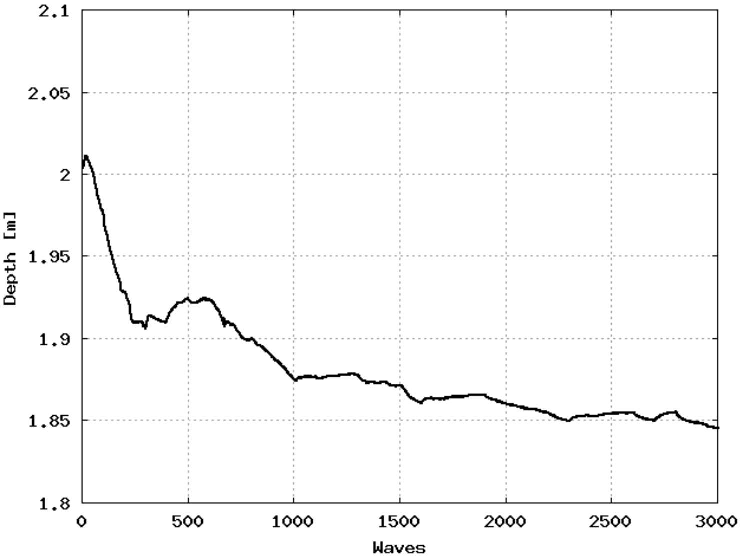

Figure 3.44: Temporal evolution of scour in the numerical simulation

3.3 Stability analysis of a scour hole

Modelling the bottom by means of a finite element model provides an opportunity to examine the response of the model to changing geometry as well as to the shear stresses affecting the surface layer. The developing scour leads to steep slopes which become unstable when the angle of repose is reached. This behaviour may be simulated with the aid of the finite element model, thereby permitting an analysis of the location and depth of instabilities. The bottom surface geometry exists as a mesh of triangles. In order to obtain a three-dimensional mesh, a horizontal layer of triangles with the same element coordinates as the surface layer is created. This layer is located beneath the lowest surface mesh point at about 20% of the height of the latter. The space between the two layers is filled with a constant number of wedge elements in the vertical direction. The finite element model of the soil has different degrees of freedom at the boundaries. Whereas no displacements are permitted over the bottom layer, the surrounding boundary faces cylinder nodes are allowed to move in the vertical direction. Simulations with the finite element model of the soil were carried out in order to analyse slope stability.

3.3.1 Flow-induced instability

The parameters used in the simulations were Young's modulus $E = 1 \cdot 10^5 kN/m^2$ and Poisson's ratio $\nu = 0.3$. The unit weight of the material was given as $\gamma = 13kN/m^3$. As, according to Krantz (1991); Schellart (2000), a small amount of cohesion is present even for granular materials, a cohesion factor of $c = 0.5kN/m^2$ was assumed. The depth of the scour hole after one hour of sediment transport was found to be 12.5cm. The finite element simulations were carried out from this point in time. The plastic strains p_{xz} are shown in Fig. 3.45. As a result of experiments by Roulund et al. (2005), sand slides were found to occur when the slope angle was two degrees greater than the friction angle. Figure 3.46 shows that for a difference of two degrees between the slope and the friction angle, strong plastic strains occur on the upstream as well as on the downstream slope when the actual slope angle exceeds the friction angle. As the solution algorithm does not converge under these conditions, this is expected to be the regions where most

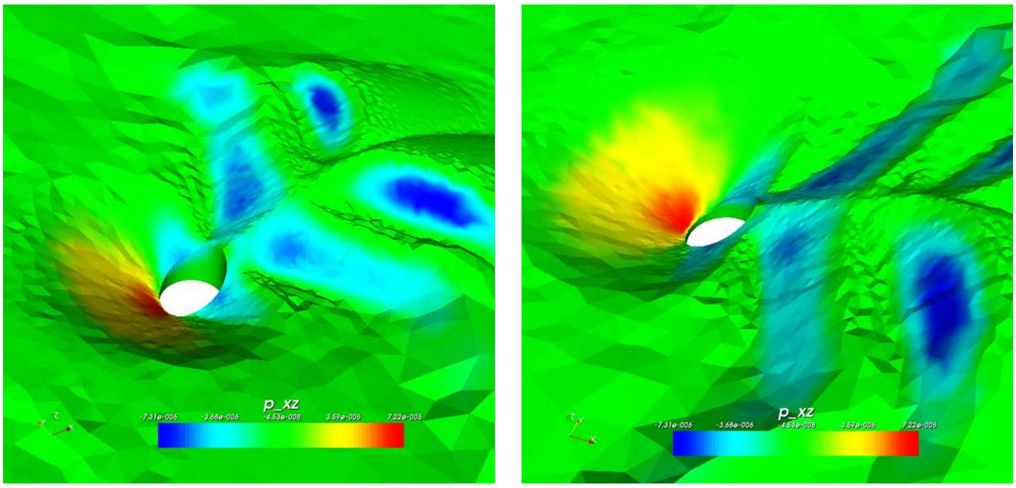

Figure 3.45: Plastic deformations for $\beta = \phi$

of the sand sliding takes place. As illustrated by Fig. 3.47, the intensity of the deformations is considerably less if the friction angle is two degrees lower than the actual slope angle. In this case the model converges and regains a stable condition even though plastic deformations occur.

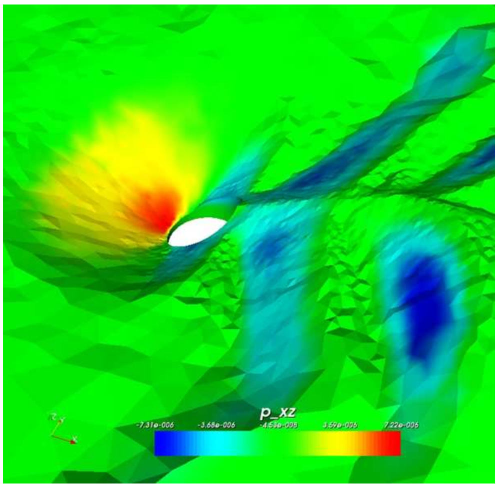

Figure 3.46: Plastic deformations for $\beta = \phi + 2°$

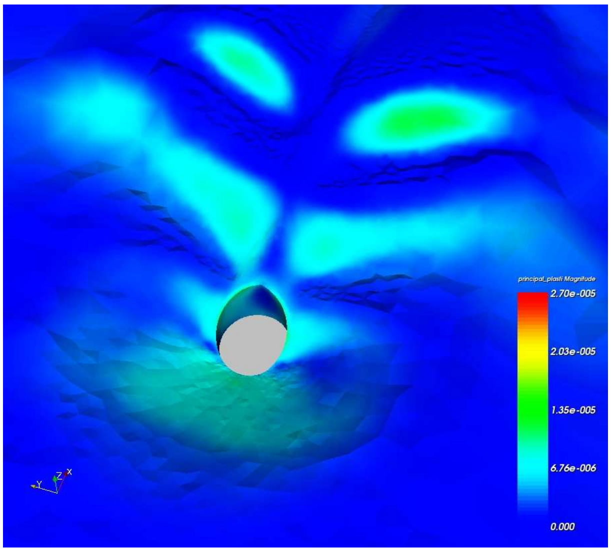

Figure 3.47: Plastic deformations for $\beta = \phi - 2°$

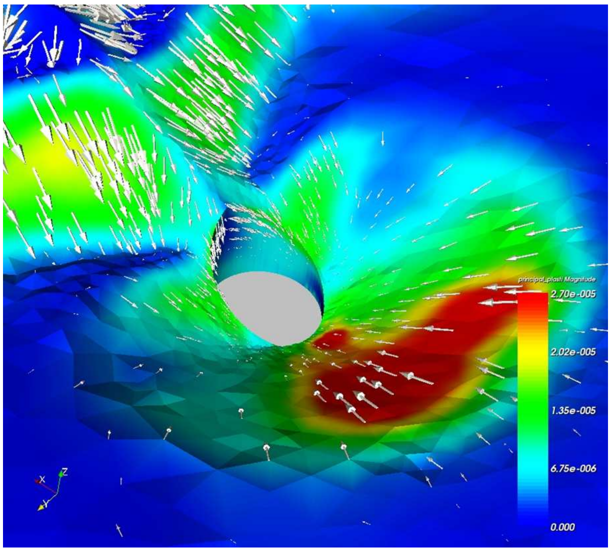

Figure 3.48: Displacement vectors

4 Conclusions

A three-dimensional flow model capable of simulating flows with and without a free surface was coupled with a model of sediment transport, bottom evolution and soil stability analysis. The flow model presented is capable of simulating a steady flow or a propagating wave for the purpose of calculating the flow field in the vicinity of a structure. The solver is based on the Reynold's averaged Navier-Stokes equations whereas closure of the set of equations is achieved by means of the k-ω turbulence model. The model was validated using experimental data for steady flows and for a propagating wave passing a vertical cylinder. In the case of a propagating wave the boundary conditions were calculated by first order wave theory or by stream function theory. The latter implements a numerical scheme for calculating wave properties such as the free surface and orbital velocities for any required order. By this means it is possible to prescribe highly nonlinear waves at the open model boundary.

The free surface scheme was found to be highly applicable to steady flows and propagating waves. The results obtained for the free surface, however, depend very much on the quality of the velocity field. Depending on the advection scheme used, small instabilities in the velocity field result in discontinuities at the free surface. The use of the method of characteristics as an advection scheme yielded results which led to a stable calculation of the free surface without anomalies. The fact that the vortex system at the cylinder was also sufficiently resolved meant that the calculated shear stress at the bottom was suitable for application in the sediment transport model.

Using the shear stress at the bottom computed by the flow model, a sediment transport rate may be calculated and subsequently inserted in the bottom evolution equation. The quality of the results of this model is highly dependent on the equations used for calculating the sediment transport rate. This is especially the case when simulating scour, as this is an extreme case with regard to shear stress and hence bottom evolution. Good results were obtained using the sediment transport rate equation of Cheng for the case of small shear stresses caused by short waves. In the case of high shear stresses the equation of Engelund and Fredsøe was found to be more suitable.

The simulation of sliding sediment is necessary in order to realistically model the bottom geometry. Adjustments for the inception of motion and the sediment transport rate at slopes improve the original equations in such a way that sand sliding is less intensive with regard to the number of iterations required, even though it is still necessary. The resulting scour geometry is therefore also characterized by this algorithm, which depends on one soil parameter.

The coupling of flow and sediment transport was carried out by using a representative period of flow results for several sediment transport computations. The period and number of re-used flow results were determined manually in order to control the number of required couplings. The former were chosen so as to minimise the bottom evolution during each coupling period prior to the next flow calculation. Computation time, on the other hand, was a limiting factor regarding the number of realisable couplings.

The sediment transport model was enhanced by a finite element model in order to analyse bottom stability. The horizontal mesh was extended in the vertical direction to form a three-dimensional mesh consisting of wedge elements. A linear-elastic solver was combined with a failure criterion and a visco-plastic method in order to calculate non-linear deformations. Several soil parameters as well as the bottom geomtetry are taken into account in this model in order to determine soil stability. By this means it is possible to locate zones of total failure more precisely than would otherwise be possible basd on a comparison between the actual slope angle and the friction angle.

The described model was used to simulate different laboratory experiments on flow and wave-induced scour. Simulations were carried out for a vertical cylinder and an abutment in a steady flow, whereby the results of experiments on short and long waves were used to validate the model. Furthermore, the scour resulting from a wave spectrum was used as a test case for the numerical model.

Simulations involving short waves indicate that no horseshoe vortex is formed at a vertical pile for a Keulegan-Carpenter (KC) number of less than six. Sediment transport in the proximity of the structure in this case is solely dependent on wave-induced near-bed velocities. This leads to comparatively small transport rates. In this case the best results were obtained using a transport rate equation that was not developed on the assumption of a critical shear stress for the inception of particle motion. The applied transport model permits the calculation of small transport rates even when the shear stress is very small. The results show good agreement with measurements with regard to both scour depth and shape.

When a long wave with a KC number greater than six passes a pile, the wave-induced flow is intense enough to produce a horseshoe vortex system. This leads to a situation which is comparable to steady flow conditions present for less than the length of the trough or crest. As sediment transport is dominated by this flow effect, the scour shape is more similar to the scour shape produced by a steady flow than by a wave with a KC number less than six.

The flow-induced scour simulations indicate that the sediment transport rate equation has a significant influence on the results. This is very obvious from the results of the abutment scour. Using the equation of Meyer-Peter and Müller led to good agreement with measurements regarding the final scour shape, whereas the equation of Engelund and Fredsøe resulted in an equilibrium scour depth similar to that observed in laboratory experiments. Although the scour depth was slightly overestimated for the case of a cylinder in a steady flow, the computed shape of the scour hole matched the measurements fairly well.

The bottom geometry of a flow-induced scour hole was used for analysing soil stability. The zones of erosion are then indicated by regions where strong plastic deformations occur. In the case of total failure the solution algorithm fails to converge as no stable condition can be found. Comparing the calculated erosion zones with the criterion of the sand-slide algorithm shows that the results of the two approaches differ with regard to the areas affected. Although the finite element stability model is assumed to be more accurate regarding the determination of erosion zones, the fact that it is three-dimensional places a high burden on computation time. In addition, the need for more model parameters than just the friction angle cannot always be fulfilled. Consequently, the assumption of missing parameters has an artificial influence on the results.

The results of the presented numerical simulations of flow and wave-induced scour were found to be in good agreement with laboratory experiments. Further improvement of the results could be achieved by increasing number of couplings between flow simulations and sediment transport computations in order to take account of the changes in the bed geometry more frequently. The use of a finite element model of the soil as a criterion for erosion and sand-slides seems to be appropriate, especially if the influence of pressure is also taken into account.

A Wave theories

An oscillatory flow, such as the flow caused by a propagating wave, may be described by means of different complex mathematical theories. Although the linear or Airy wave theory is used very extensively, it does have limitations when it comes to shallow water or deep water, or waves with high steepness. Nevertheless, the simplicity and explicitness of the theory is an advantage over more complex theories such as the cnoidal wave theory of Korteweg and De Vries (1895) or stream function theory (Dean, 1965). Although the latter must be evaluated with the aid of a numerical scheme, which is a drawback in terms of simplicity, it is nevertheless very versatile, as will be shown in Chapter A.2.

A.1 Linear wave theory

Waves are described by several parameters. The main parameters are the length and height of the wave and the water depth in which the wave is propagating. Other parameters such as wave-induced velocities and dynamic pressure may be derived from the above-mentioned quantities. Figure A.1 shows the scheme of a propagating wave. The length of a wave is defined by the distance between two crests or troughs, respectively. The wave height is denoted by H and the water depth by h. $\eta(x,t)$ describes the position of the free surface in space and time. The shape of the illustrated wave is derived from linear wave theory and therefore takes the form of a sinusoidal oscillation (Eq. A.8). By placing the origin of the coordinate system at the still water level, the bottom is denoted by $z=-h$.

The basic assumptions in linear wave theory are that the flow is inviscid, the amplitude is small relative to the water depth, and the flow field is irrotational. No shear stress can be generated in the flow itself but only in the proximity of a

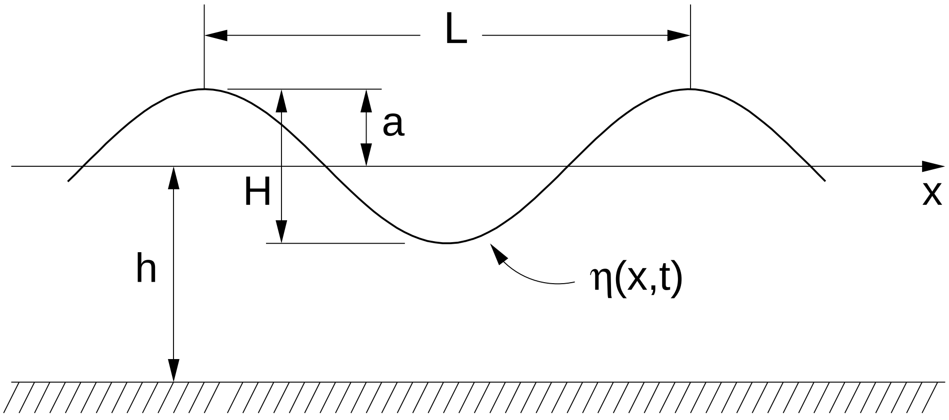

Figure A.1: Wave parameters

bottom boundary. In shallow water the wave motion may extend to the bottom, thereby generating a small boundary layer with rotational flow. Because this layer is very thin and its influence on wave motion is very slight, it is neglected in the equation of motion. The solution of the flow and pressure field is given by the potential function (Eq. A.1) where ϕ is the velocity potential.

$$\nabla^2\phi = \frac{\partial^2\phi}{\partial x^2} + \frac{\partial^2\phi}{\partial y^2} + \frac{\partial^2\phi}{\partial z^2} = 0 \tag{A.1}$$

A difficulty that arises in the application of linear wave theory concerns the imposition of boundary conditions. These may be expressed in the form of three equations. In accordance with Fig. A.1, η is the perturbation from the mean water level. The kinematic boundary condition states that a fluid particle at the free surface remainsat this location (Eq. A.2). Using the velocity potential instead of velocities leads to Eq. A.3.

$$-\frac{\partial\eta}{\partial t} - u\frac{\partial\eta}{\partial x} + w = 0 \tag{A.2}$$

$$\frac{\partial\eta}{\partial t} + \frac{\partial\phi}{\partial x}\frac{\partial\eta}{\partial x} = \frac{\partial\phi}{\partial z} \qquad at \;\; z = \eta \tag{A.3}$$

The second boundary condition states that the pressure at the free surface is constant. This is referred to as the dynamic boundary condition. Applying the

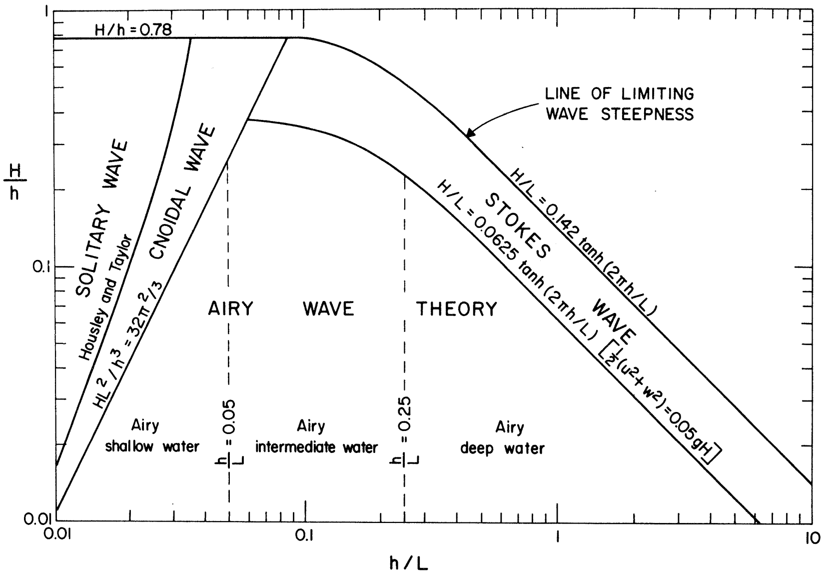

Figure A.2: Wave theories and their application range (Komar, 1998)

Bernoulli equation leads to

$$\frac{\partial \phi}{\partial t} + \frac{p}{\rho} + \frac{1}{2}\nabla\phi \cdot \nabla\phi + g\eta = F(t) \tag{A.4}$$

where p is the pressure at $z = \eta$ and ρ is the fluid density. Prescribing zero flux at the bottom boundary (Eq. A.5) then results in

$$\frac{\partial \phi}{\partial z} = 0 \quad at \;\; z = -h \tag{A.5}$$

By combining Eq. A.1 with the boundary conditions given by Eqs. A.2-A.5, Stokes assumed that the solution of the final equation could be expressed by a Fourier series. Linear (Airy) wave theory uses only the first term of this series, which leads to Eq. A.6.

$$\phi(x,z,t) = \frac{gH}{2\omega}\frac{cosh\, k(z+h)}{cosh\, kh} cos(kx - \omega t) \tag{A.6}$$

In the following equations $\theta = (kx - \omega t)$ describes the phase angle, i.e. the position in space and time where the equations are evaluated. Here, $k = 2\pi/L$ is the wave number. The angular frequency may be calculated from the dispersion relationship, which describes the relationship between the wave period T and the wave length L.

$$\omega^2 = gk \tanh(kh) \tag{A.7}$$

The free surface takes the form:

$$\eta = \frac{H}{2} cos\theta \tag{A.8}$$

The velocities and pressures in the vertical and horizontal direction (Eqs. A.9 and A.10) are derived from the flow potential function (Eq. A.6). The velocity perpendicular to the x-z plane ist constantly zero.

$$u = \frac{\pi H}{T} \frac{cosh(k(z+d))}{sinh(kd)} cos\theta \tag{A.9}$$

$$w = \frac{\pi H}{T} \frac{sinh(k(z+d))}{sinh(kd)} sin\theta \tag{A.10}$$

$$p = \rho g \left(\eta \frac{cosh(k(z+d))}{cosh(kd)} - z \right) \tag{A.11}$$

In linear wave theory it is assumed that the boundary conditions are fulfilled at the still water level. The equations resulting from this theory are not valid for positive values of z. Taking this into account, Chakrabarti (1971) developed an expression (Eq. A.12) for the pressure distribution which solves the problem and fulfills the dynamic boundary condition at the free surface. Unfortunately, the Laplace equation is no longer fulfilled at every wave position.

$$p_{mod} = \rho g \left(\eta \frac{cosh(k(z+d))}{cosh(k(d+\eta))} - z \right) \tag{A.12}$$

Modern measurement techniques provide a more precise knowledge of wave particle velocities. Wheeler (1970) found a similar expression (Eq. A.13) to adapt particle velocities to measured values. In the so-called “stretching method” an additional term is introduced for horizontal velocities. Although the boundary conditions at the free surface are no longer fulfilled, they are still valid at the bottom. Using this stretching method also for vertical velocities again leads to a situation where the Laplace equation is not fulfilled at every wave position.

$$u_{mod} = \frac{\pi H}{T} \frac{cosh\left(k(z+d)\frac{d}{d+\eta}\right)}{sinh(kd)} cos\theta \tag{A.13}$$

A.2 Stream function theory

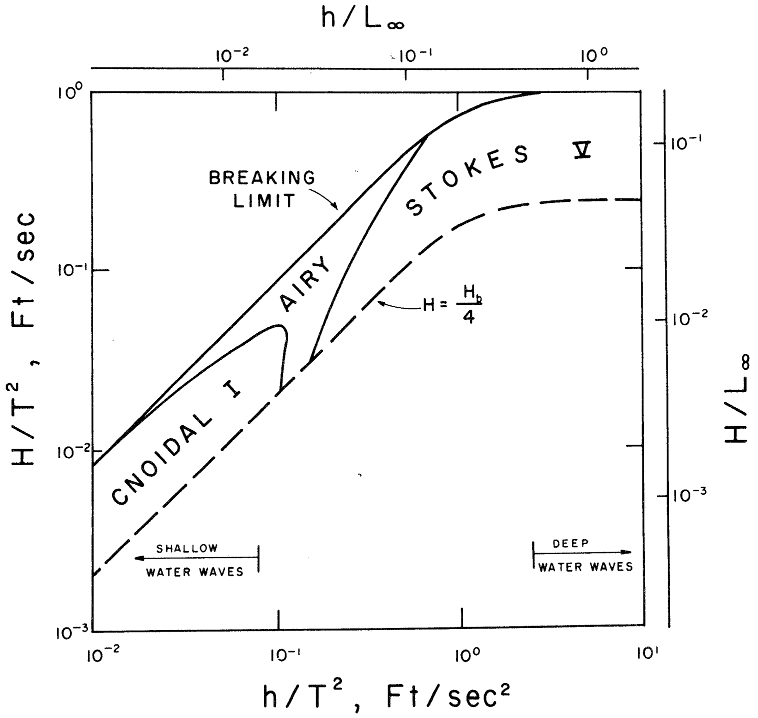

Figure A.3: Best fit for the free surface (Komar, 1998)

Using Airy wave theory to describe an initial wave in a channel is quite conve-

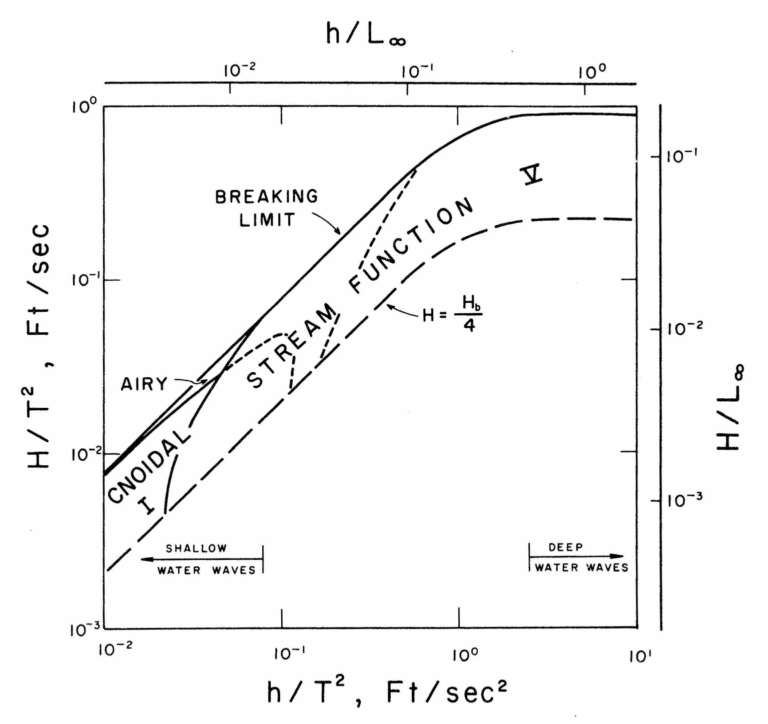

Figure A.4: Best fit for the free surface including stream function theory (Komar, 1998) nient owing to its explicit character and easily comprehensible formulation. Unfortunately, the theory is only valid when dealing with small amplitude waves such as those described in Chapters 3.2.1 and 3.2.2. For waves in very shallow or deep water or for waves with a high steepness, the application of other theories is more appropriate. The reason for this is the poor fit of the dynamic free surface boundary conditions of the Airy theory in such cases (Fig. A.3). As a consequence of the latter, the calculated waves are unstable. In the case of shallow water the cnoidal theory (Korteweg and De Vries, 1895) and the solitary wave theory (Boussinesq, 1872) yield good results for wave kinematics, whereas in deep water Stokes' theory of higher order proves to be more applicable (Figs. A.2 and A.3).

Extending the above-mentioned theories to a higher order becomes quite difficult and inconvenient. The stream function wave theory developed by Dean (1965) overcomes these problems. The underlying equations of this theory, which may be evaluated numerically to any required order, may be represented by a scalar function which is easy to handle and permits a calculation of the velocity vector field.

Eqs. A.14 and A.15 represent the linear form of the velocity potential and the stream function, respectively. The velocity field may be determined from the potential ψ of an irrotational and incompressible flow. A stream function exists for all two-dimensional flows (Dean and Dalrymple, 1984). These functions describe the flow rate in the longitudinal and transverse direction, respectively.

$$\phi(x,z,t) = -\frac{H}{2}\frac{g}{\omega}\frac{\cosh\,k(h+z)}{\cosh\,kh}\sin(kx-\omega t) \tag{A.14}$$

$$\psi(x,z,t) = -\frac{H}{2}\frac{g}{\omega}\frac{\sinh\,k(h+z)}{\cosh\,kh}\cos(kx-\omega t) \tag{A.15}$$

The fact that the isolines of constant velocity potential and constant stream function are orthogonal means that the product of the gradients of both functions is zero:

$$\nabla\psi\cdot\nabla\phi = 0 \tag{A.16}$$

This is also evident from Eqs. A.14 and A.15, which have a phase shift of $\pi/2$.

With regard to velocities, the stream function and the velocity potential are related by

$$\begin{aligned} u &= -\frac{\partial\phi}{\partial x} = -\frac{\partial\psi}{\partial z} \\ w &= -\frac{\partial\phi}{\partial z} = -\frac{\partial\psi}{\partial x} \end{aligned} \tag{A.17}$$

In order to obtain an expression for the stream function which is not time dependent, the coordinate system is moved with the wave celerity $C = L/T$. This implies that the wave form travels without a change of shape (Dean, 1965). The steady version of the stream function is therefore

$$\psi(x, z) = Cz - \frac{H}{2}\frac{g}{\omega}\frac{\sinh\, k(h+z)}{\cosh\, kh}\cos\, kx \tag{A.18}$$

The boundary conditions for the stream function are basically the same as those of the Airy wave theory. Firstly, the Laplace equation must be fulfilled throughout the fluid (Eq. A.19).

$$\nabla^2\psi = 0 \tag{A.19}$$

Neglecting the pressure at the free surface, and without time dependency, the dynamic free surface boundary condition is

$$\frac{1}{2}\left[\left(\frac{\partial\psi}{\partial z}\right)^2 + \left(\frac{\partial\psi}{\partial x}\right)^2\right] + g\eta = Q_B \tag{A.20}$$

where Q_B is the Bernoulli constant.

The kinematic free surface boundary condition states that the motion of the water surface must be consistent with the velocities of the water particles at the free surface (cf. Eq. A.3). Again without the time dependency the boundary condition may be written as

$$\frac{\partial\psi}{\partial x} = -\frac{\partial\psi}{\partial z}\frac{\partial\eta}{\partial x} \tag{A.21}$$

As no flux is permitted through the bottom boundary, the following holds:

$$\frac{\partial \psi}{\partial x} = 0 \quad \text{at} \quad z = -h \tag{A.22}$$

Besides the boundary conditions, a representation of the stream function which permits an evaluation of any order is required. The generalized form of the stream function of N^{th} order in a steady rendered coordinate system takes the form

$$\psi(x,z) = Cz - \sum_{n=1}^{N} X(n) \sinh \left\{nk(h+z)\right\} \cos nkx \tag{A.23}$$

In order to obtain the first order solution (cf. Eq. A.15) the coefficient $X(1)$ is

$$X(1) = -\frac{Hg}{2\omega}\frac{1}{\cosh kh} \tag{A.24}$$

The kinematic boundary condition is fulfilled by default when applying stream function theory, as it states that the free surface must be a streamline. In order to also fulfil the dynamic boundary condition, the X(n) coefficients must be chosen in such a way as to ensure that this condition is satisfied. This is achieved numerically by splitting the free surface of the wave into I discrete points. The dynamic boundary condition is then evaluated at each point I, thereby yielding a local value of the Bernoulli constant Q_{B_i} (Eq. A.25) which must be equal to the global constant Q_B.

In order to calculate the values of Q_{B_i}, the $X(n)$ coefficients must be known. Otherwise the velocities and the free surface in Eq. A.25 can not be determined. This results in an iterative procedure in which the $X(n)$ coefficients and the Q_{B_i} constants are calculated alternately until the boundary condition is satisfied.

$$Q_{B_i} = \frac{\left(\frac{\partial \psi}{\partial z}\right)_i^2 + \left(\frac{\partial \psi}{\partial x}\right)_i^2}{2} + g\eta_i = Q_B \tag{A.25}$$

With each iteration the boundary condition error decreases. For an exact solution this error would be zero. In the present solution scheme the iteration is repeated until the error is sufficiently small. A measure for the error is E_1 which is described by

$$E_1 = \frac{2}{L}\int_0^{L/2} \left(Q_{B_i} - Q_B\right)^2 \, dx \tag{A.26}$$

where

$$Q_B = \frac{2}{L}\int_0^{L/2} Q_{B_i} \, dx \tag{A.27}$$

The coefficients resulting from the iterative procedure must lead to a zero mean of the free surface $\eta(x)$:

$$(2/L)\int_0^{L/2} \eta(x) \, dx = 0 \tag{A.28}$$

In order to describe the boundary conditions in a numerical model using the results of stream function theory, the length of the wave L and the value of the stream function $\psi(x, \eta)$ must be determined. As described by Dean and Dalrymple (1984), this is achieved by applying the method of Lagrange multipliers (Hildebrand, 1965). The objective function

$$O_f = E_1 + \frac{2\lambda_1}{L}\int_0^{L/2} \eta(x) \, dx + \lambda_2 \left[\eta_0 - \eta\left(\frac{L}{2}\right) - H\right] \tag{A.29}$$

in which λ_1 and λ_2 are the Lagrange multipliers, must be minimized. This is a nonlinear equation which is solved by expanding the equation with a truncated Taylor series:

$$O_f^{j+1} = O_f^j \sum_{n=1}^{N+2} \frac{\partial O_f^j}{\partial X(n)} \Delta X^j(n) \tag{A.30}$$

The value of $\Delta X^j(n)$ represents a slight correction of $X^j(n)$ in the j^{th} iteration step. Minimizing the expanded objective function leads to a set of linear equations which may be solved using a suitable linear equation solver. Taking the correction of $\Delta X^j(n)$ into account in the next iterative step leads to

$$X^{j+1}(n) = X^j(n) + \Delta X^j(n) \tag{A.31}$$

This procedure is repeated until the result of the objective function O_f^{j+1} is sufficiently small.

Nomenclature

Greek

β	Actual bottom slope
η	Free surface position
γ	Unit weight
γ_{ij}	Shear strains
ν	Viscosity
ν_P	*Poisson's* ratio
ν_t	Turbulent viscosity
ω	Turbulent dissipation
ϕ	Critical slope angle
ρ	Density
σ	Normal stress
σ	Stress
τ_B	Bottom shear stress
$\tau_{b,cr}$	Critical bed shear stress
τ_{ij}	Shear stress
θ	Shields parameter

θ_{cr}	Critical Shields parameter
ε	Turbulent dissipation
ε_i	Extensional strains

Latin

c	Cohesion
D_*	Sediment grain parameter
d_m	Sediment mean diameter
d_{50}	Median grain diameter
E	Young's modulus
G	Shear modulus
g	Gravity
h	Water depth
H_s	Significant wave height
$H_{1/3}$	Average of 33% of the highest waves
H_{max}	Maximum wave height
k	Turbulent kinetic energy
k_s	Effective grain roughness
KC	Keulegan-Carpenter number
L	Wave length
N_i	Shape function
p	Pressure
q_s	Sediment flux

S	Free surface
s	Sediment grain size
T	Wave period
t	Time
T_p	Wave peak period
T_w	Wave period
T_z	Zero upcrossing wave period
u	Flow velocity
u_*	Shear velocity
u_b	Sediment particle velocity
u_i	Displacement vector
U_m	Near bed velocity
$v_{1/3}$	Average of 33% of the highest velocities
v_{max}	Maximum velocity
W_i	Weighting function

Bibliography

R. A. Bagnold. An approach to the sediment transport problem for general physics. Technical report, Geological Survey Prof. Paper 422-I, Washington, 1966.

R. A. Bagnold. The nature of saltation and bed load transport in water. *Proc. R. Soc. London*, Ser. A, 332, 1973.

F. Ballio, A. Radice, and S. Malavasi. Sediment motion in local bridge scour. DVD, Dipartimento di Ingegneria Idraulica, Politecnico di Milano, Italy, 2006.

K. J. Bathe. *Numerical methods in finite element analysis,* 3^{rd} *Ed.* Prentice-Hall, Englewood Cliffs, New Jersey, 1996.

J. C. W. Berkhoff. Computation of combined refraction-diffraction. In *Proceedings 13th Int. Conference on Coastal Engineering, Vancouver*, volume 1, 1972.

M. A. Biot. General theory of three-dimensional consolidation. *Journal of Applied Physics*, 12:155–164, 1941.

A. W. Bishop. The use of the slip circle in the stability analysis of slopes. *Géotechnique*, 5(1), 1955.

J. Boussinesq. Théorie des ondes et des remous qui se propagent le long d'un canal rectangulaire horizontal en communiquant au liquide continu dans ce canal des vitesses sensiblement pareilles de la surface au fond. *J. Math. Pures et Appliquées*, 17:55–108, 1872.

P. Bradshaw, D. H. Ferris, and N. P. Atwell. Calculation of boundary layer development using the turbulent energy equation. *Journal of Fluid Mechanics*, 28 (3):593–616, 1967.

M. Breuer. A challenging test case for large eddy simulations: high Reynolds number circular cylinder flow. *Int. J. of Heat and Fluid Flow*, 21, 2000.

H. N. C. Breusers, G. Nicollet, and H. W. Shen. Local scour around cylindrical piles. *J. Hydr. Res.*, 15(3):211–252, 1977.

J. Buffington. The legend of A.F. Shields. *J. Hydr. Eng.*, 125(4):376–387, 1999.

P. Catalano, M. Wang, G. Iaccarino, and P. Moin. Numerical simulation of the flow around a circular cylinder at high Reynolds numbers. *Int. J. of Heat and Fluid Flow*, 24, 2003.

S. K. Chakrabarti. Dynamics of single point mooring in deep water. *J. of Waterways, Harbors and Coastal Eng.*, 97, 1971.

N.-S. Cheng. Exponential formula for bedload transport. *J. Hydr. Eng.*, 128(10): 942–946, 2002.

Y. M. Chiew and B. M. Melville. Local scour around bridge piers. *J. Hydr. Res.*, 25(1):15–26, 1987.

Y.-M. Chiew and G. Parker. Incipient sediment motion on non-horizontal slopes. *Journal of Hydraulic Research*, 32(5), 1994.

I. C. Cormeau. Numerical stability in quasi-static elasto-vscoplasticity. *Int. J. Num. Meth. Eng.*, 9(1):109–127, 1975.

J. S. Damgaard, R. J. S. Whitehouse, and R. L. Soulsby. Bed-Load sediment transport on steep longitudinal slopes. *Journal of Hydraulic Engineering*, 123 (12), 1997.

J. S. Damgaard, B. M. Sumer, T. C. Teh, A. C. Palmer, P. Foray, and D. Osorio. Guidelines for Pipeline On-Bottom Stability on Liquefied Noncohesive Seabeds. *J. of Waterway, Port, Coastal and Ocean Engineering*, 132(4):300–309, 2006.

R. O. Davis and A. P. S. Selvadurai. *Plasticity and Geomechanics.* Cambridge Univ. Press, 2002.

R. O. Davis and A. P. S. Selvadurai. *Elasticity and Geomechanics.* Cambridge Univ. Press, 1996.

M. B. de Groot, M. D. Bolton, P. Foray, P. Meijers, A. C. Palmer, R. Sandven, A. Sawicki, and T. C. Teh. Physics of liquefaction phenomena around marine structures. *J. of Waterway, Port, Coastal and Ocean Engineering*, 132(4):227–243, 2006.

R. G. Dean. Stream function representation of nonlinear ocean waves. *J. Geophys. Res.*, 70(18):4561–4572, 1965.

R. G. Dean and R. A. Dalrymple. *Water Wave Mechanics for Engineers and Scientists.* Prentice-Hall International, Inc., London, 1984.

J. M. Duncan. State of the art: limit equilibrium and finite-element analysis of slopes. *J. Geotech. Eng., ASCE*, 122(7), 1996.

S. L. Dunn, P. L. Vun, A. H. C. Chan, and J. S. Damgaard. Numerical modeling of wave-induced liquefaction around pipelines. *J. of Waterway, Port, Coastal and Ocean Engineering*, 132(4):276–288, 2006.

R. W. Eadie and J. Herbich. Scour about a single, cylindrical pile due to combined random waves and current. In *Proceedings 20th Coastal Engineering Conference*, volume 3, 1986.

H. A. Einstein. Formulas for the transportation of bed-load. *Trans. Am. Soc. Civ. Eng.*, 107, 1942.

H. A. Einstein. The bed-load function for sediment transportation in open channel flow. Technical Bulletin 1026, U.S. Dep. of Agriculture, Washington, D.C., 1950.

F. Engelund. Flow and Bed Topography in Channel Bends. *J. Hydra. Div., ASCE*, 100(11), 1974.

F. Engelund and J. Fredsøe. A sediment transport model for straight alluvial channels. *Nordic Hydrology*, 7:293–306, 1976.

F. Engelund and E. Hansen. *A monograph on sediment transport in alluvial streams.* Teknisk Vorlag, Copenhagen, Denmark, 1967.

R. Ettema. Scour at bridge piers. Technical Report 216, School of Engineering, University of Auckland, Auckland, New Zealand, 1980.

W. Fellenius. Calculation of the stability of earth dams. In *Proc. 2nd congr. large dams, Washington DC*, 1936.

R. E. Findeiß. *Ein orts- und zeitadaptives Finite-Elemente-Verfahren zur Traglastanalyse wassergesättigter Böden.* Dissertation, Lehrstuhl für Statik der Technischen Universität München, 2001.

H. C. Frijlink. Discussion of bed load movement formulas. Report X2344/LV, Delft Hydraulics, Delft, The Netherlands, 1952.

J. Fröhlich and W. Rodi. LES of the flow around a circular cylinder of finite height. *Int. J. of Heat and Fluid Flow*, 25, 2004.

J. Fröhlich, W. Rodi, A. Dewan, and J. P. Fontes. Large-Eddy simulation of the flow around the free end of a circular cylinder. *Notes on Numerical Fluid Mechanics*, 82, 2003.

W. Graf. *Hydraulics of sediment transport.* McGraw-Hill, New York, 1971.

D. V. Griffiths and P. A. Lane. Slope stability analysis by finite elements. *Géotechnique*, 49(3), 1999.

D. V. Griffiths and R. M. Marquez. Three-dimensional slope stability analysis by elasto-plastic finite elements. *Géotechnique*, 57(6):537–546, 2007.

J. Grüne, U. Sparboom, R. Schmidt-Koppenhagen, H. Oumeraci, A. Mitzlaff, J. Uecker, and K. Peters. Innovative Scour Protection with Geotextile Sand Containers for Offshore Monopile Foundations of Wind Energy Turbines. In *3rd Int. Conf. on Scour and Erosion (ICSE), Amsterdam*, 2006.

J. Hardisty and R. J. S. Whitehouse. Evidence for a new sand transport process from experiments on saharan dunes. *Nature*, 332(6164):532–534, 1988.

P. B. Hasbo. *Flow and sediment transport over oblique bed forms.* PhD thesis, Dept. of Hydrodynamics and Water Resources, Technical University of Denmark, 1995.

J.-M. Hervouet. *Hydrodynamics of free surface flows - modelling with the finite element method.* John Wiley & Sons, Ltd, England, 2007.

J.-M. Hervouet and C.-T. Pham. Telemac version 5.7, release notes. Technical report, Laboratoire National d'Hydraulique et Environnement, EDF, Chatou, France, 2007.

F. B. Hildebrand. *Methods of applied mathematics,* 2^{nd} *Ed.* Prentice Hall, Englewood Cliffs, N.J., 1965.

P. Hjorth. *Studies on the nature of local scour.* Bull. Series A, No. 46, viii + 191p., Department of Water Resources Engineering, University of Lund, Sweden, 1975.

S. Ikeda. Incipient Motion of Sand Particles on Side Slopes. *J. Hydra. Div., ASCE*, 108(1), 1982.

S. Ikeda. Lateral Bed-Load Transport on Side Slopes. In *Civil Engineering Practice 2.* Technomic Publishing Company, USA, 1988.

J. A. Jankowski. A non-hydrostatic model for free surface flows. Institutsbericht 56, Institute of Fluid Mechanics, Universität Hannover, Germany, 1999.

A. Jennings and J. McKeown. *Matrix computation for engineers and scientists.* John Wiley, London, 1992.

B. Jeremic. Finite element methods for three-dimensional slope stability analysis. In D. V. Griffiths, G. A. Fenton, and T. R. Martin, editors, *Slope stability 2000.* ASCE, 2000.

A. A. Kalinske. Movement of sediment as bed load in rivers. *Transactions, American Geophysical Union*, 28(4), 1947.

H. Katsui and T. Toue. Methodology of estimation of scouring around large-scale offshore structures. In *Proceedings 3rd Int. Offshore and Polar Engineering Conference, Singapore*, volume 1, 1993.

T. Kobayashi and K. Oda. Experimental study on developing process of local scour around a vertical cylinder. In *Proceedings 24th Int. Conference on Coastal Engineering, Kobe, Japan*, volume 2, 1994.

F. G. Koch and C. Flokstra. Bed level computations for curved alluvial channels. Technical report, XIXth Congress of the International Association for Hydraulic Research, New Delhi India, 1981.

P. D. Komar. *Beach processes and sedimentation.* 2^{nd} *Edition.* Prentice-Hall, 1998.

D. J. Korteweg and G. De Vries. On the change of form of long waves advancing in a rectangular channel, and on a new type of long stationary waves. *Philos. Mag.*, 39, 1895.

A. Kovacs and G. Parker. A new vectorial bedload formulation and its application to the time evolution of straight river channels. *Journal of Fluid Mechanics*, 267, 1994.

R. Krantz. Measurement of friction ceofficients and cohesion for faulting and fault reactivation in laboratory models using sand and sand mixtures. *Tectonophysics, Elsevier Science B.V*, 188, 1991.

P. K. Kundu and I. M. Cohen. *Fluid Mechanics, 3. ed.* Elsevier Acad. Press, Amsterdam, 2004.

E. W. Lane. Design of Stable Channels. *Trans., ASCE*, 120, 1955.

L. Lau and P. Engel. Inception of sediment transport on steep slopes. *Journal of Hydraulic Engineering*, 125(5), 1999.

O. Leiner. Zur Erforschung der Geschiebe und Sinkstoffbewegung. *Zeitschrift für Bauwesen*, 62, 1912.

O. Link and U. Zanke. On the timedependent scour-hole volume evolution at a circular pier in uniform coarse sand. In *Proceedings of Second International Conference on Scour and Erosion*, 2004.

R. F. Luque and R. Beek. Erosion and transport of bedload sediment. *Journal of Hydraulic Research*, 14(2), 1976.

T. Matsui and K. C. San. Finite element slope stability analysis by shear strength reduction technique. *Soils Found.*, 32(1), 1992.

B. W. Melville. Scour at bridge sites. Technical Report 117, School of Engineering, Univ. of Auckland, Auckland, New Zealand, 1975.

B. W. Melville and Y. M. Chiew. Time scale for local scour at bridge piers. *J. Hydr. Eng.*, 125(1), 1999.

B. W. Melville and S. E. Coleman. *Bridge Scour.* Water Resources Publications, LLc, CO, USA, 2000.

B. W. Melville and A. J. Sutherland. Design method for local scour at bridge piers. *Journal of Hydraulic Engineering*, 114(10), 1988.

F. R. Menter. Improved two-equation k-ω turbulence models for aerodynamic flows. NASA technical memorandum 103975, NASA, Ames Research Center, California, 1992.

E. Meyer-Peter and R. Müller. Formulas for bed-load transport. In *Sec. Int. IAHR Congress, Stockholm, Sweden*, 1948.

E. Meyer-Peter and R. Müller. Eine Formel zur Berechnung des Geschiebetriebs. *Schweizerische Bauzeitung*, 67(3):29–32, 1949.

T. Nagata, T. Hosoda, T. Nakato, and Y. Muramoto. 3D numerical simulation of flow and local scour around a cylindrical pier. *Journal of Hydroscience and Hydraulic Engineering*, 20(1), 2002.

J. Nikuradse. Strömungsgesetze in rauhen Rohren. *Forschungsheft 361, VDI*, 1933.

G. Oliveto and W. H. Hager. Temporal Evolution of Clear-Water Pier and Abutment Scour. *Journal of Hydraulic Engineering*, 128(9), 2002.

N. R. B. Olsen and H. M. Kjellesvig. Three-dimensional flow modelling for estimation of maximum local scour depth. *J. Hydr. Res.*, 36(4), 1998.

N. R. B. Olsen and M. C. Melaaen. Three-dimensional calculation of scour around cylinders. *J. Hydr. Eng.*, 119(9):1048–1054, 1993.

H. Oumeraci, U. Prepernau, J. Grüne, U. Sparboom, R. Schmidt-Koppenhagen, and Z. Wang. Untersuchungen zur Kolkbildung und Kolkentwicklung an Monopile-Gründungsstrukturen von Offshore-Windenergieanlagen (OWEA) unter Seegangsbedingungen. Technical report, Coastal Research Center (FZK), Hannover, Germany, 2007.

A. S. Paintal. Concept of critical shear stress in loose boundary open channels. *J. Hydr. Res.*, 1, 1971.

P. Perzyna. Fundamental problems in viscoplasticity. In *Advances in Applied Mechanics*, volume 9. Academic Press, New York, 1966.

P. Perzyna. Thermodynamic theory of viscoplasticity. In *Advances in Applied Mechanics*, volume 11. Academic Press, New York, 1971.

A. Radice, F. Ballio, V. Armenio, and S. Franzetti. Scour development and sediment motion at rectangular and trapezoidal abutments. In *Proceedings Third International Conference on Scour and Erosion*, 2006.

R. Ratke, O. Kolditz, and W. Zielke. Rockflow: Dreidimensionales Dichtemodell DM2/3d. Technical report, Institut of Fluid Mechanics, Universität Hannover, 1996.

A. Raudkivi. *Loose boundary hydraulics.* 2nd Ed., Pergamon, Oxford, U.K., 1976.

A. J. Raudkivi and R. Ettema. Clear-water scour at cylindrical piers. *Journal of Hydraulic Engineering*, 109(3), 1983.

A. Roulund. *Three-dimensional modelling of flow around a bottom-mounted pile and it's application to scour.* PhD thesis, Dept. of Hydrodynamics and Water Resources, Technical University of Denmark, 2000.

A. Roulund, B. M. Sumer, J. Fredsøe, and J. Michelsen. Numerical end experimental investigation of flow and scour around a circular pile. *Journal of Fluid Mechanics*, 534:351–401, 2005.

D. Rudolph and K. J. Bos. Scour around a monopile under combined wave-current conditions and low KC-numbers. In *3rd Int. Conf. on Scour and Erosion (ICSE), Amsterdam*, 2006.

A. N. Sainak. Application of three-dimensional finite element method in parametric and geometric studies of slope stability. In *Advances in geotechnical engineering (Skempton Conference)*, volume 2. Tomas Telford, London, 2004.

T. M. Salaheldin, A. M. Imran, and M. H. Chaudhry. Numerical modeling of three-dimensional flow field around circular piers. *Journal of Hydraulic Engineering*, 130(2), 2004.

E. Salvatici and M. V. Salvetti. Large Eddy simulations of the flow around a circular cylinder: effects of grid resolution and subgrid scale modeling. *Wind and Structures*, 6(6), 2003.

W. P. Schellart. Shear test results for cohesion and friction coefficient for different granular materials: scaling implications for their usage in anlogue modelling. *Tectonophysics, Elsevier Science B.V.*, 324:1–16, 2000.

H. Schlichting. *Grenzschicht-Theorie.* Verlag G. Braun, Karlsruhe, Germany, 1982.

A. Schoklitsch. Über Schleppkraft und Geschiebebewegung. Technical report, W. Engelmann, Leipzig und Berlin, 1914.

M. Sekine and G. Parker. Bed-load transport on transverse slope. *J. Hydr. Eng.*, 118(4), 1992.

A. Shields. Anwendung der Ähnlichkeitsmechanik und der Turbulenzforschung auf die Geschiebebewegung. Technical Report 26, Mitt. der Preussischen Versuchsanstalt für Wasser, Erd- und Schiffbau, 1936.

A. Shvidchenko and G. Pender. Flume study of the effect of relative depth on the incipient motion of coarse uniform sediments. *Water Res. Research*, 36(2): 619–628, 2000.

G. M. Smart. Sediment transport formula for steep channels. *Journal of Hydraulic Engineering, ASCE*, 110(3), 1984.

I. M. Smith and D. V. Griffiths. *Programming the finite element method.* John Wiley & Sons Ltd., 2nd edition, 1988.

I. M. Smith and D. V. Griffiths. *Programming the finite element method.* John Wiley & Sons Ltd., 3rd edition, 1998.

I. M. Smith and R. Hobbs. Finite element analysis of centrifuged and built-up slopes. *Géotechnique*, 24(4), 1974.

E. Spencer. A method of analysis of the stability of embankments assuming parallel interslice forces. *Géotechnique*, 17(1), 1967.

B. M. Sumer and J. Fredsøe. Wave scour around a large vertical circular cylinder. *Journal of Waterway, Port, Coastal and Ocean Engineering*, 127(3), 2001a.

B. M. Sumer and J. Fredsøe. Scour around pile in combined wave and current. *Journal of Hydraulic Engineering*, 127(5), 2001b.

B. M. Sumer and J. Fredsøe. *The mechanics of scour in the marine environment.* World Scientific Publishing Co. Pte. Ltd., 2002.

B. M. Sumer and J. Fredsøe. *Hydrodynamics around cylindrical structures.* World Scientific Publishing Co. Pte. Ltd., 1997.

B. M. Sumer, J. Fredsøe, and N. Christiansen. Scour around vertical pile in waves. *J. Waterway, Port, Coastal and Ocean Eng.*, 118(1), 1992.

B. M. Sumer, N. Christiansen, and J. Fredsøe. Influence of cross section on wave scour around piles. *J. Waterway, Port, Coastal and Ocean Eng.*, 119(5):477–495, 1993.

B. M. Sumer, J. Fredsøe, S. Christensen, and M. T. Lind. Sinking/floatation of pipelines and other objects in liquefied soil under waves. *Coastal Engineering*, 38:53–90, 1999.

B. M. Sumer, F. Hatipoglu, J. Fredsøe, and N. O. Hansen. Critical flotation density of pipelines in soils liquefied by waves and density of liquefied soils. *J. of Waterway, Port, Coastal and Ocean Engineering*, 132(4):252–265, 2006a.

B. M. Sumer, F. Hatipoglu, J. Fredsøe, and S. K. Sumer. The sequence of sediment behaviour during wave-induced liquefaction. *Sedimentology*, 53:611–629, 2006b.

B. M. Sumer, F. Hatipoglu, and J. Fredsøe. Wave scour around a pile in sand, medium dense and dense silt. *J. Waterway, Port, Coastal and Ocean Eng.*, 133 (1):14–27, 2007.

A. M. Talmon and J.-U. Wiesemann. Influence of grain size on the direction on bed-load transport on transverse sloping beds. In *Proceedings Third International Conference on Scour and Erosion*. CURNET, Gouda, The Netherlands, 2006.

A. M. Talmon, M. C. L. M. van Mierlo, and N. Struiksma. Laboratory measurement of the direction of sediment transport on transverse alluvial-bed slopes. *J. Hydr. Research*, 33(4), 1995.

D. Taylor. Stability of earth slopes. *J. Boston Soc. Civ. Eng.*, 24, 1937.

T. C. Teh, A. C. Palmer, and J. S. Damgaard. Experimental study of marine pipelines on unstable and liquefied seabed. *Coastal Eng.*, 50(1-2):1–17, 2003.

S. P. Timoshenko and J. N. Goodier. *Theory of elasticity*. McGraw-Hill, New-York, 1951.

A. Tørum. Wave-induced Pore Pressures - Air/Gas Content. *J. of Waterway, Port, Coastal and Ocean Engineering*, 133(1):83–86, 2007.

T. Toue, H. Katsui, and K. Nadaoka. Mechanism of sediment transport around a large circular cylinder. In *Proceedings 23rd Int. Coastal Engineering Conference, Venice, Italy*, volume 3, 1992.

L. van Rijn. Sediment Transport, Part I: Bed Load Transport. *Journal of Hydraulic Engineering, ASCE*, 110(10), 1984.

L. van Rijn. *Principles of sediment transport in rivers, estuaries and coastal seas.* Aqua Publications, Amsterdam, 1993.

A. Verruijt. *Computational Geomechanics*. Kluwer Academic Publishers, Dordrecht, The Netherlands, 1995.

H. Weilbeer. Numerische Simulation von Strömung und Kolkung an Wasserbauwerken. Institutsbericht 66, Institute of Fluid Mechanics, Universität Hannover, Germany, 2001.

J. Wheeler. Method for calculating forces produced by irregular waves. *J. of Petroleum Technology*, pages 359–367, 1970.

F. M. White. *Fluid Mechanics*. McGraw-Hill, Boston, 5th edition, 2003.

R. Whitehouse and J. Hardisty. Experimental assessment of two theories for the effect of bedslope on the threshold of bedload transport. *Marine Geology*, 79, 1988.

D. Wilcox. *Turbulence modelling for CFD*. DCW Industries, Inc., La Cañada, California, 1993.

M. S. Yalin. *Mechanics of sediment transport*. Pergamon, Oxford, 1977.

M. S. Yalin and A. M. F. da Silva. *Fluvial processes*. IAHR Monograph, IAHR, Delft, The Netherlands, 2001.

C.-L. Yen, J.-S. Lai, and W.-Y. Chang. Modeling of 3D flow and scouring around circular piers. *Proceedings National Science Council, Republic of China*, 25(1): 17–26, 2001.

U. Zanke. *Grundlagen der Sedimentbewegung*. Springer-Verlag, 1982a.

U. Zanke. Kolke am Pfeiler in richtungskonstanter Strömung und unter Welleneinfluss. Technical Report 54, Franzius Institut, Universität Hannover, 1982b.

M. Zhao and B. Teng. Numerical simulation of wave-induced local scour around a large cylinder. *Coastal Engineering Journal*, 46(3), 2004.

M. Zhao, B. Teng, and S. Liu. Numerical simulation of wave scour around a large scale circular cylinder. *China Ocean Engineering*, 16(4), 2002.

M. Zhao, B. Teng, and L. Li. Local scour around a large-scale vertical circular cylinder due to combined wave-current action. *J. of Hydrodynamics, Ser. B*, 1: 7–16, 2004.

F. Ziegler. *Mechanics of solids and fluids,* 2^{nd} *Edition.* Springer-Verlag New York, Inc., 1995.

O. Zienkiewicz and I. Cormeau. Viscoplasticity, plasticity and creep in elastic solids. A unified numerical solution approach. *Int. J. Num. Meth. Eng.*, 8: 821–845, 1974.

O. Zienkiewicz and R. Taylor. *The Finite Element Method,* 5^{th} *Edition*, volume 1. Butterworth-Heinemann, 2000.

O. C. Zienkiewicz, C. Humpheson, and R. C. Lewis. Associated and non-associated viscoplasticity and plasticity in soil mechanics. *Géotechnique*, 25(4), 1975.

Liste der bereits erschienenen Institutsberichte

01/1970 **Holz, K.-P.** Ergänzung des Verfahrens finiter Elemente durch Ecksingularitäten zur verbesserten Berechnung schiefwinkliger Platten. Dissertation, Techn. Univ. Hannover, 1970

02/1971 **Ehlers, K.-D.** Berechnung instationärer Grund- und Sickerwasserströmungen mit freier Oberfläche nach der Methode finiter Elemente. Dissertation, Techn. Univ. Hannover, 1971

03/1971 **Meissner, U.** Berechnung von Schalen unter großen Verschiebungen und Verdrehungen bei kleinen Verzerrungen mit Hilfe finiter Dreieckselemente. Dissertation, Techn. Univ. Hannover, 1971

04/1972 **Grotkop, G.** Die Berechnung von Flachwasserwellen nach der Methode der finiten Elemente. Dissertation, Techn. Univ. Hannover, Sonderdruck aus dem Jahresbericht 1971 d. SFB 79, H. 2, 1972

05/1973 **Schulze, K.-W.** Eine problemorientierte Sprache für die Dynamik offener Gerinne. Dissertation, Techn. Univ. Hannover, Mitteil. d. SFB 79, Heft 1, 1973

06/1977 **Beyer, A.** Die Berechnung großräumiger Grundwasserströmungen mit Vertikalstruktur mit Hilfe der Finite-Element-Methode. Dissertation, Fortschrittberichte der VDI-Zeitschriften, Reihe 4, Nr. 34, 1977

07/1977 **Ebeling, H.** Berechnung der Vertikalstruktur wind- und gezeitenerzeugter Strömungen nach der Methode der finiten Elemente. Dissertation, Fortschrittberichte der VDI-Zeitschriften, Reihe 4, Nr. 32, 1977

08/1977 **Gärtner, S.** Zur Berechnung von Flachwasserwellen und instationären Transportprozessen mit der Methode der finiten Elemente. Dissertation, Fortschrittberichte der VDI-Zeitschriften, Reihe 4, Nr. 30, 1977

09/1977 **Herrling, B.** Eine hybride Formulierung in Wasserständen zur Berechnung von Flachwasserwellen mit der Methode finiter Elemente. Dissertation, Fortschrittberichte der VDI-Zeitschriften, Reihe 4, Nr. 37, 1977

10/1979 **Hennlich, H.-H.** Aeroelastische Stabilitätsuntersuchung von Linientragwerken. Dissertation, Fortschrittberichte der VDI-Zeitschriften, Reihe 4, Nr. 49, 1979

11/1979 **Kalocay, E.** Zur numerischen Behandlung der Konvektions-Diffusions-Gleichung im Hinblick auf das inverse Problem. Dissertation, Univ. Hannover, 1979

12/1980 **Januszewski, U**. Automatische Eichung für ein- und zweidimensionale, hydrodynamisch-numerische Flachwassermodelle. Dissertation, Univ. Hannover, Fortschrittberichte der VDI-Zeitschriften, Reihe 4, Nr. 58, 1980

13/1982 **Carbonel Huaman, C.A.A.** Numerisches Modell der Zirkulation in Auftriebsgebieten mit Anwendung auf die nordperuanische Küste. Dissertation, Univ. Hannover, 1982

14/1985 **Tuchs, M.** Messungen und Modellierung am Deep Shaft. Dissertation, Univ. Hannover, 1984

15/1985 Theu**nert, F.** Zum lokalen Windstau in ästuarien bei Sturmfluten - Numerische Untersuchungen am Beispiel der Unterelbe. Dissertation, Univ. Hannover, 1984

16/1985 **Perko, H.-D.** Gasausscheidung in instationärer Rohrströmung. Dissertation, Univ. Hannover, 1984

17/1985 **Crotogino, A.** Ein Beitrag zur numerischen Modellierung des Sedimenttransports in Verbindung mit vertikal integrierten Strömungsmodellen. Dissertation, Univ. Hannover, 1984

18/1985 **Rottmann-Söde, W.** Ein halbanalytisches FE-Modell für harmonische Wellen zur Berechnung von Wellenunruhen in Häfen und im Küstenvorfeld. Dissertation, Univ. Hannover, 1985

19/1985 **Nitsche, G.** Explizite Finite-Element-Modelle und ihre Naturanwendungen auf Strömungsprobleme in Tidegebieten. Dissertation, Univ. Hannover, 1985

20/1985 **Vera Muthre, C.** Untersuchungen zur Salzausbreitung in Ästuarien mit Taylor'schen Dispersionsmodellen. Dissertation, Univ. Hannover, 1985

21/1985 **Schaper, H.** Ein Beitrag zur numerischen Berechnung von nichtlinearen kurzen Flachwasserwellen mit verbesserten Differenzenverfahren. Dissertation, Univ. Hannover, 1985

22/1986 **Urban, C.** Ein Finite-Element-Verfahren mit linearen Ansätzen für stationäre zweidimensionale Strömungen. Dissertation, Univ. Hannover, 1986

23/1987 **Heyer, H.** Die Beeinflussung der Tidedynamik in ästuarien durch Steuerung - Ein Beitrag zur Anwendung von Optimierungsverfahren in der Wasserwirtschaft. Dissertation, Univ. Hannover, 1987

24/1987 **Gärtner, S.** Zur diskreten Approximation kontinuumsmechanischer Bilanzgleichungen. Institutsbericht, davon 4 Abschnitte als Habilitationsschrift angenommen, Univ. Hannover, 1987

25/1988 **Rogalla, B.U.** Zur statischen und dynamischen Berechnung geometrisch nichtlinearer Linientragwerke unter Strömungs- und Wellenlasten. Dissertation, Univ. Hannover, 1988

26/1990 **Lang, G.** Zur Schwebstoffdynamik von Trübungszonen in Ästuarien. Dissertation, Univ. Hannover, 1990

27/1990 **Stittgen, M.** Zur Fluid-Struktur-Wechselwirkung in flexiblen Offshore-Schlauchleitungen. Dissertation, Univ. Hannover, 1990

28/1990 **Wollrath, J.** Ein Strömungs- und Transportmodell für klüftiges Gestein und Untersuchungen zu homogenen Ersatzsystemen. Dissertation, Univ. Hannover, 1990

29/1991 **Kröhn, K.-P.** Simulation von Transportvorgängen im klüftigen Gestein mit der Methode der Finiten Elemente. Dissertation, Univ. Hannover, 1991

30/1991 **Lehfeldt, R.** Ein algebraisches Turbulenzmodell für Ästuare. Dissertation, Univ. Hannover, 1991

31/1991 **Prüser, H.-H.** Zur mathematischen Modellierung der Interaktion von Seegang und Strömung im flachen Wasser. Dissertation, Univ. Hannover, 1991

dito **Schröter, A.** Das numerische Seegangsmodell BOWAM2 1990 - Grundlagen und Verifikationen - . Univ. Hannover, 1991

32/1992 **Leister, K.** Anwendung numerischer Flachwassermodelle zur Bestimmung von Wasserlinien. Dissertation, Univ. Hannover, 1992

33/1993 **Ramthun, B.** Zur Druckstoßsicherung von Fernwärmenetzen und zur Dynamik von Abnehmeranlagen. Dissertation, Univ. Hannover, 1993

34/1993 **Helmig, R.** Theorie und Numerik der Mehrphasenströmungen in geklüftet-porösen Medien. Dissertation, Univ. Hannover, 1993

35/1994 **Plüß, A.** Netzbearbeitung und Verfahrensverbesserungen für Tidemodelle nach der Finiten Element Methode. Dissertation, Univ. Hannover, 1994

36/1994 **Nöthel, H.** Statistisch-numerische Beschreibung des Wellen- und Strömungsgeschehens in einem Buhnenfeld. Dissertation, Univ. Hannover, 1994

37/1994 **Shao, H.** Simulation von Strömungs- und Transportvorgängen in geklüfteten porösen Medien mit gekoppelten Finite-Element- und Rand-Element-Methoden. Dissertation, Univ. Hannover, 1994

38/1994 **Stengel, T.** Änderungen der Tidedynamik in der Deutschen Bucht und Auswirkungen eines Meeresspiegelanstiegs. Dissertation, Univ. Hannover, 1994

39/1994 **Schubert, R.** Ein Softwaresystem zur parallelen interaktiven Strömungssimulation und -visualisierung. Dissertation, Univ. Hannover, 1994

40/1994 **Alm, W.** Zur Gestaltung eines Informationssystems im Küsteningenieurwesen. Dissertation, Univ. Hannover, 1994

41/1994 **Benali, H.** Zur Kopplung von FEM- und CAD-Programmen im Bauwesen über neutrale Datenschnittstellen. Dissertation, Univ. Hannover, 1994

42/1995 **Schröter, A.** Nichtlineare zeitdiskrete Seegangssimulation im flachen und tieferen Wasser. Dissertation, Univ. Hannover, 1995

43/1995 **Blase, Th.** Ein systemtechnischer Ansatz zur Modellierung von Hydraulik, Stofftransport und reaktionskinetischen Prozessen in Kläranlagen. Dissertation, Univ. Hannover, 1995

44/1995 **Malcherek, A.** Mathematische Modellierung von Strömungen und Stofftransportprozessen in Ästuaren. Dissertation, Univ. Hannover, 1995

45/1995 **Lege, T.** Modellierung des Kluftgesteins als geologische Barriere für Deponien. Dissertation, Univ. Hannover, 1995

46/1996 **Arnold, H.** Simulation dammbruchinduzierter Flutwellen. Dissertation, Univ. Hannover, 1996

47/1996 **Kolditz, O.** Stoff- und Wärmetransport im Kluftgestein. Habilitation, Univ. Hannover, 1996

48/1996 **Hunze, M.** Numerische Modellierung reaktiver Strömungen in oberflächenbelüfteten Belebungsbecken. Dissertation, Univ. Hannover, 1996

49/1996 **Wollschläger, A.** Ein Random-Walk-Modell für Schwermetallpartikel in natürlichen Gewässern. Dissertation, Univ. Hannover, 1996

50/1997 **Feist, M.** Entwurf eines Modellierungssystems zur Simulation von Oberflächengewässern. Dissertation, Univ. Hannover, 1997

51/1997 **Hinkelmann, R.** Parallelisierung eines Lagrange-Euler-Verfahrens für Strömungs- und Stofftransportprozesse in Oberflächengewässern. Dissertation, Univ. Hannover, 1997

52/1997 **Barlag, C.** Adaptive Methoden zur Modellierung von Strofftransport im Kluftgestein. Dissertation, Univ. Hannover, 1997

53/1997 **Saberi-Haghighi, K.** Zur Ermittlung der verformungsabhängigen Windbelastung bei Hängedächern. Dissertation, Univ. Hannover, 1997

54/1998 **Krüger, A.** Physikalische Prozesse im Nachklärbecken - Modellbildung und Simulation. Dissertation, Univ. Hannover, 1998

55/1998 **Wolters, A. H.** Zur Modellierung des instationären thermohydraulischen Betriebsverhaltens von Fernwärmeanlagen. Dissertation, Univ. Hannover, 1998

56/1999 **Jankowski, J. A.** A non-hydrostatic model for free surface flows. Dissertation, Univ. Hannover, 1999

57/1999 **Kopmann, R.** Mehrdimensionale Effekte in dimensionsreduzierten Gewässergütemodellen. Dissertation, Univ. Hannover, 1999

58/1999 **Kahlfeld, A.** Numerische Seegangsmodellierung als Bestandteil einer funktionellen Hafenplanung. Dissertation, Univ. Hannover, 1999

59/1999 Festschrift zum 60. Geburtstag von Prof. Dr.-Ing. Werner Zielke. Univ. Hannover, 1999

60/2000 **Kolditz, O., Zielke, W., Wriggers, P., Dürbaum, H.-J., Wallner, M.** 3. Workshop Kluft-Aquifere - Gekoppelte Prozesse in Geosystemen. Univ. Hannover, 2000

61/2001 **Malcherek, A.** Hydromechanik der Fließgewässer. Habilitation, Univ. Hannover, 2001

62/2001 **Thorenz, C.** Model Adaptive Simulation of Multiphase and Density Driven Flow in Fractured and Porous Media. Dissertation, Univ. Hannover, 2001

63/2001 **Kaiser, R.** Gitteradaption für die Finite-Elemente-Modellierung gekoppelter Prozesse in geklüftet-porösen Medien. Dissertation, Univ. Hannover, 2001

64/2001 **Rother, T.** Geometric Modelling of Geo-Systems. Dissertation, Univ. Hannover, 2001

65/2001 **Habbar, A.** Direkte und inverse Modellierung reaktiver Transportprozesse in klüftig-porösen Medien. Dissertation, Univ. Hannover, 2001

66/2001 **Weilbeer, H**.: Strömung und Kolkung an Wasserbauwerken. Dissertation, Univ. Hannover, 2001.

67/2002 **Hoyme**, H.: Mesoskalige morphodynamische Modellierungen am Beispiel der Meldorfer Bucht. Dissertation, Univ. Hannover, 2002.

68/2004 **Moenickes, S**.: Grid Generation for Simulation of Flow and Transport Processes in Fractures-Porous Media. Dissertation, Univ. Hannover, 2004

69/2004 **Strybny, J.:** Ein phasenauflösendes Seegangsmodell zur Ermittlung von Bemessungsparametern für Küstenstrukturen. Dissertation, Univ. Hannover 2004

70/2004 **Weilbeer, J.:** Modellierung des Partikeltransports in Nachklärbecken als Mehrphasenströmung. Dissertation, Univ. Hannover 2004

71/2006 **Mittendorf, K.:** Hydromechanical Design Paramters and Design Loads for Offshore Wind Energy Converters, Dissertation, Leibniz Univ. Hannover 2006

72/2006 **Kohlmeier, M.:**, Coupling of thermal, hydraulic and mechanical processes for geotechnical simulations of partially saturated porous media, Dissertation, Leibniz Univ. Hannover 2006

73/2006 **Schumacher, S.:**, Leistungsbestimmende Prozesse in Nachklärbecken – Einflussgrößen, Modellbildung und Optimierung , Dissertation, Leibniz Univ. Hannover 2006

74/2008 **Ziefle, G.:** Modeling Aspects of Coupled Hydraulic-Mechanical Processes in Clay Material, Dissertation, Leibniz Univ. Hannover 2008

75/2008 **Schimmels, S.:** Numerical Simulation of the Influence of Circular Cylinders on Mixing and Entrainment in Natural Density Currents, Dissertation, Leibniz Univ. Hannover 2007